

INTERIM SUMMARY REPORT

For The Period

1 JULY 1965 - 30 SEPTEMBER 1966

**INVESTIGATION OF THE COMBINED EFFECTS OF
SPACE ENVIRONMENTAL PARAMETERS ON
SPACE VEHICLE MATERIALS**

by

C. A. ESCOFFERY

October 1966

for

NASA

George C. Marshall Space Flight Center

Huntsville, Alabama

Contract No. NAS 8-20210

Control No. DCN 1-5-54-01211-01 (IF)

Approved by:



E. F. Smith, Manager
Materials Technology Department

HUGHES AIRCRAFT COMPANY
AEROSPACE GROUP
RESEARCH AND DEVELOPMENT DIVISION
CULVER CITY, CALIFORNIA

FOREWORD

This report summarizes the first year's effort by The Materials Technology Department of Hughes Aircraft Company, Culver City, California under Contract Number NAS 8-20210 with the National Aeronautics and Space Administration. The Contracting Officer's Technical Representative was Mr. E. C. McKannan, Chief of the Engineering Physics Branch, Materials Division, Propulsion and Vehicle Engineering Laboratory, George C. Marshall Space Flight Center, Huntsville, Alabama.

Grateful acknowledgement is made to the numerous members of the technical staff who contributed to the program; in particular to F. G. Albright for research assistance and for a large share in the project; to G. R. Blair for studies on the measurement of thermal properties, and for suggesting the use of an integrating sphere to make the in situ solar absorptance measurements; to P. M. Blair, Jr. for assistance on vacuum techniques; to T. Handy, J. Rogers, and P. M. Blair, Jr. for assistance with the design and checkout of the optical integrating sphere; to R. Turk and R. Culpepper for their help in making the titanium foil window; to Dr. E. C. Smith and R. L. Birdsall for carrying out the radiation characterization and dosimetry; to L. Victor and G. Hecker for operating the electron beam generator; to B. Kimmel and P. C. Crepeau for assistance in securing many of the material specimens; to D. Wile, T. Hershberger, and T. Ono for design of major parts of the experimental chamber; to R. Gourlay and E. R. Haberland for assistance in circuit design; and to R. Y. Scapple for supervision and consultation.

SUMMARY

Details are presented of an environmental chamber designed and built to perform selected in-situ property measurements on materials exposed to a simulated space environment. The environment stresses include vacuum (10^{-9} torr), electrons, protons, and ultraviolet radiation. The test samples are disc-shaped specimens (up to twenty-five) mounted in suitable holders hinged along the rim of a turntable. The property measurements include solar absorptance, dc resistivity, microwave permittivity (dielectric constant and loss tangent), and thermal diffusivity and conductivity.

A special integrating sphere that utilizes 99 percent of the internal reflecting surface was designed and fabricated to measure solar absorptance (by integration of spectral reflectance). The sphere was smoked with magnesium oxide and checked out in air. Two thermal control coatings (black and white, respectively) that had been calibrated in a standard Gier-Dunkle integrating sphere were used to evaluate the sphere. Agreement between the two instruments was good and within the experimental error.

Studies made on dc resistivity of various materials indicated that non-electroded specimens could be used. Microwave permittivity at 9.28 GHz on these specimens were carried out in a special resonant-cavity vacuum-dielectrometer. The effect of specimen diameter and of specimen thickness on the permittivity values of a number of materials was investigated. The magnitude of the systematic error in measured values of dielectric constant as a function of specimen diameter was found to correspond to calculated values. A review of the theory of the TE_{01n} resonant-cavity dielectrometer is presented.

Studies were conducted on thermal diffusivity measurements by the flash technique. Improved results were obtained using photoflash bulbs in place of a xenon flash lamp as the thermal pulse source. Good agreement with known values was obtained on stainless steel and on alumina specimens with soot-blackened front surfaces.

An irradiation run was conducted on 0.3-inch thick non-electroded specimens selected from eight material classes which include epoxy-fiberglass laminate, silicone-fiberglass laminate, polyurethane resin, epoxy-polyamide resin, SP-1 polyimide resin, FEP Teflon, TFE Teflon, and polyethylene.

The specimens were irradiated with 1 Mev electrons to a total dose of 10^8 rads. DC resistivity measurements were made in vacuo during the course of irradiation. In addition, measurements were made in air of pre- and post-irradiation microwave permittivity and post-irradiation permittivity at 1 kHz.

Excluding the laminates, the specimens developed typical Lichtenberg figures ("trees"). Most of the specimens also displayed some darkening in color. The dielectric properties were not significantly affected except for the polyurethane which showed a permanent decrease in resistivity after 10^5 rads of dose, and the polyimide which showed a permanent decrease in resistivity after 10^7 rads. The epoxy laminate and the epoxy-polyamide resin displayed a resistivity decrease after 10^6 rads but appeared to recover on further irradiation. The resistivity of the polyethylene dropped after 10^8 rads but appeared to recover after four weeks storage (in air). The resistivity of the FEP Teflon and of the silicone laminate remained unchanged.

The permittivity values of the specimens were not significantly affected except for the polyurethane which showed a slight increase in dielectric constant.

Pressures in the environmental chamber during the irradiation were generally kept in the 10^{-9} to 10^{-8} range, except for the final stages of the run when higher dose rates had to be employed and a few specimens showed outgassing. The polyurethane and the polyethylene displayed outgassing at dose rates above 1.8×10^4 rads/sec causing the chamber pressure to rise into the 10^{-7} to 10^{-6} torr range. At 3.6×10^4 rads/sec the FEP Teflon gradually began to show marked outgassing and raised the chamber pressure into the low 10^{-5} torr range.

CONTENTS

1.0	INTRODUCTION	1
2.0	EQUIPMENT DESIGN AND FABRICATION	3
2.1	Environmental Chamber	3
2.2	Irradiation Station	15
2.3	Optical Properties Station	22
2.4	Thermal Properties Station	22
2.5	DC Resistivity Station	22
2.6	Dielectrometer Station	31
3.0	DOSIMETRY AND RADIATION CHARACTERIZATION FOR THE ELECTRON BEAM GENERATOR	49
3.1	Introduction	49
3.2	Dosimetry Techniques	49
3.3	Measurements	51
4.0	EXPERIMENTAL RESULTS	55
4.1	Studies on the Measurement of Optical Properties	55
4.2	Studies on the Measurement of Thermal Properties	63
4.3	Studies on the Measurement of DC Resistivity	68
4.4	Studies on the Measurement of Microwave Permittivity	71
	A. Effect of Specimen Diameter	71
	B. Effect of Specimen Thickness	76
4.5	Electron Irradiation Run No. 1	81
	A. Specimen Preparation	81
	B. Electron Irradiation	84
	C. Results, Observations, and Discussion	88
	APPENDIX A. REVIEW OF THE THEORY OF THE TE _{01n} RESONANT CAVITY DIELECTROMETER	101
	APPENDIX B. AN INTEGRATING SPHERE FOR MEASURING THE REFLECTANCE OF IRRADIATED MATERIALS	127
	REFERENCES	135

ILLUSTRATIONS

Figure 1.	Schematic representation of environmental chamber and associated property measurements	4
Figure 2.	Schematic cross section of environmental chamber	4
Figure 3.	Details of environmental chamber	5
Figure 4.	Photograph of environmental chamber	7
Figure 5.	Schematic representation of the dc resistivity and thermal stations	8
Figure 6.	Schematic representation of proposed specimen transfer mechanism to vacuum dielectrometer	8
Figure 7.	Turntable, irradiation station, and dc resistivity station	9
Figure 8.	Details of turntable	11
Figure 9.	Details of turntable support stand	13
Figure 10.	Details of irradiation station	17
Figure 11.	Titanium window	21
Figure 12.	Details of optical station	23
Figure 13.	Interior view of integrating sphere	24
Figure 14.	View of assembled integrating sphere (without detector)	24
Figure 15.	Details of integrating sphere (upper half)	25
Figure 16.	Details of integrating sphere (lower half)	27
Figure 17.	Details of integrating sphere support	29
Figure 18.	Details of dc resistivity station	33
Figure 19.	DC resistivity station, open	37
Figure 20.	DC resistivity station, closed	37
Figure 21.	Circuit diagram for measuring dc resistivity	38
Figure 22.	Vacuum microwave dielectrometer design	40
Figure 23.	Details of proposed specimen transfer tunnel	41
Figure 24.	Block diagram for measuring permittivity in microwave dielectrometer	44
Figure 25.	Vacuum microwave dielectrometer assembly	45
Figure 26.	Resonance curve for TE ₀₁₅ mode in air-filled cavity	48

Figure 27.	Low Z AgPO_3 fluorod calibration	50
Figure 28.	Thermoluminescent dosimeter calibration	50
Figure 29.	Dose rate versus beam current (Al plate monitor)	52
Figure 30.	Comparison of the UV output of three sources.	56
Figure 31.	Signal flow-chart, optical measurements	58
Figure 32.	Detectivity of typical detectors	59
Figure 33.	Monochromator calibration curve (0.3 - 3.5 μ)	61
Figure 34.	Monochromator calibration curve (0.3 - 0.8 μ)	61
Figure 35.	Comparison (in air) of small vacuum integrating sphere with Gier-Dunkle integrating sphere	62
Figure 36.	Rear face temperature rise of 0.062 inch aluminum	66
Figure 37.	Time trace of Sylvania Blue Dot photoflash bulb	66
Figure 38.	Breadboard set-up for preliminary dc resistivity measurements	69
Figure 39.	Electrode configuration for preliminary dc resistivity measurements	70
Figure 40.	Placement modes in specimen-diameter studies in a TE_{015} cavity resonator.	72
Figure 41.	Effect of specimen diameter on dielectric properties measured in a TE_{015} cavity resonator	74
Figure 42.	Microwave (9.28 GHz) dielectric constant of various materials as a function of specimen thickness	77
Figure 43.	Microwave (9.28 GHz) loss tangent of various materials as a function of specimen thickness	77
Figure 44.	Resonance half-power bandwidth of TFE Teflon as a function of specimen thickness	82
Figure 45.	Resonance half-power bandwidth of polyethylene as a function of specimen thickness	82
Figure 46.	Electron beam generator	85
Figure 47.	Specimen layout positions on turntable (top view)	87
Figure 48.	View of non-irradiated (top row) and irradiated (bottom row) specimens. Specimens are in alpha- betical sequence beginning with A on the left	89
Figure 49.	Non-irradiated and irradiated polyurethane	89
Figure 50.	Non-irradiated and irradiated epoxy-polyamide	89
Figure 51.	Non-irradiated and irradiated TFE Teflon	90

Figure 52. Non-irradiated and irradiated polyethylene . . .	90
Figure 53. DC resistivity of specimens as a function of 1 Mev electron dose	92

TABLES

Table 1.	Calculations of electron energy spectrum . . .	53
Table 2.	Chamber background dose measurements . . .	53
Table 3.	Effect of specimen diameter on measured dielectric properties in a cavity dielectrometer .	75
Table 4.	Dielectric-constant relative-error values calculated by Equation (23), as a function of specimen diameter. (Cavity diameter $a = 2.160$ inches.)	75
Table 5.	Pre-irradiation permittivity of specimens, 0.310 inch thick, at 9.28 GHz	75
Table 6.	Pre-irradiation permittivity of Teflon specimens, 0.280 inch thick, at 9.28 GHz	80
Table 7.	Parameters for irradiation Run No. 1	84
Table 8.	DC volume resistivity of 0.3-inch thick specimens irradiated in vacuum with 1 Mev electrons as a function of dose (in rads)	93
Table 9.	Microwave (9.28 GHz) permittivity in air of Run No. 1 specimens.	95
Table 10.	Rounded average values of microwave (9.28 GHz) permittivity of Run No. 1 specimens	98
Table 11.	Final values of permittivity at a frequency of 1 kHz and 9.28 GHz, respectively	99

1.0 INTRODUCTION

This summary report covers effort on the subject research program during the period 1 July 1965 to 30 September 1966. The general objective of the research program is to obtain pertinent, valid, experimental data of the effects produced on space vehicle materials by ultra-low pressures, temperature extremes, and space radiation. Specific objectives are outlined in the Contractual Statement of Work.

The underlying philosophy of the program is to perform in situ property measurements on selected materials exposed to a simulated space environment. The property measurements and corresponding material classes are:

1. Solar absorptance on thermal control coatings and optical films;
2. DC conductivity, dielectric constant, and dissipation factor on dielectrics;
3. Thermal diffusivity and conductivity on thermal insulators.

The data generated will be for application to the engineering design of space vehicles. To ensure a high level of statistical confidence, twenty-five specimens may be mounted at one time on a "Lazy Susan" within a specially designed vacuum chamber. Property measurements are made during the course of irradiation without removal of the specimens from the chamber.

The space radiation to be simulated during the projected research program will consist of ultraviolet light, electrons, and protons. Specimen temperature will range from -195°C to $+180^{\circ}\text{C}$, and pressures will be in the 10^{-7} to 10^{-9} torr range. In the irradiation studies reported herein, the specimens were subjected at near room temperatures to 1 Mev electrons in a vacuum of 10^{-7} to 10^{-9} torr.

2.0 EQUIPMENT DESIGN AND FABRICATION

2.1 ENVIRONMENTAL CHAMBER

To fulfill the objectives outlined in the previous section, a special vacuum chamber had to be designed and fabricated. Figure 1 is a schematic representation of the chamber and associated property measurements and Figure 2 is a schematic cross section. Details of the exterior envelope and vacuum equipment* are shown in Figure 3. Figure 4 is a photograph of the chamber taken when it was first received.

The material test specimens are mounted on a "Lazy Susan" turntable which can be turned to bring the specimens sequentially into a temperature-controlled irradiation station. From the irradiation station the specimens can be transferred to any of four property measurement stations. Although the chamber and turntable were designed around the property measurements described in the Introduction and illustrated in Figure 1, the basic concept will permit other types of measurements to be made in the future. Figure 5 is a schematic representation of the dc resistivity and thermal stations, and Figure 6 of the dielectrometer station. The optical station is indicated in Figure 2. These stations are described more fully in following sections.

The test specimens are disc-shaped ranging in thickness from thin foil up to about 3/8-inch. Two diameters are employed, 2.135 and 7/8-inch, respectively. The larger value is dictated by the microwave resonant-cavity dielectrometer used for measurement of permittivity. (The same diameter is also used on the dc resistivity measurements.) The smaller value, used on the optical and thermal specimens, is determined by the Gier-Dunkle integrating sphere and hohlraum employed as standard instruments for spectral reflectance measurements.

The test specimens are mounted in 25 holders hinged along the rim of the turntable, as shown in Figure 7. The turntable is supported

* Built by the Vacuum Tube Products Division of Hughes Aircraft Company, Oceanside, California.

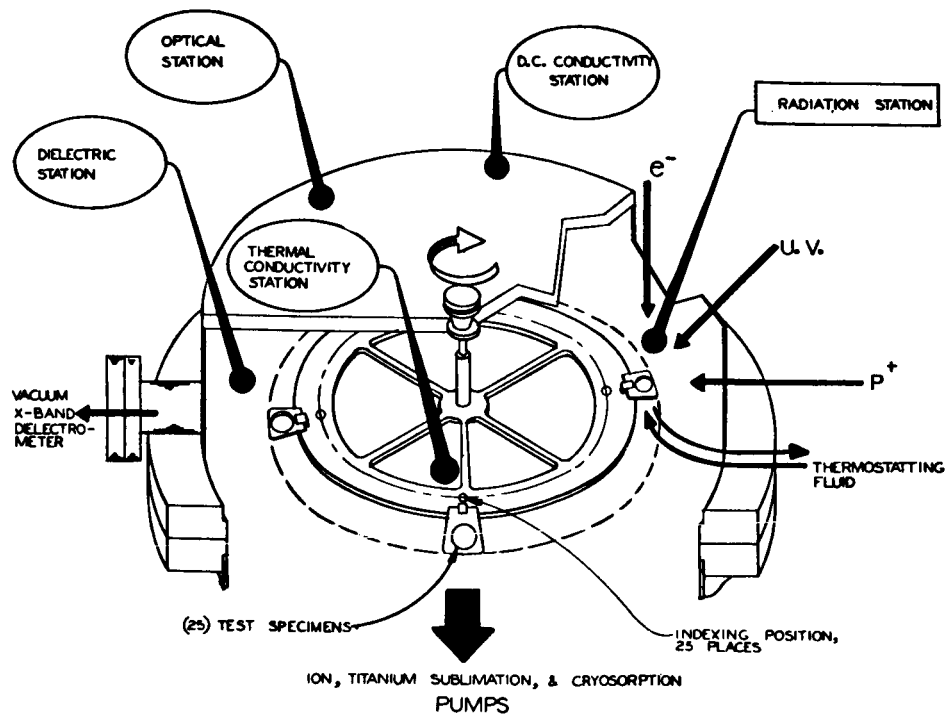


Figure 1. Schematic representation of environmental chamber and associated property measurements.

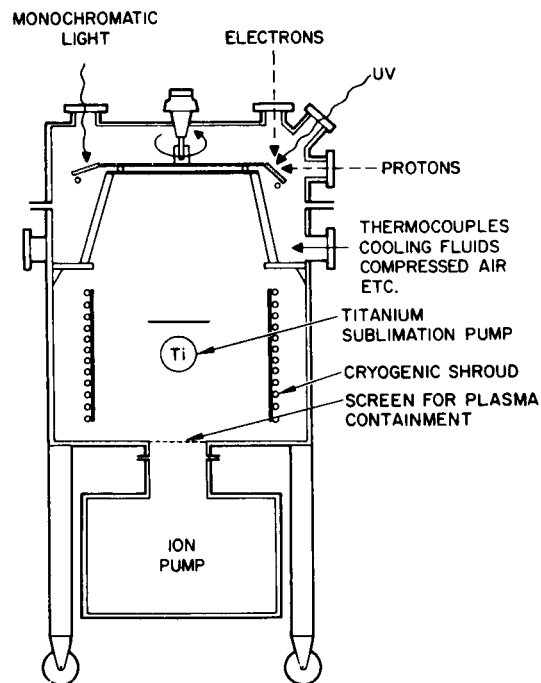


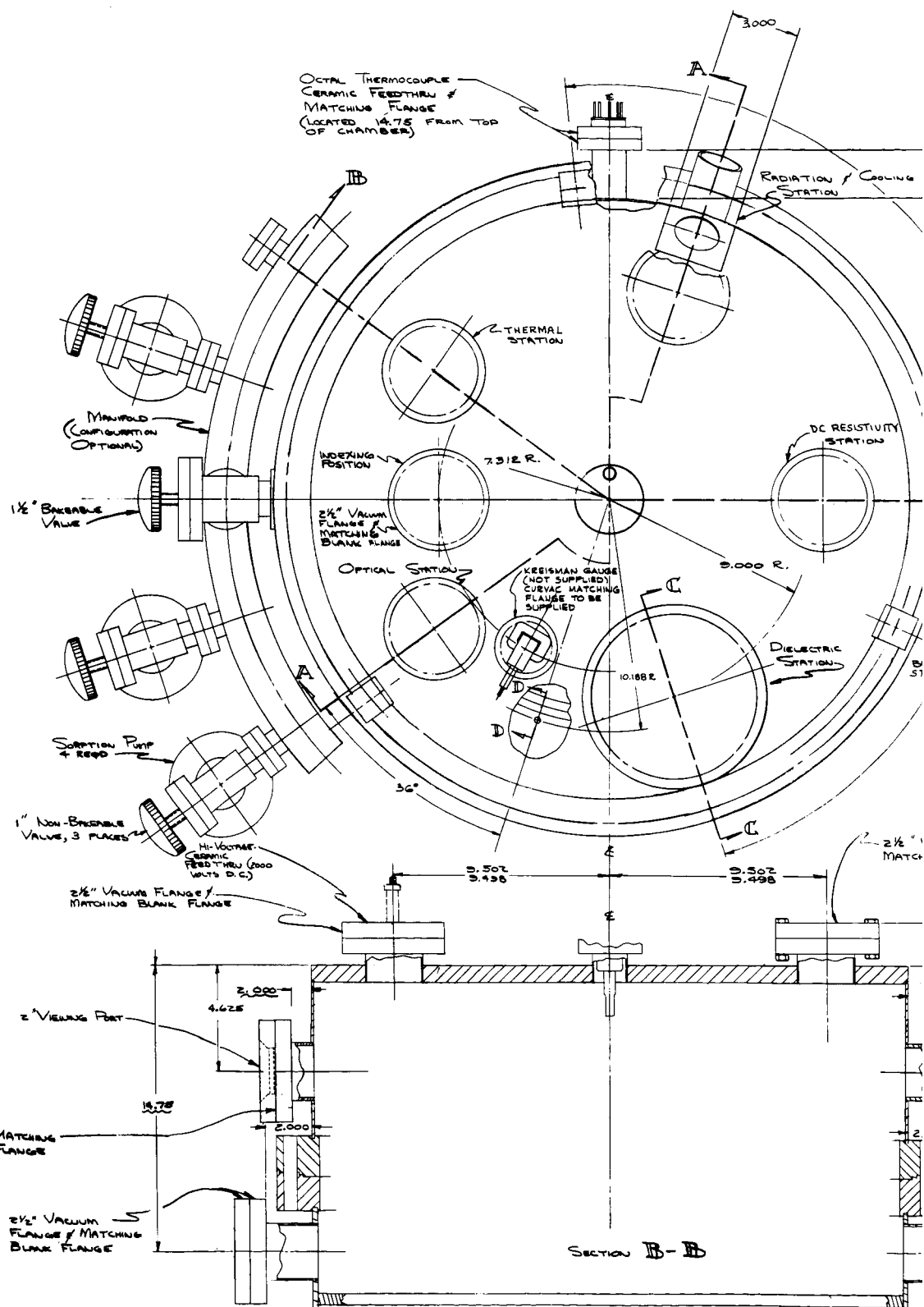
Figure 2. Schematic cross section of environmental chamber.

D

C

B

A



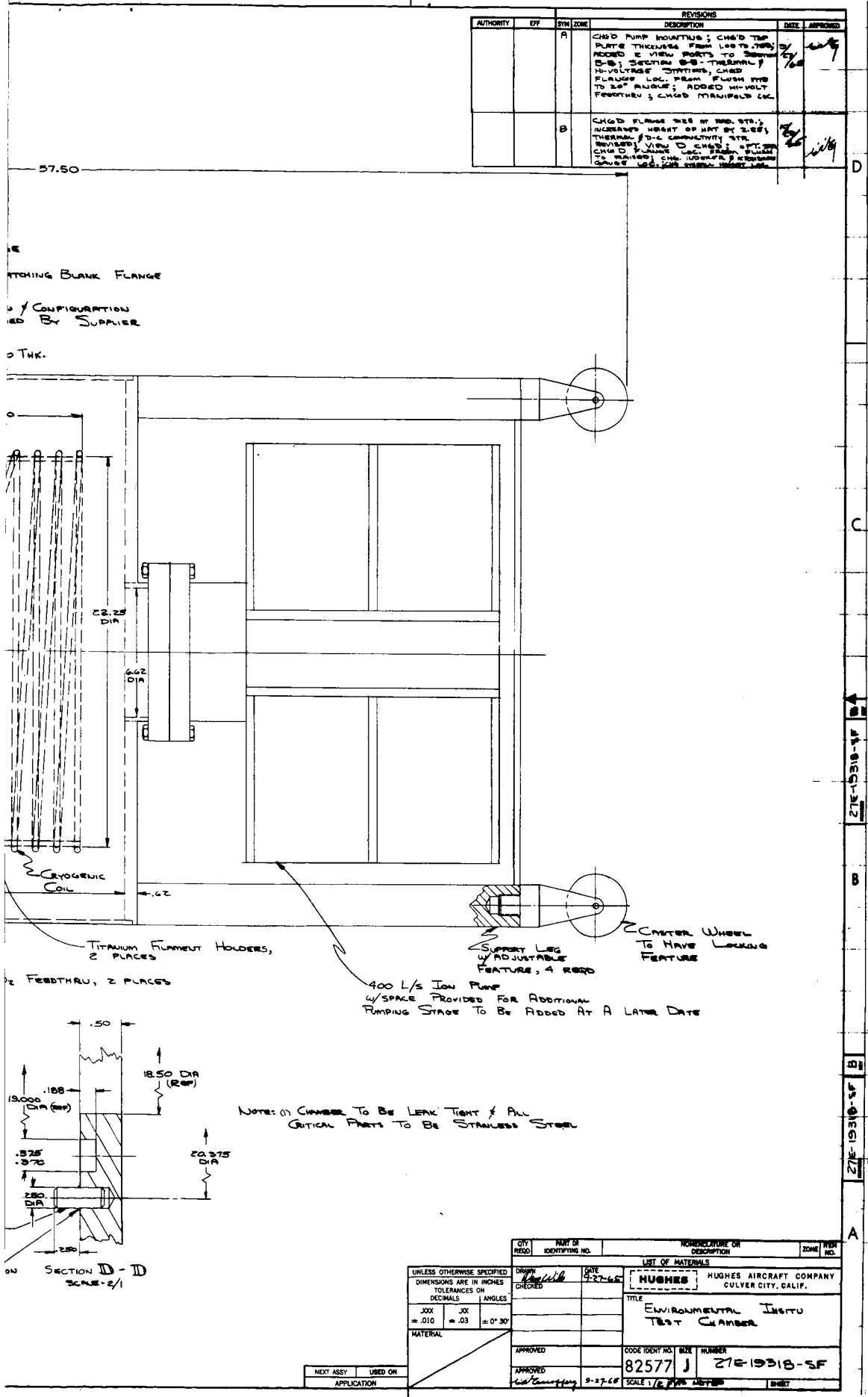


Figure 3. Details of environmental chamber.

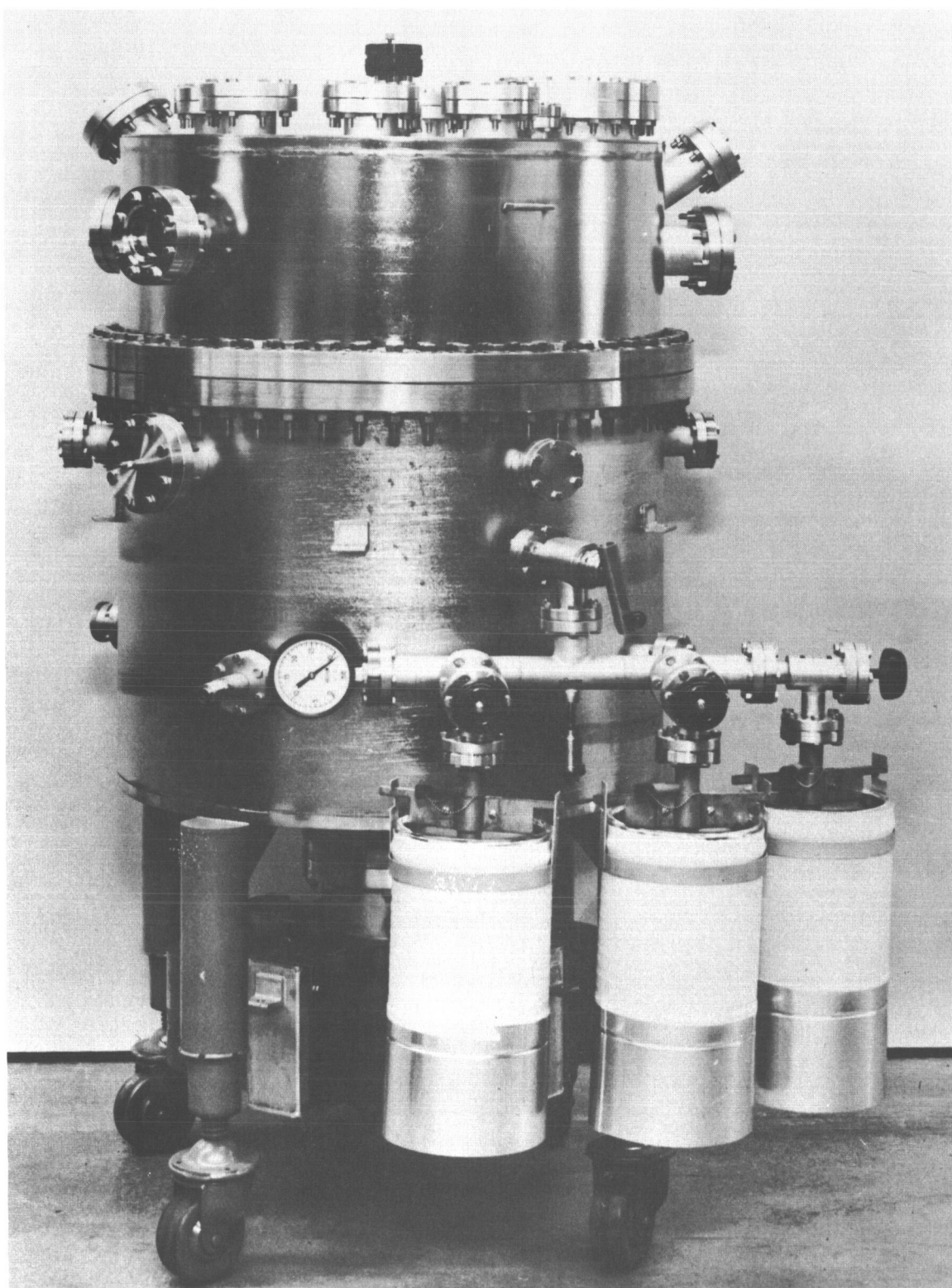


Figure 4. Photograph of environmental chamber
(HAC Photo No. R108257).

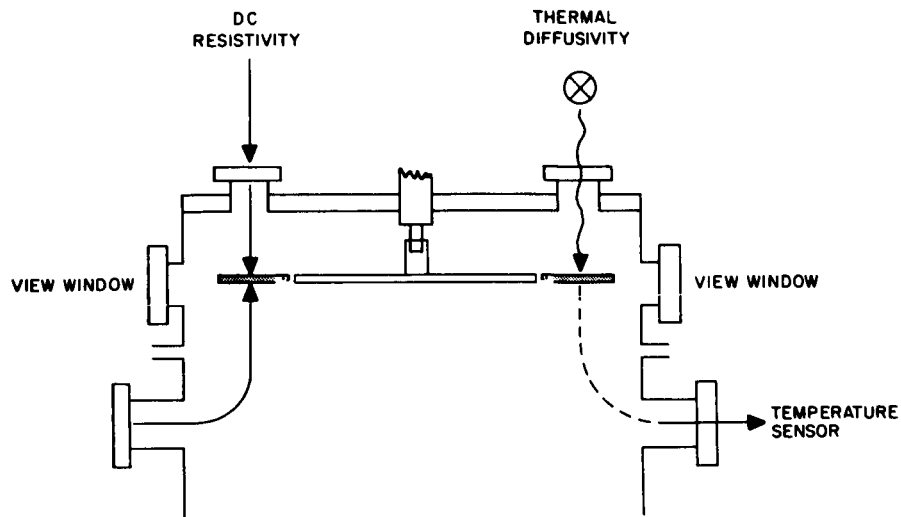


Figure 5. Schematic representation of the dc resistivity and thermal stations.

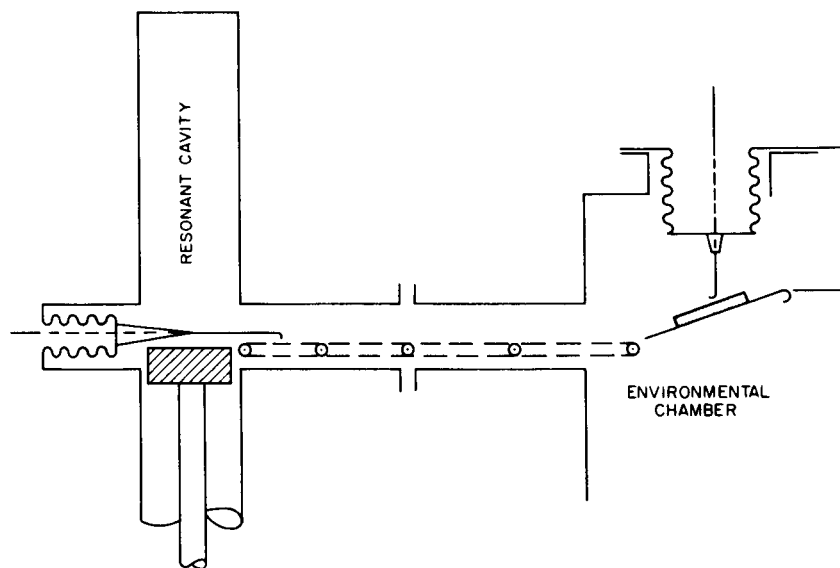


Figure 6. Schematic representation of proposed specimen transfer mechanism to vacuum dielectrometer.

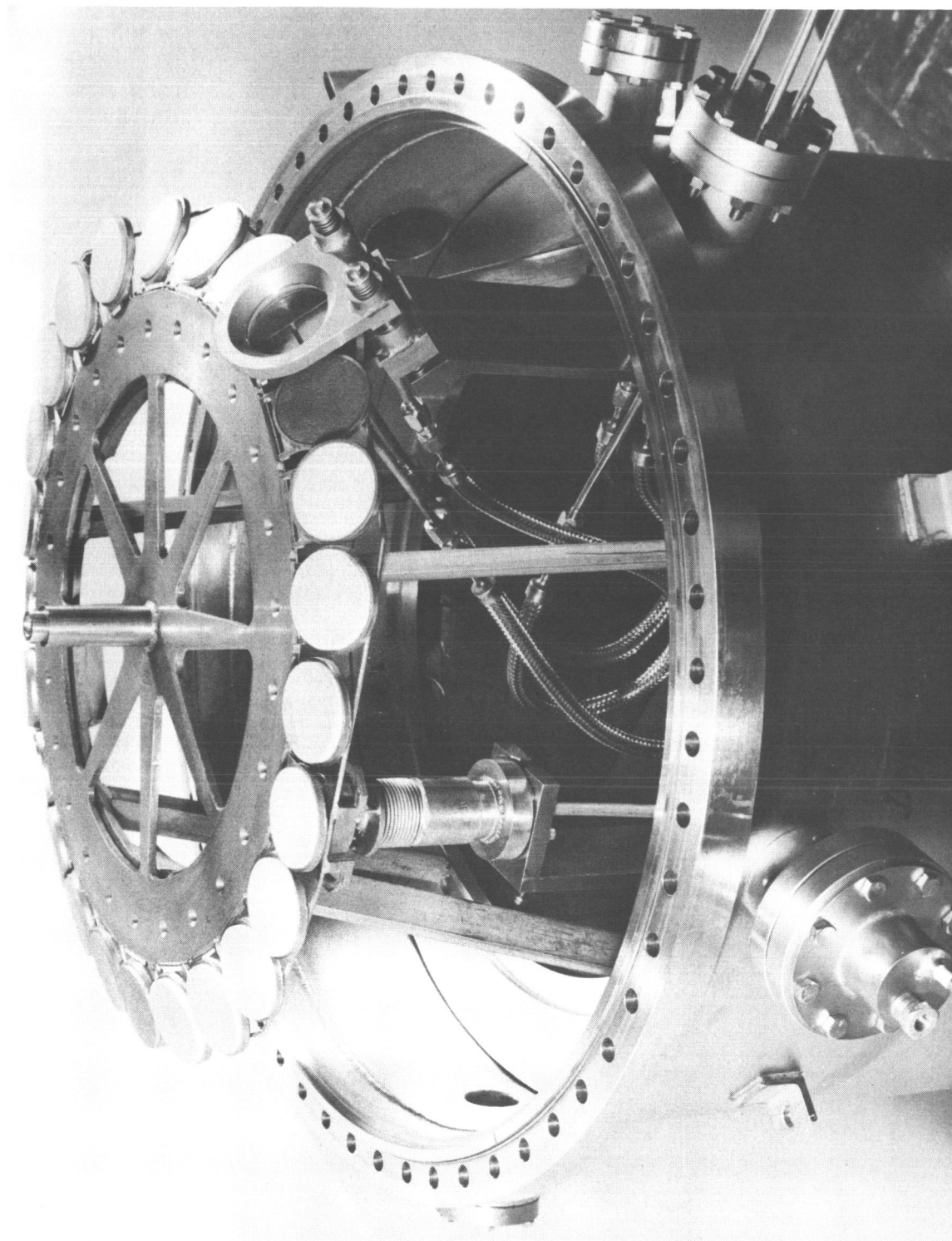


Figure 7. Turntable, irradiation station, and dc resistivity station
(HAC Photo No. R109774).

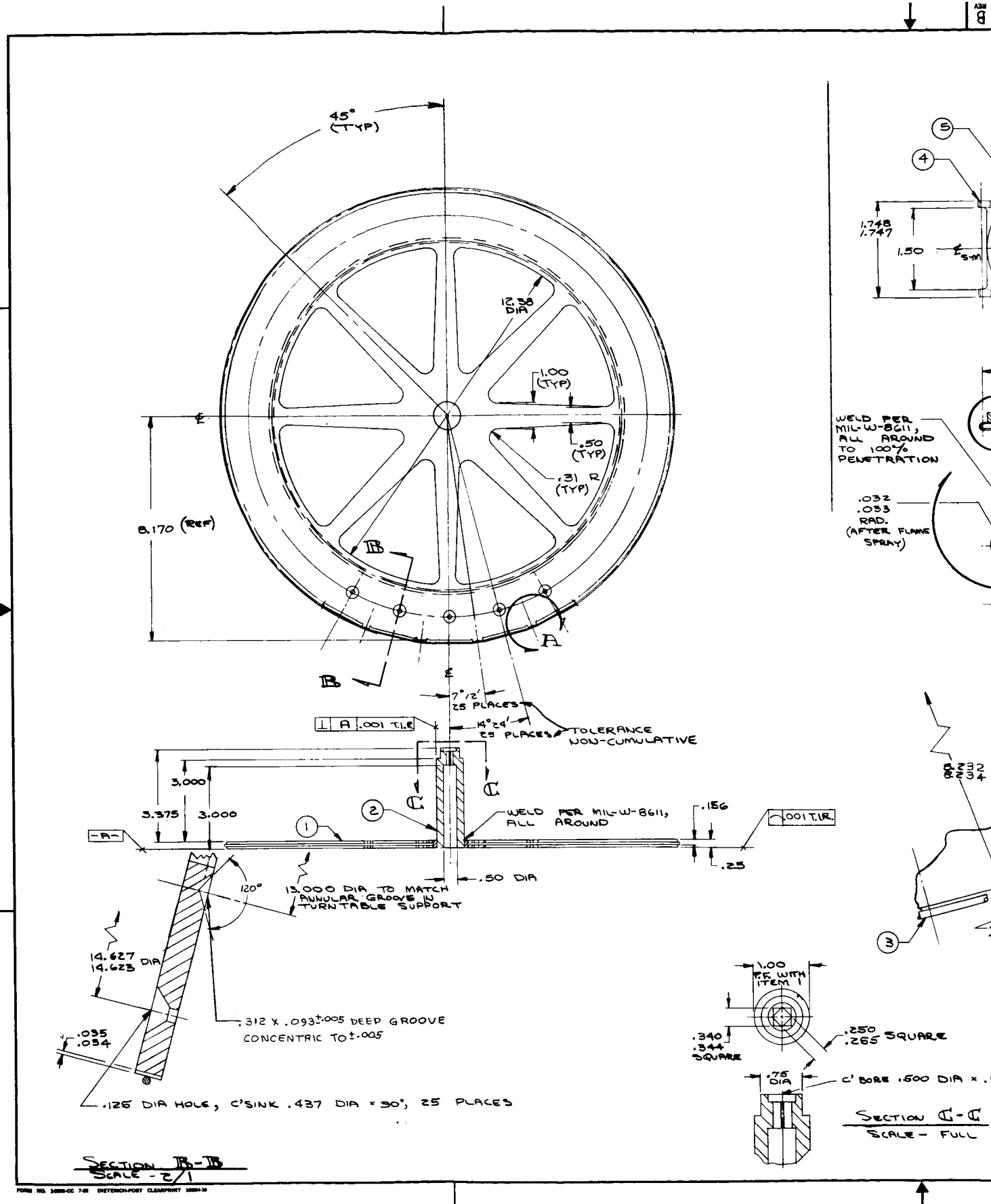
on ceramic (Al_2O_3) ball bearings lying in a groove on top of the support stand. The latter is a 5-leg pedestal anchored on an annular plate along the inside wall of the chamber. Details of the turntable and of the turntable support stand are shown in Figures 8 and 9, respectively.

The turntable support stand is provided with 5 station-positions where the specimen holders come to rest at predetermined angles. A guide rail dictates the angular position of the holders. The following settings were selected for the property measurements outlined herein:

<u>Station</u>	<u>Measurements</u>	<u>Declination Angle</u>
1. Radiation	(Temperature-controlled irradiation)	45 degrees
2. Thermal	Thermal diffusivity Thermal conductivity	0 degree
3. Dielectric	Microwave dielectric constant Microwave loss tangent	20 degrees
4. Optical	Solar absorptance Spectral reflectance	20 degrees
5. DC Resistivity	DC volume resistivity	0 degree

Pumping of the chamber is accomplished by a 400 l/sec sputter-ion pump in combination with a titanium sublimation pump. The latter consists of six titanium filaments that are electrically heated on an optional duty cycle that can be set to operate for 1 minute out of each 2^n minutes, where n is an integer ranging from 0 to 7. The pumping speed of the combined ion-pumping and titanium sublimation is estimated as about 6000 l/sec (for nitrogen).

Roughing down of the chamber prior to activating the ion pump is accomplished by three cryosorption cylinders attached to a common manifold outside of the chamber. A bakeable 1-1/2 inch valve isolates the chamber after it has been roughed down. The absence of oil pumps (mechanical or oil-diffusion) is intentional, to avoid the possibility of contaminating the chamber and the test specimens.



FORM NO. 100-60 7-62 DETROIT-PORT CLEARPORT 1000-10

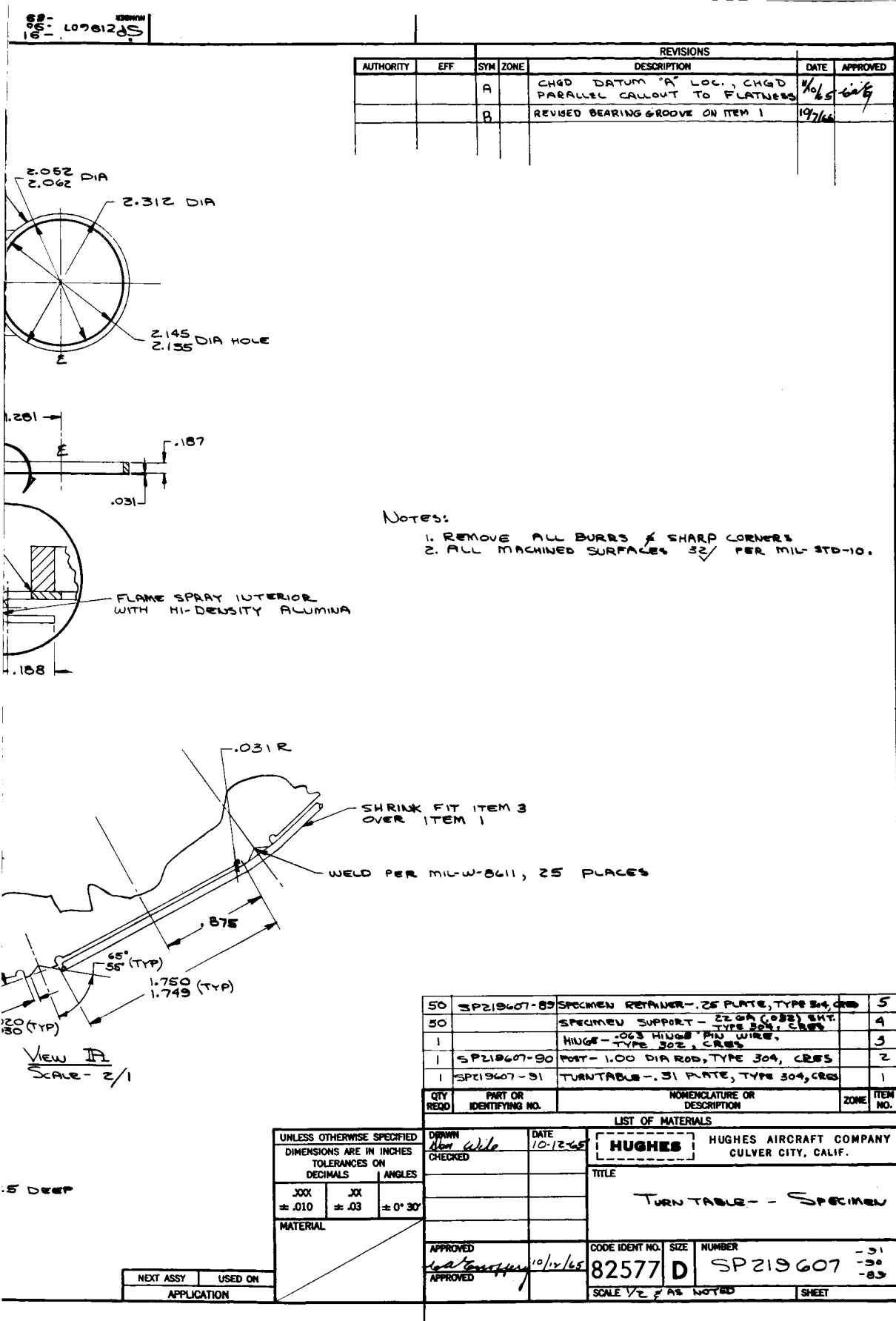
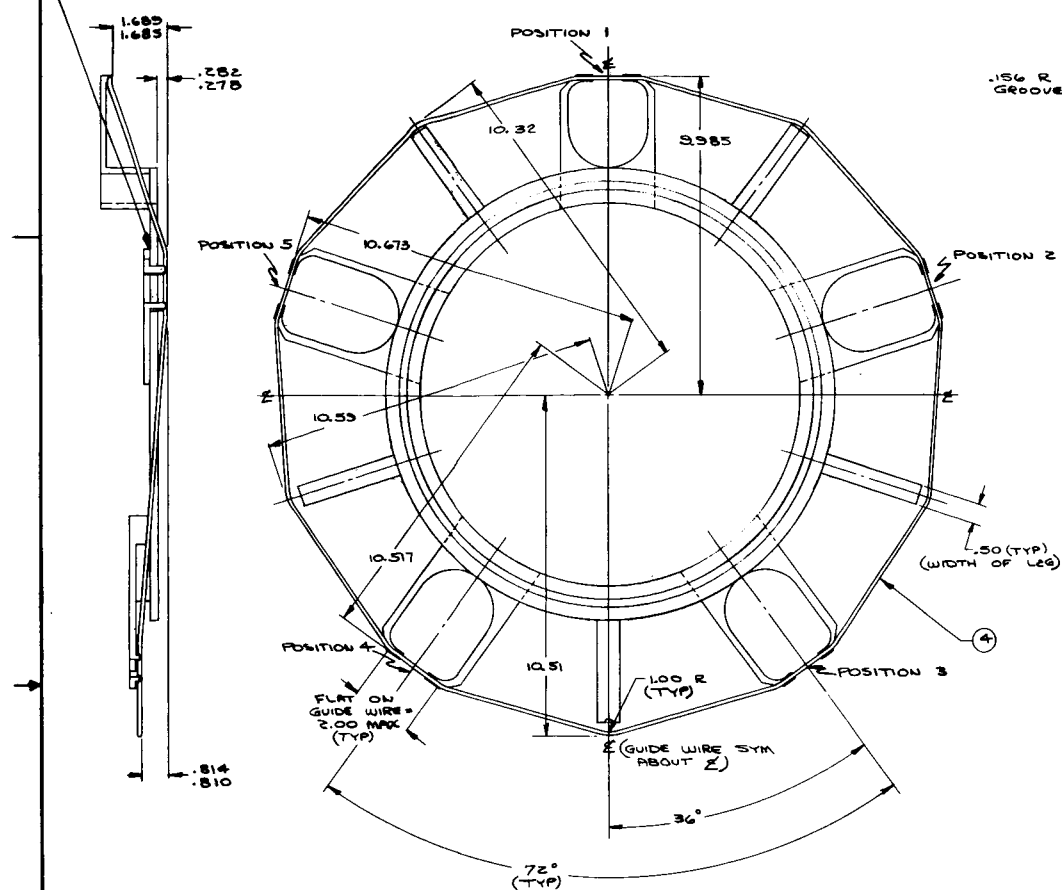
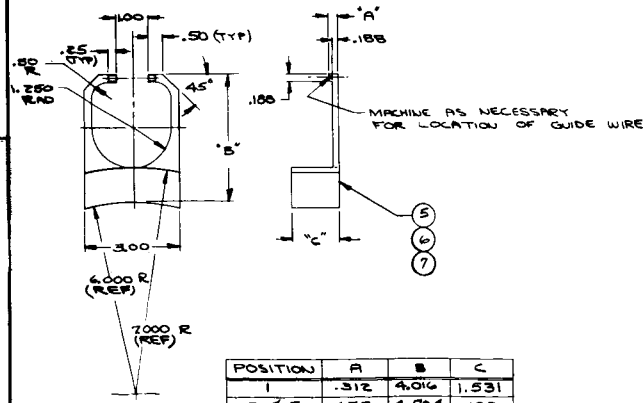


Figure 8. Details of turntable.

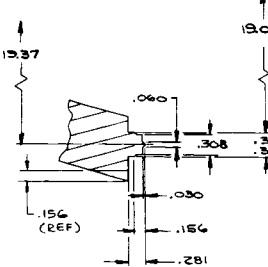
WELD PER MIL-W-8611
TO 100% PENETRATION
(TYP) (5 POSITIONS)



WELD PER MIL-W-8611
TO 100% PENETRATION
(5 PLACES)



POSITION	A	B	C
1	.312	4.016	1.531
2 / 5	.657	4.704	.188
3 / 4	.312	4.548	.655



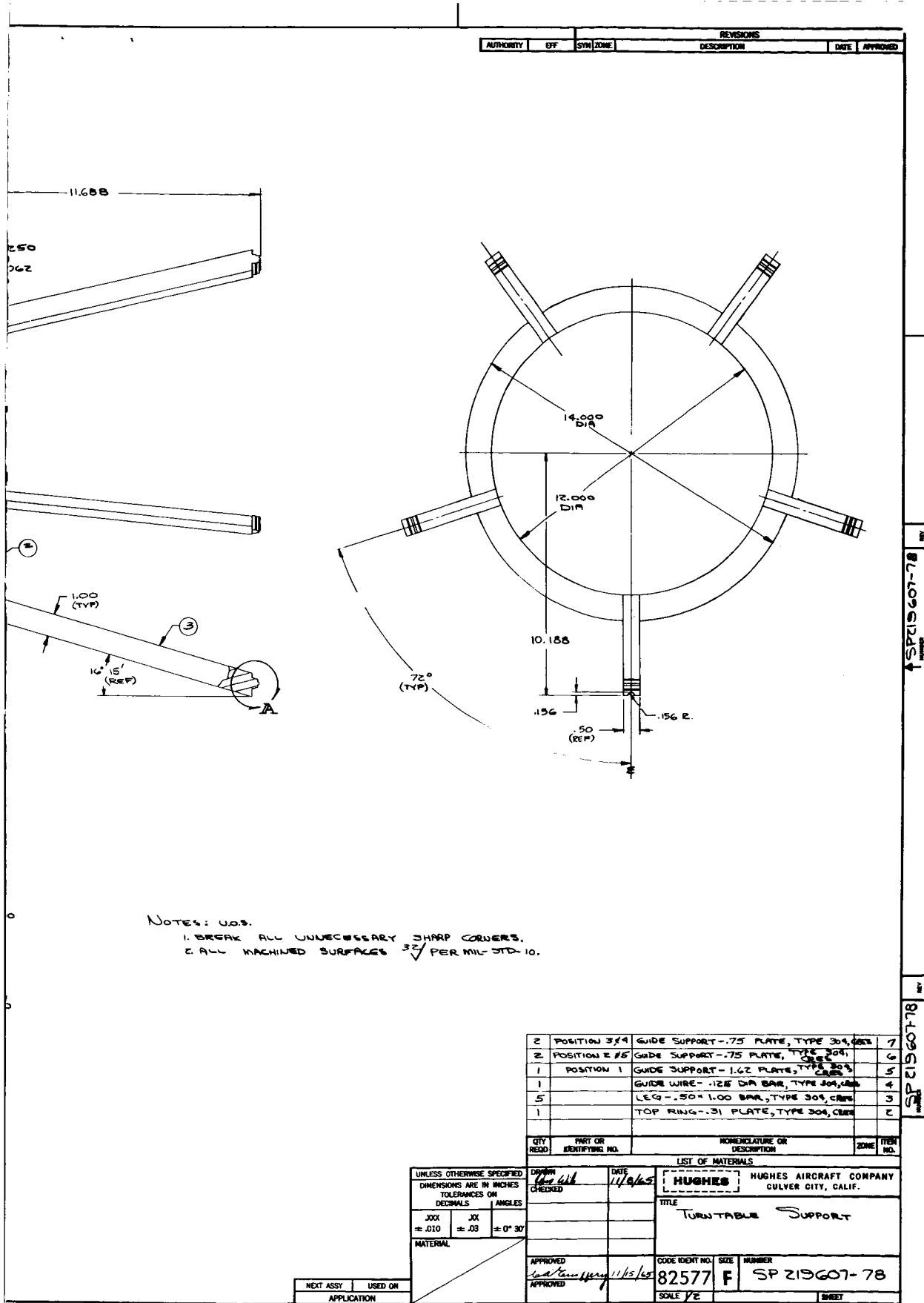


Figure 9. Details of irradiation station.

When the chamber was first completed, it was given a vacuum checkout in an empty condition, that is, without the turntable or specimens. After a preliminary bake, a pressure of 5×10^{-9} torr was obtained after 3 hours of pumping. Subsequently it has been possible to achieve pressures in the 10^{-10} range with specimens in the chamber. Most of the irradiation experiments were conducted in the 10^{-9} to 10^{-7} range, depending on the outgassing characteristics of the specimens, on the radiation dose-rate being applied, and on whether the titanium was subliming or not.

As the titanium sublimation pumping is most effective when LN_2 is circulated through the cryogenic shroud, LN_2 flow was always used during the irradiations. This imposed one disadvantage, however, for the specimens radiated some heat to the shroud and their measured temperature tended to be about 10°C rather than room temperature. In the future, a thermal baffle can be inserted between the specimens and shroud.

2.2 IRRADIATION STATION

Details of the irradiation station are given in Figure 10. The station can be seen in the photograph of Figure 7. During irradiation, a spring-loaded annular clamp holds the specimen firmly against a thermal sink. The clamp is provided with a 2-inch diameter window to permit the radiation to bathe most of the top face of the specimen. A pneumatically operated bellows is used to unclamp the test specimen and free it to move (within its holder) to a property measurement station.

Thermocouple wells in the heat sink and in the clamp are designed to hold thermocouples that contact the rear face and the top periphery of the specimen. The thermocouples are cemented into place with an aluminum phosphate binder. For irradiation at low temperatures (ca. -195°C) one can use liquid nitrogen; for the high temperature ($+180^\circ\text{C}$) studies a suitable thermostating fluid may be used.

As shown in Figure 10, the original design of the fluid feeds for the heat-sink support-block, and the compressed N₂ (or air) feed for the bellows called for 1/4-inch rigid stainless steel tubes. These tubes provided excessive drag on the up and down movement of the heat sink. To overcome this problem they were removed and replaced by flexible metal hose*. Connection of these conduits to the heat sink and to the vacuum flange on the chamber wall was made with Imperial 37-degree flared fittings.

With 15 psi in the bellows (corresponding to vacuum conditions in the chamber), the clamp-window compresses the specimen firmly against the support block. With an additional 30 psi, the clamp rises, the support block recedes slightly, and the specimen holder (and specimen) is disengaged and free to move.

The project plans call for irradiation with ultraviolet light, with protons and with electrons, singly and combined. To satisfy these requirements, it was felt desirable to design the station around a 45-degree specimen position. Depending on the radiation source, the radiation could be brought either directly into the chamber by direct vacuum-coupling or transmitted in through a suitable window (e. g. , sapphire for the ultraviolet light).

To utilize the 1 Mev electron beam generator available at Hughes Aircraft Company, it was decided to utilize a thin foil window in the top, horizontal, radiation part of the chamber (see Figure 3). It had been hoped to use a beryllium window in a conventional stainless steel flange. After several unsuccessful attempts to obtain a vacuum-tight seal, the LND Corporation (Long Island, New York) supplied us with a 2-1/2 inch diameter, 5-mil beryllium foil window sealed in a 4-1/2 inch outside diameter vacuum flange. After checking the system out with a leak detector, it was mounted on the chamber and subjected to a pumpdown. Unfortunately, about 30 minutes later the window failed and shattered into numerous small pieces. Attempts to develop a

*Flexonics Division of Calumet & Hecla, p/n 0320-016-500 with 1/4-inch AN 818 swivel nut at each end.

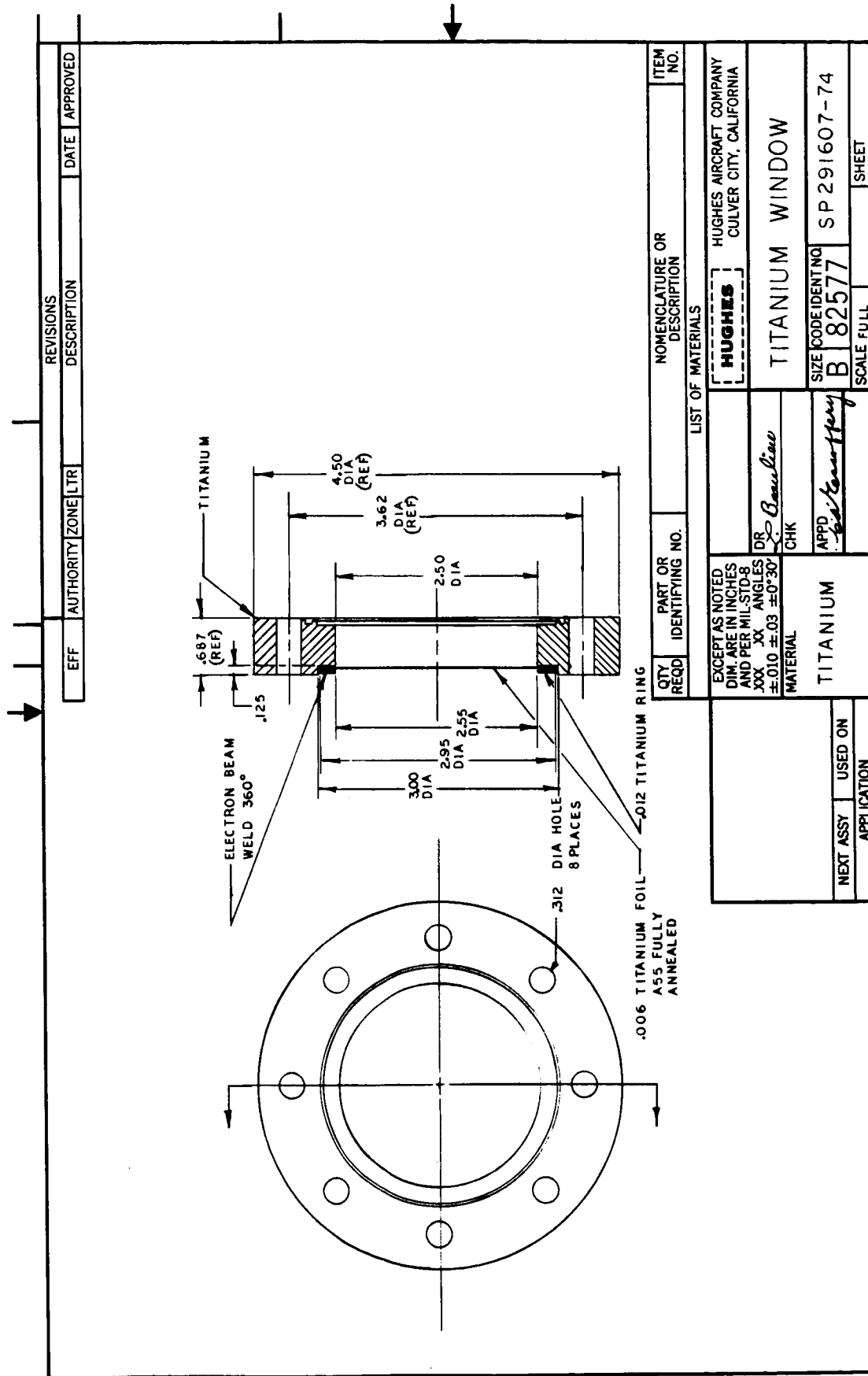
large area window from beryllium were discontinued in favor of titanium (6-mil foil).

Again, it was found difficult to obtain a reliable seal of the foil to the stainless steel. Various designs and fabrication procedures were tried that included vacuum furnace brazing, induction brazing and electron beam welding. Since titanium is very reactive and combines readily with active elements and compounds, it must be protected from air and other active gases during brazing operations.

Titanium also reacts very rapidly with practically all of the brazing filler metals, and this reaction causes the formation of intermetallic compounds in the joint. When excessive amounts of these intermetallic compounds are present, the shear strength and ductility of the joints are lowered.¹ Fine silver was used as the filler metal. It wets and adheres readily to titanium and is free flowing at temperatures above 1760°F. The TiAg compound that is formed is less harmful to the properties of the brazed joints than are some other compounds.¹ Silver plating was also used to cover the surfaces of the stainless steel flange and of intermediate steel retaining rings.

Success was finally achieved by constructing the entire vacuum flange (4-1/2-inch OD by 2-1/2-inch ID) out of titanium stock and then electron beam welding the 6-mil titanium foil over the 2-1/2 diameter opening. An elegant, neat and vacuum-tight window resulted. Details of the window are shown in Figure 11.

To insure that specimens within the chamber other than the test specimen do not receive a significant dose during irradiation periods, adequate shielding and collimation must be provided. For the irradiations with the 1 Mev electron generator, the electron beam was passed through a hole bored in an aluminum plate (outside the chamber) at the generator window, and then through an aluminum collimating tube (inside the chamber) extending from the chamber window to the specimen stand. Distance from the generator to the specimen was set at 10 inches of which 3 inches were through air.



FORM 11063B-CS-00

Figure 11. Titanium window.

2.3 OPTICAL PROPERTIES STATION

Figure 12 outlines the optical station to be used for measuring the solar absorptance of thermal control coatings. Spectral reflectance values are obtained by means of an integrating sphere that is raised and lowered pneumatically. Numerical integration of spectral reflectance values over the 0.29 to 2.6 micron range yields the solar absorptance.

Monochromatic light enters the integrating sphere via a sapphire window, strikes the specimen surface along the lower edge of the sphere, and after successive internal multireflections is picked up on a suitable detector. The test specimen is inclined at an angle of 20 degrees from the horizontal to minimize energy loss by specular reflection back through the entrance port.

Figures 13 and 14 are photographs of the integrating sphere, Figures 15 and 16 give details of the design, and Figure 17 describes the support and pneumatic lift mechanism. The square support rods shown in Figure 14 were subsequently changed to round pins.

Appendix B analyzes the sphere design in detail. Over 99 percent of the internal surface is utilized for reflections, and high accuracy and precision for solar absorptance measurements can be expected.

2.4 THERMAL PROPERTIES STATION

Measurements of thermal diffusivity and thermal conductivity can be made using a "pulse" technique.² This method lends itself readily for studies in a vacuum chamber. For a pulsed energy source, it is possible to use a xenon arc lamp, a laser, or, described in Section 4.2, a photographic flash bulb.

Insufficient time was available to finalize the design of the thermal properties station and install it in the chamber. A number of exploratory studies were done in air, outside of the chamber, however, and these are reported in Section 4.2.

2.5 DC RESISTIVITY STATION

It was recognized from the outset that measurements of resistivity (and also of dielectric properties such as dielectric constant and loss)

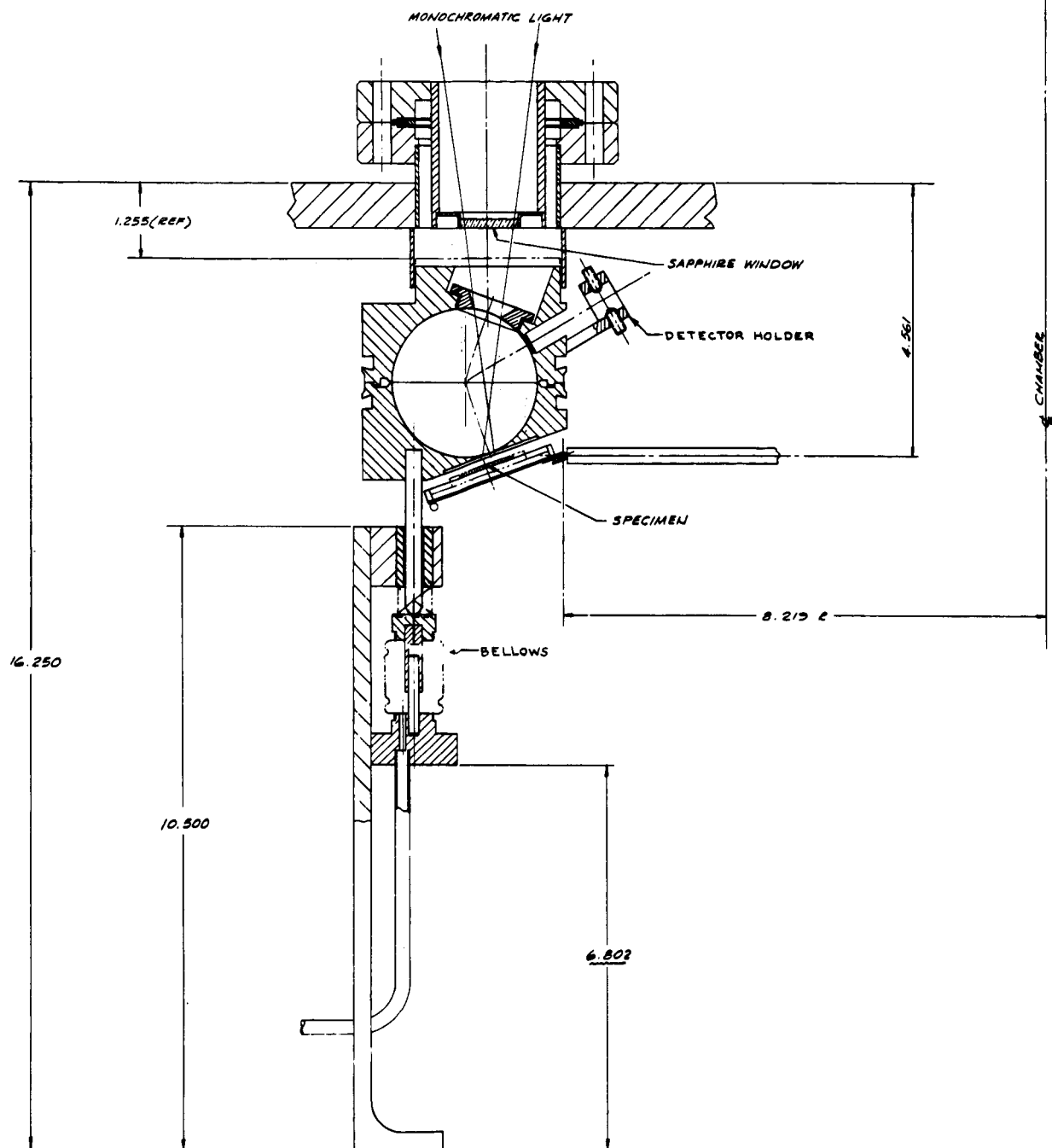


Figure 12. Details of optical station.

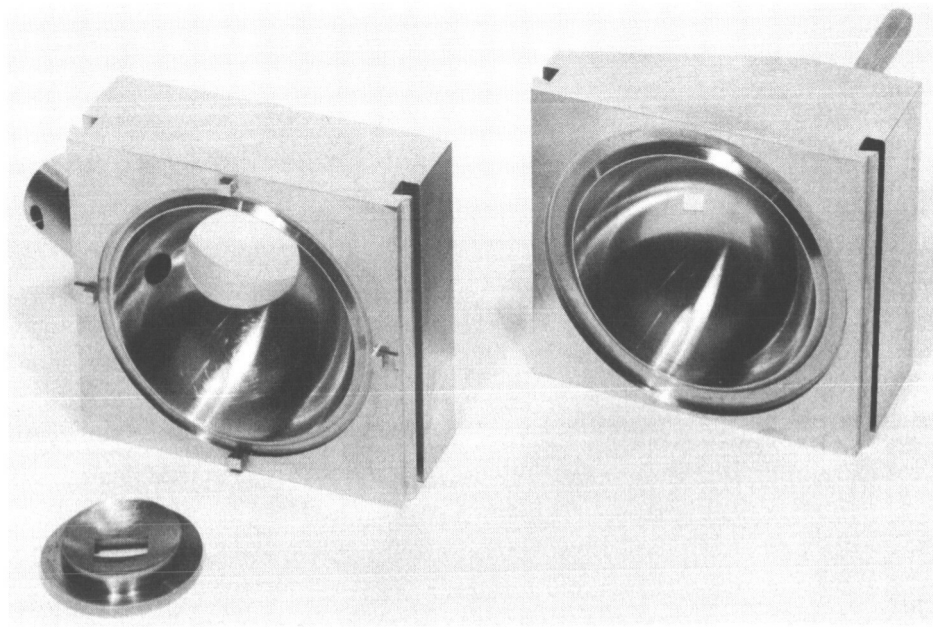


Figure 13. Interior view of integrating sphere. (HAC Photo No. R106231).

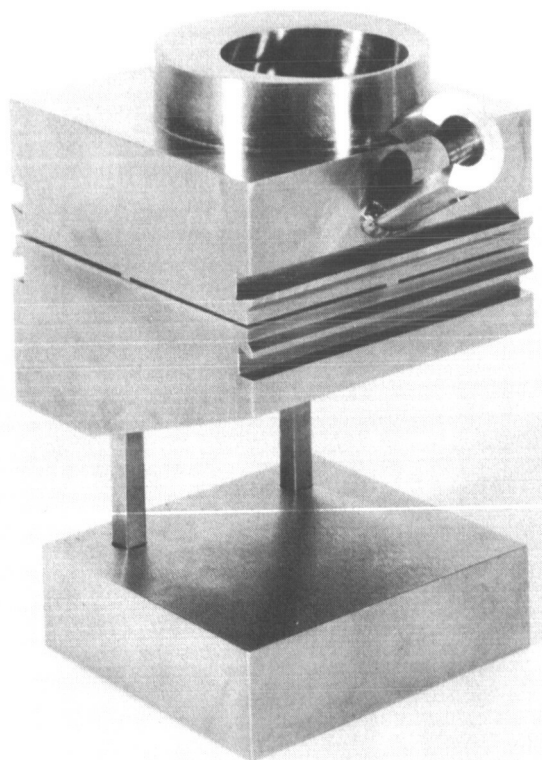
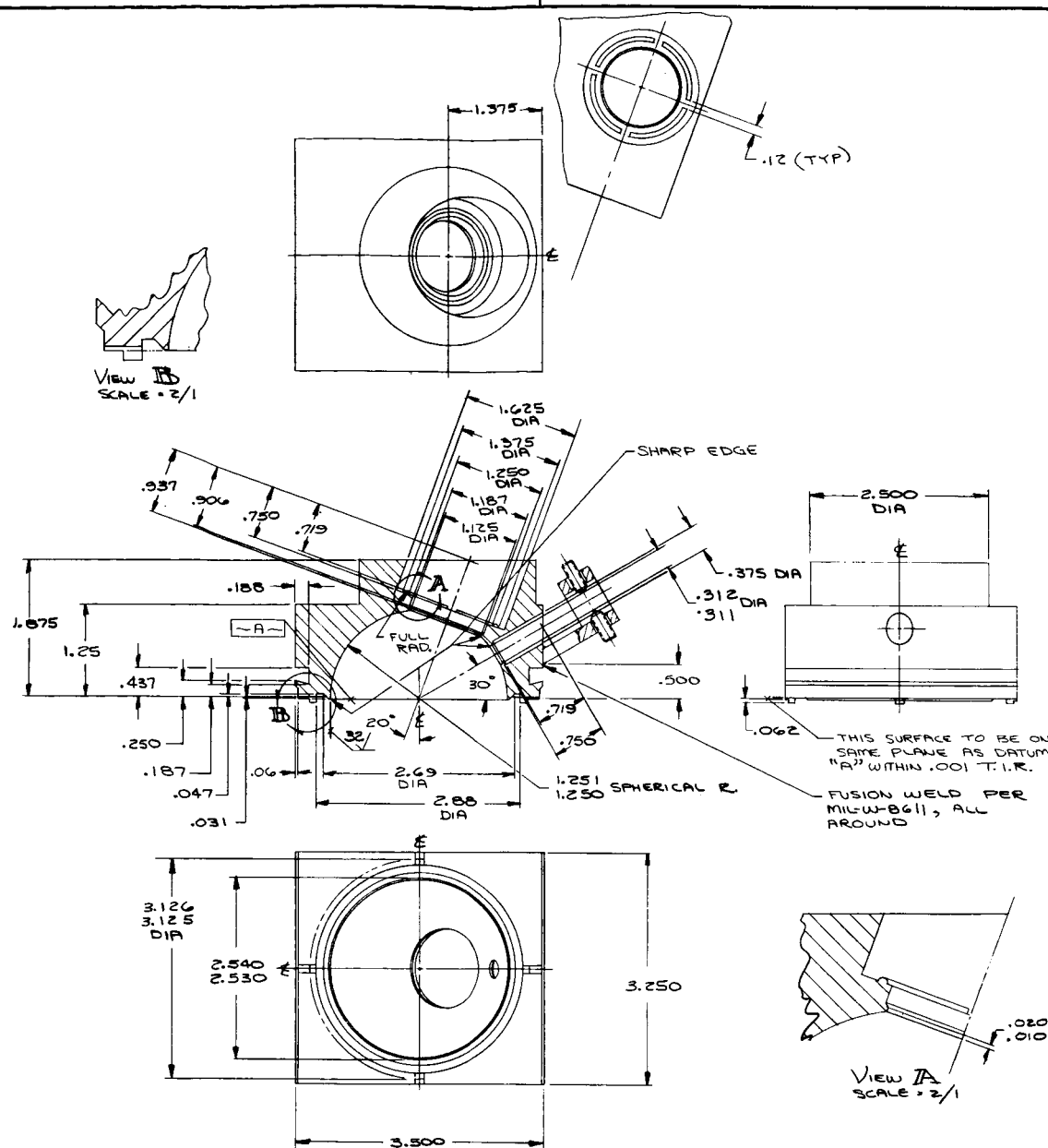
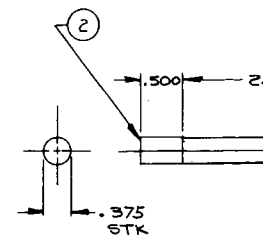
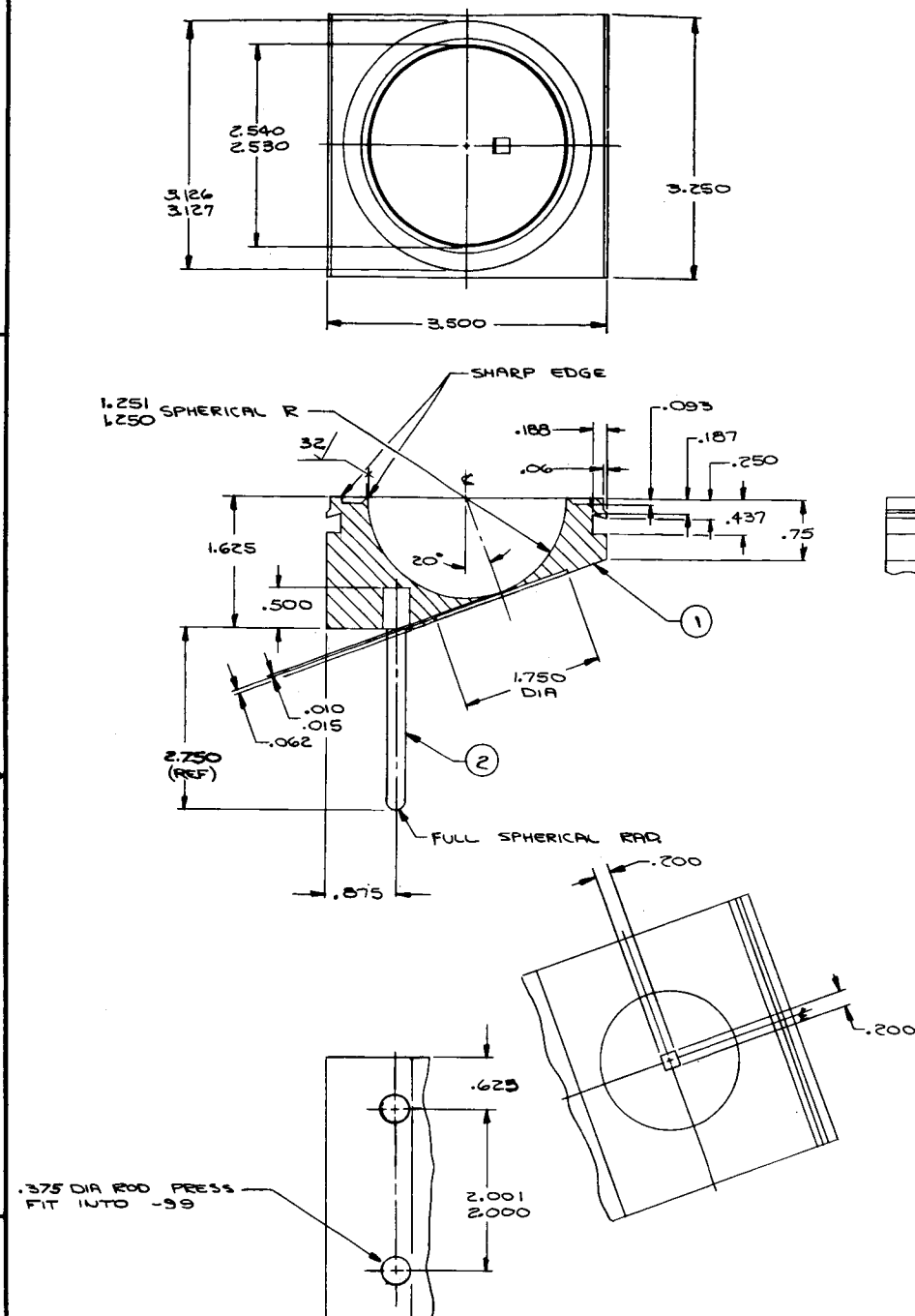


Figure 14. View of assembled integrating sphere (without detector) (HAC Photo No. 106230).



DET-97

2. ALL MACHINED SURFACES TO BE 32/ PER MIL-STD-10.
1. BREAK ALL UNNECESSARY SHARP EDGES.
- NOTES :



2. ALL MACHINED SURFACES TO BE $32/\sqrt{\text{PER MIL-STD}}$
 1. BREAK ALL UNNECESSARY SHARP EDGES.
 NOTES: U.O.S.

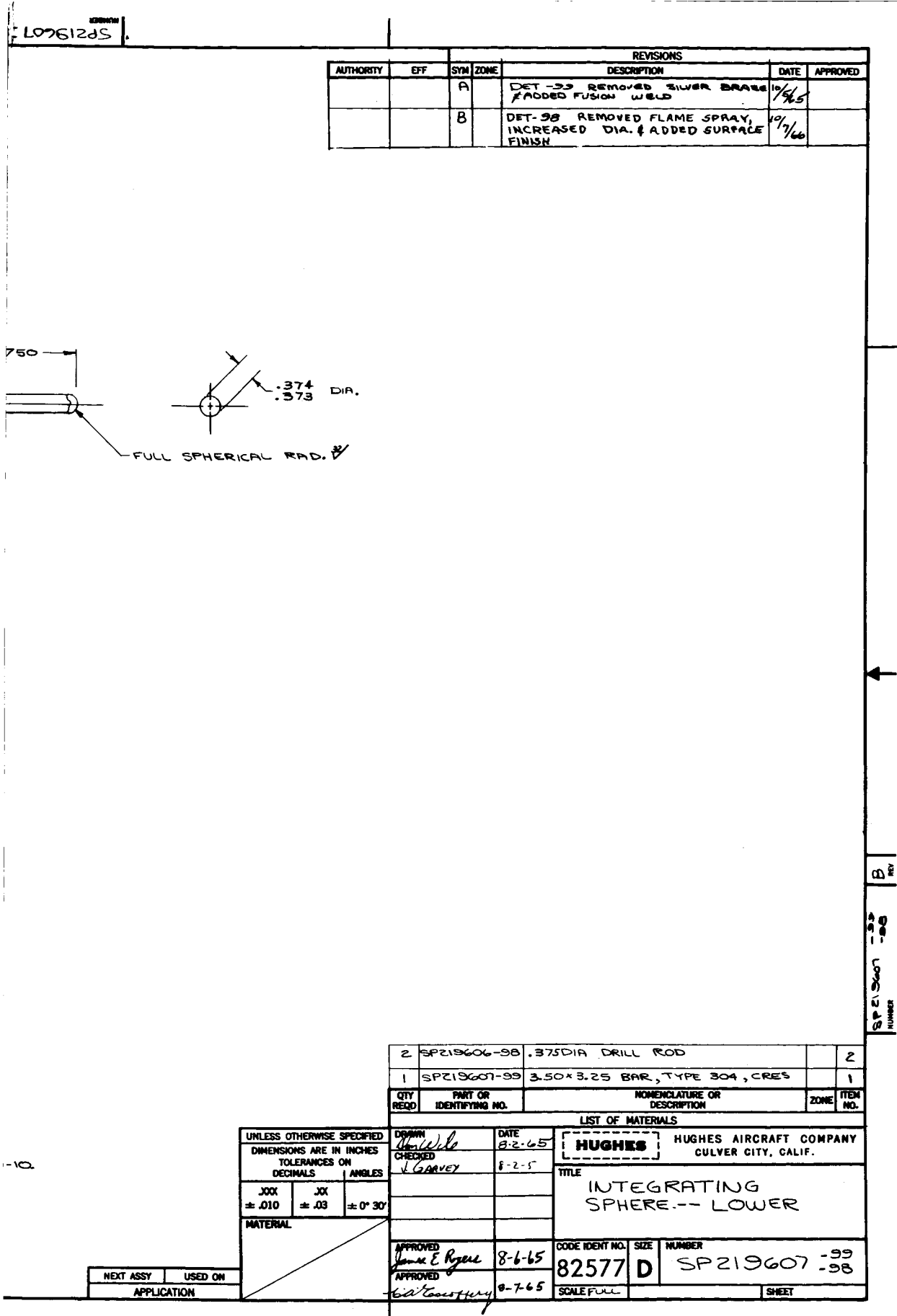


Figure 16. Details of integrating sphere (lower half).

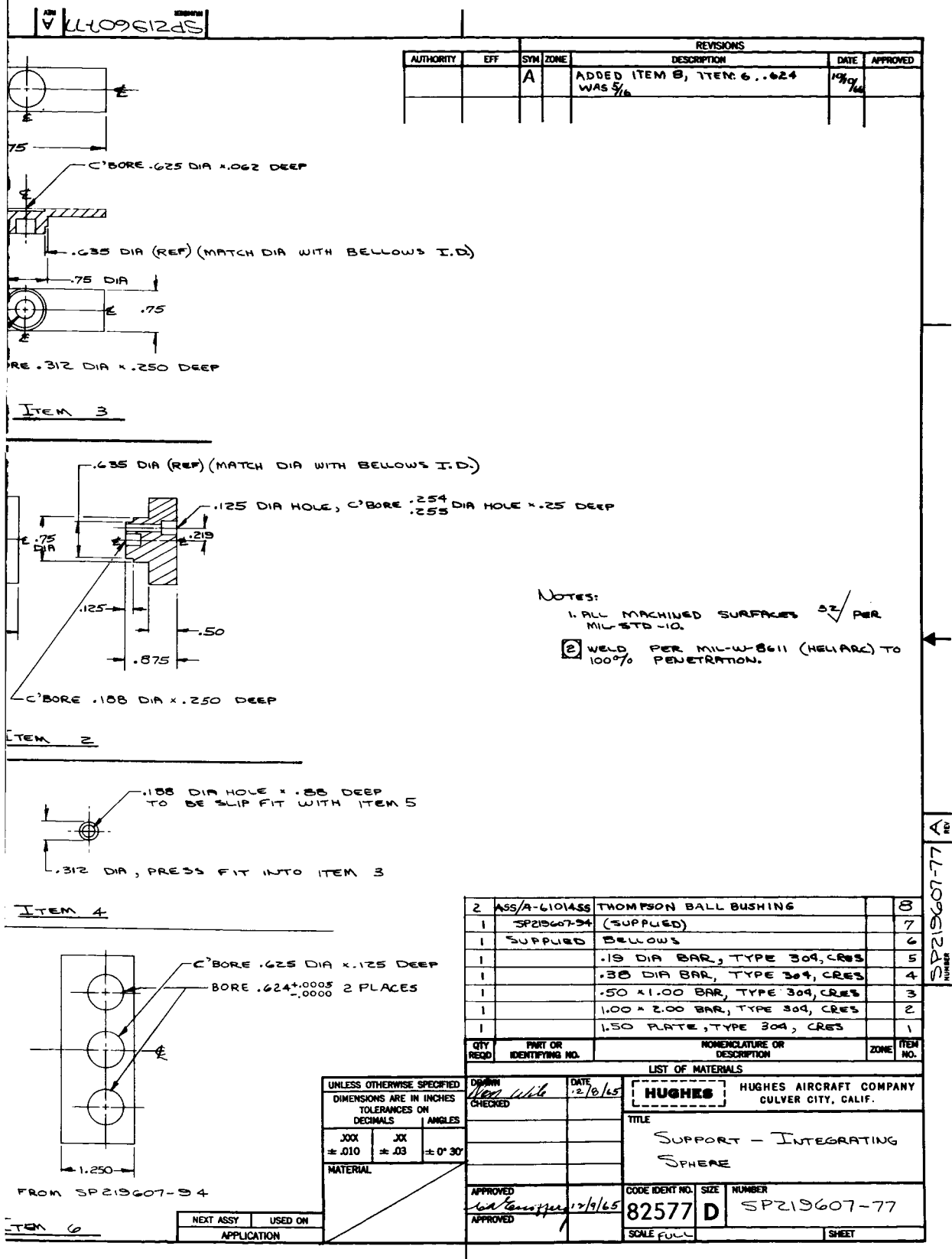


Figure 17. Details of integrating sphere support.

would have to be made directly on test specimens without attached electrodes; i. e. , electrodes applied by vacuum deposition, conductive paint, or pressed foils, for instance. This requirement was imposed by the need to keep the surfaces free to the irradiation.

The method proposed³ for measuring permittivity was a microwave resonant-cavity technique which uses non-electroded specimens, but the test specimens are fairly thick, on the order of 3/8-inch. Consequently, it was felt desirable that any proposed dc volume resistivity technique should be applicable to fairly thick specimens. Exploratory experiments were therefore made on non-electroded thick specimens, using the guard-ring technique outlined in standard procedures.⁴ These studies, described in Section 4.3 were successful and allowed us to design and build the set-up used in the environmental chamber.

Figures 18a and 18b present details of the resistivity station. The cross section of the lower half is such that it can be installed or removed through the flanged opening in the side of the vacuum chamber.

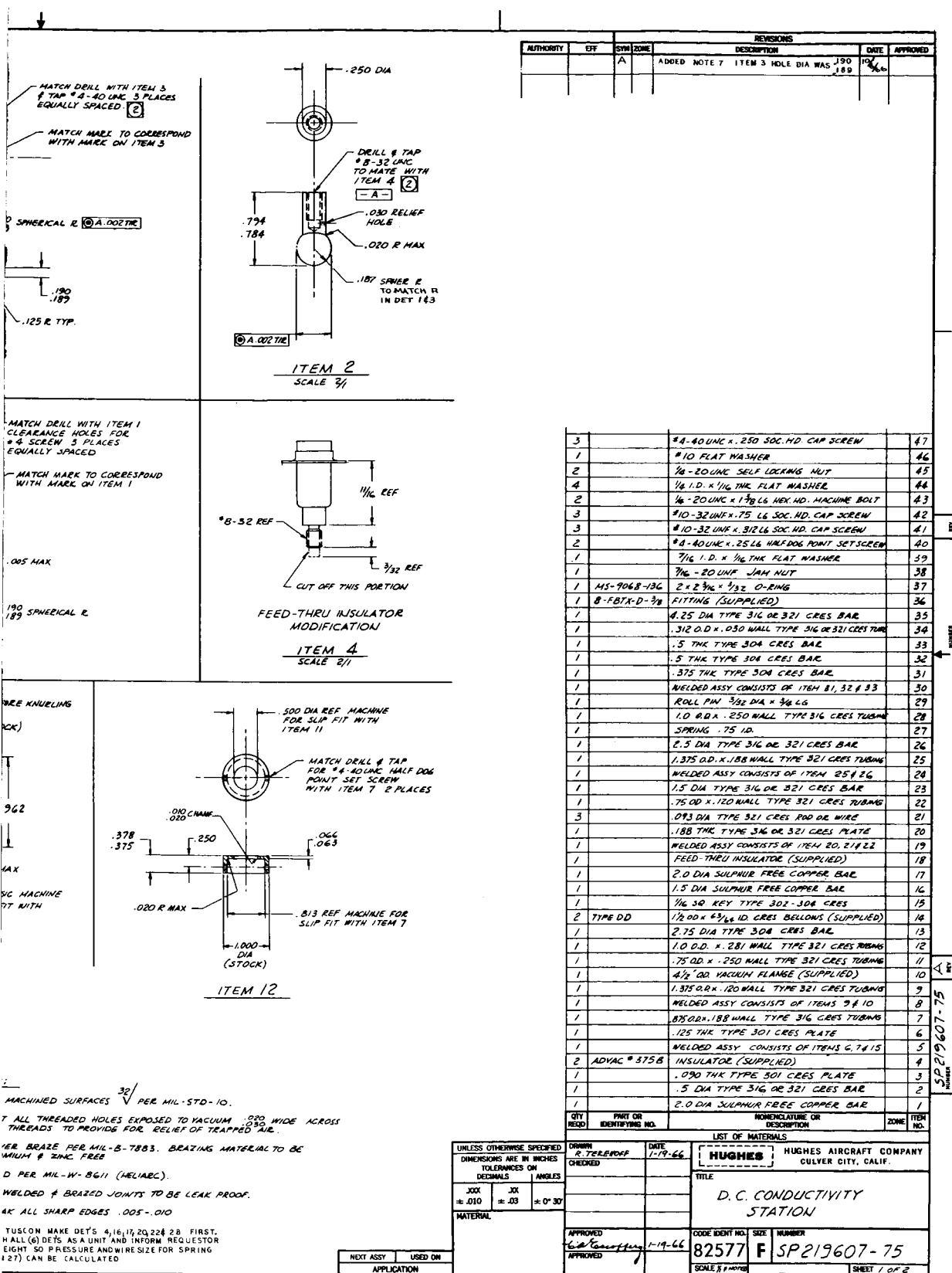
Figures 19 and 20 illustrate a specimen in the resistivity station. Under remote control, the pneumatically-operated bellows expands, raises the lower (guarded) electrode and presses the specimen against the upper, fixed, electrode. The latter can be prepositioned by means of an adjustable jam nut. The contact area of the guarded electrode is 10 cm².

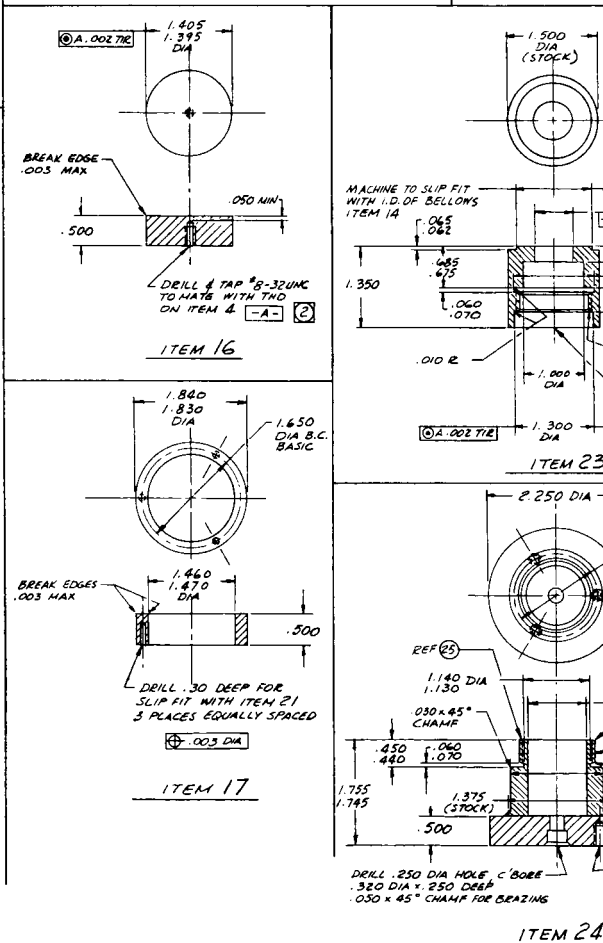
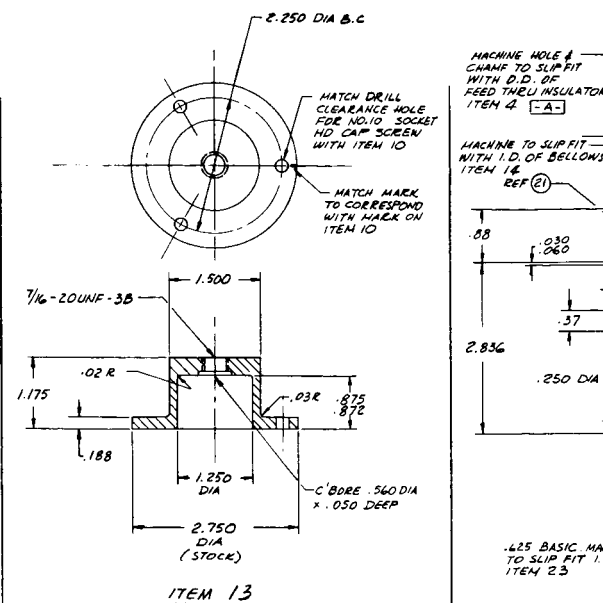
Figure 21 illustrates the electrical circuit used in measuring dc resistivity. The voltmeter is provided with two scales covering the range 0-500 and 0-1500 volts, respectively. The electrometer, Keithley Model 210 with Model 2008 decade shunt, can be read to 8×10^{-13} amperes full scale. Minimum detectable reading is about 8×10^{-15} amperes.

2.6 DIELECTROMETER STATION

One of the objectives of the program is to measure the complex permittivity of specimens exposed to a simulated space environment. The complex permittivity, ϵ^* , is defined by

$$\epsilon^* = \epsilon' - j\epsilon'' \quad (1)$$





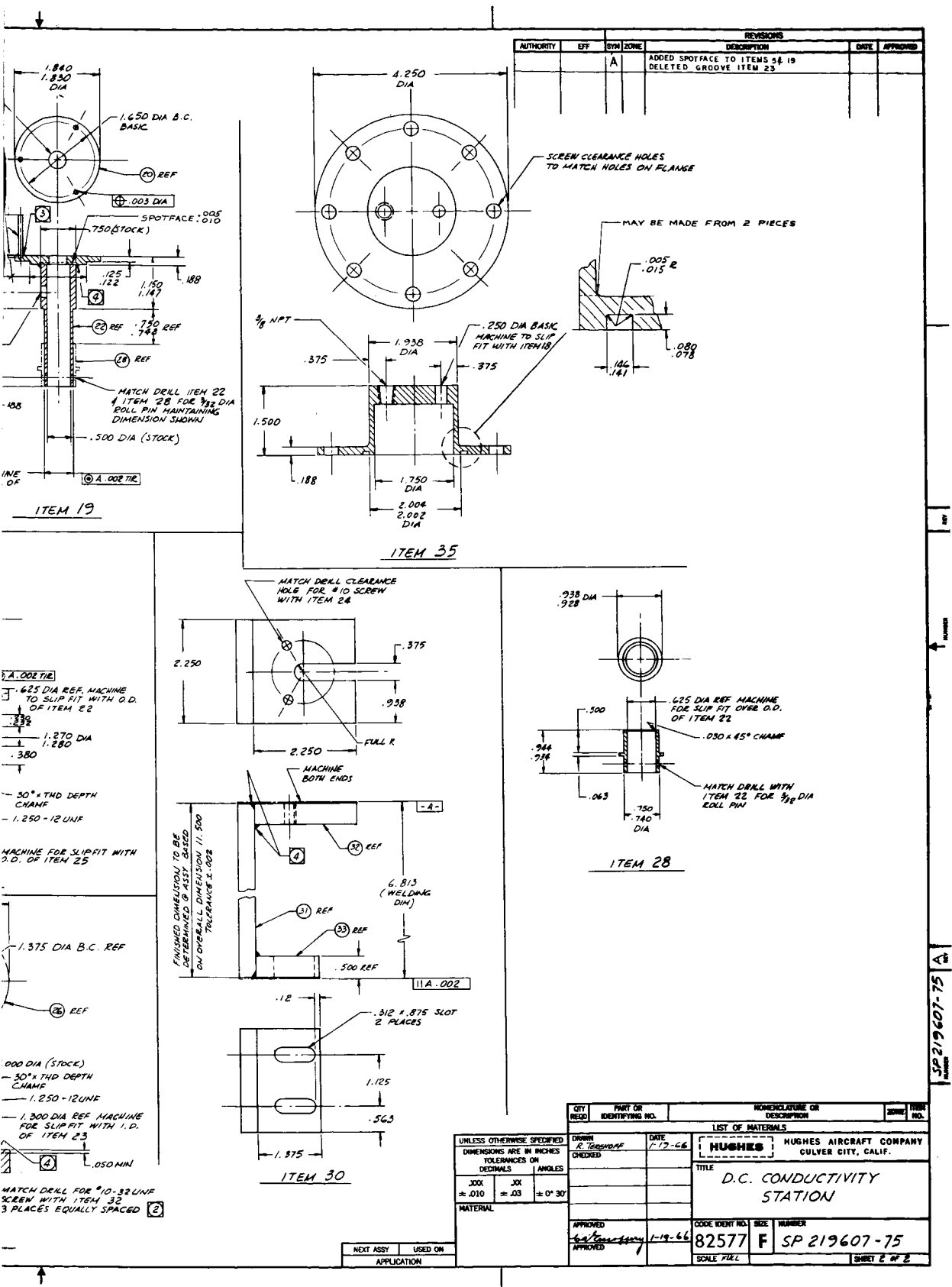


Figure 18. (Continued) (Sheet 2 of 2).

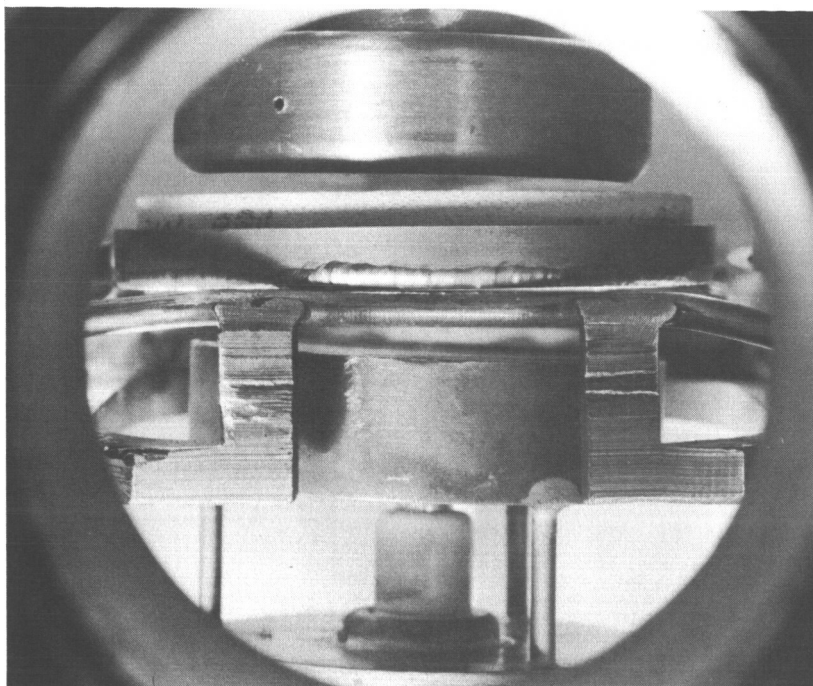


Figure 19. DC resistivity station, open
(HAC Photo No. R109775).

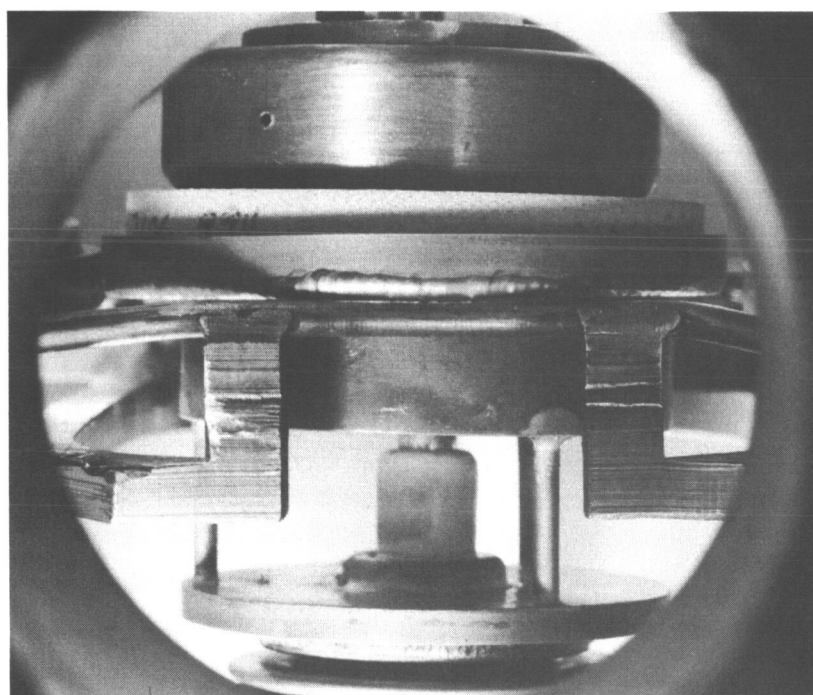


Figure 20. DC resistivity station, closed
(HAC Photo No. R109773).

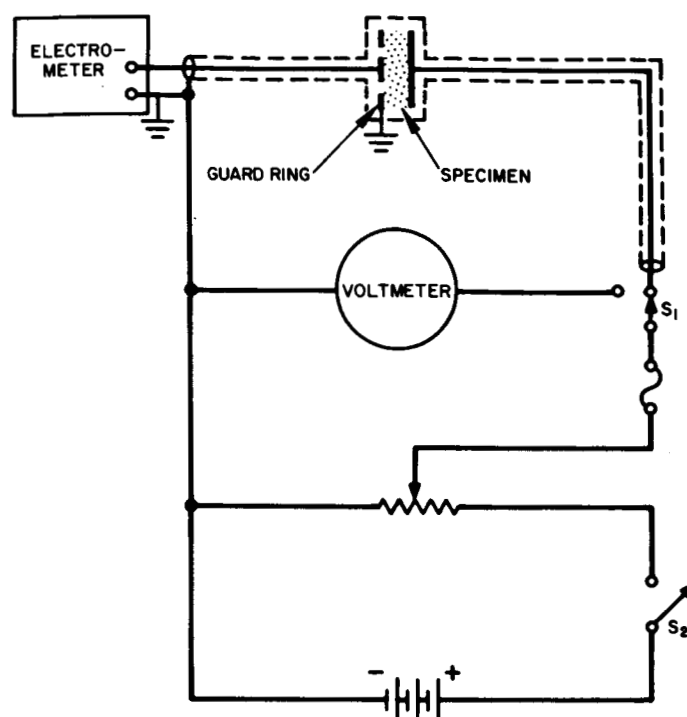


Figure 21. Circuit diagram for measuring dc resistivity.

The real part, ϵ' , is called the dielectric constant. It is more convenient, however, to measure and express it in terms of its value relative to the permittivity of vacuum (ϵ_0). The relative dielectric constant, $\bar{\epsilon}'$, is thus defined by

$$\bar{\epsilon}' = \frac{\epsilon'}{\epsilon_0} \quad (2)$$

and is obviously a pure number.

The imaginary part of Equation (1), ϵ'' , is called the loss factor. Again, it is more convenient to express it in terms of its ratio to the real part, yielding the loss tangent, defined by

$$\tan \delta = \frac{\epsilon''}{\epsilon'} \quad (3)$$

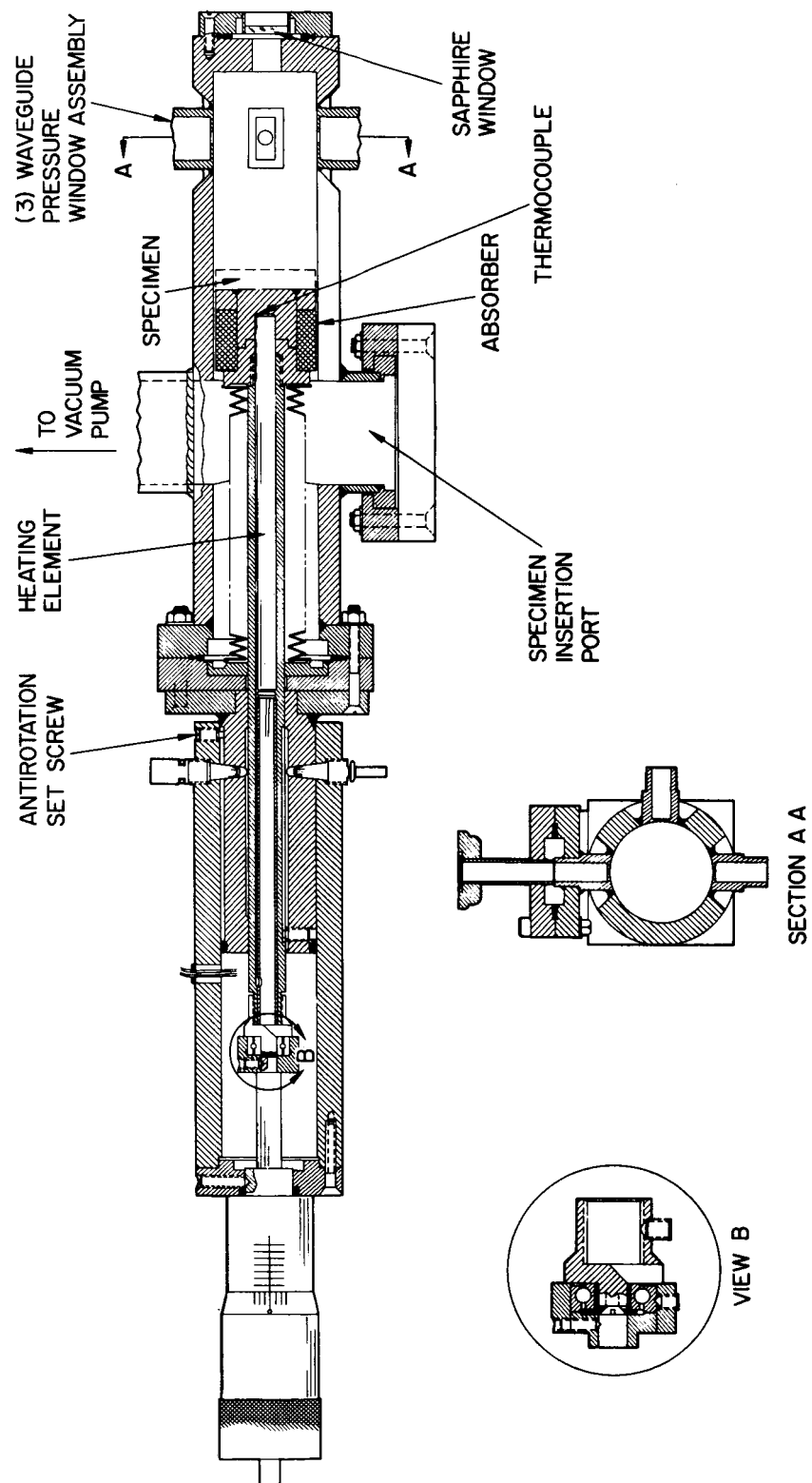


Figure 22. Vacuum microwave dielectrometer design.

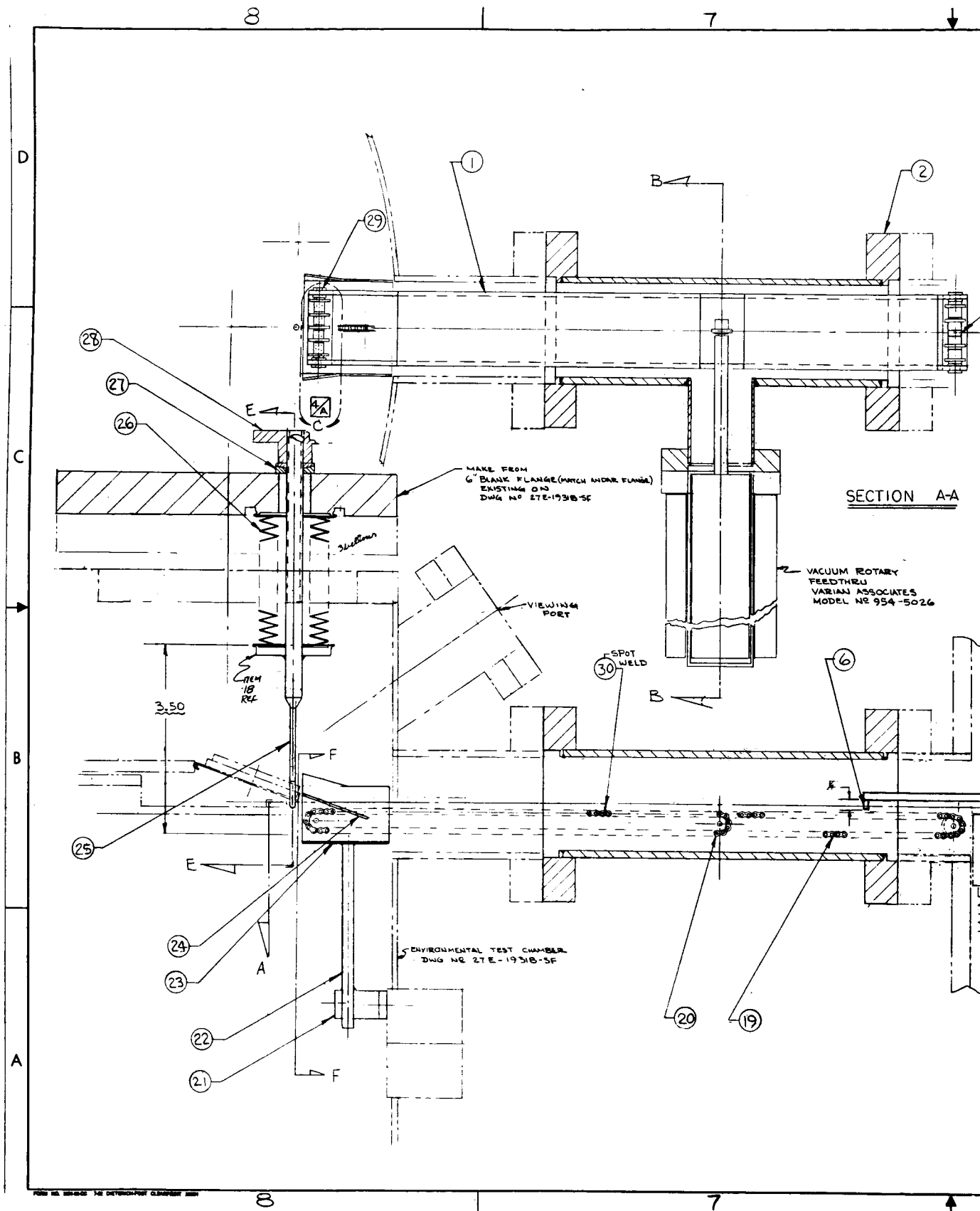
where δ , the loss angle, is the angle between the total current vector and the charging current vector. The loss tangent is also called the dissipation factor.

While the permittivity of vacuum is a constant (8.854×10^{-12} farads/m), the permittivity of air varies with temperature, pressure and moisture content. For many purposes, however, the two values can be considered equal, and it is common to assign a value of 1 to the relative dielectric constant of air. (According to Reference 5, dry air has a value of 1.000569.)

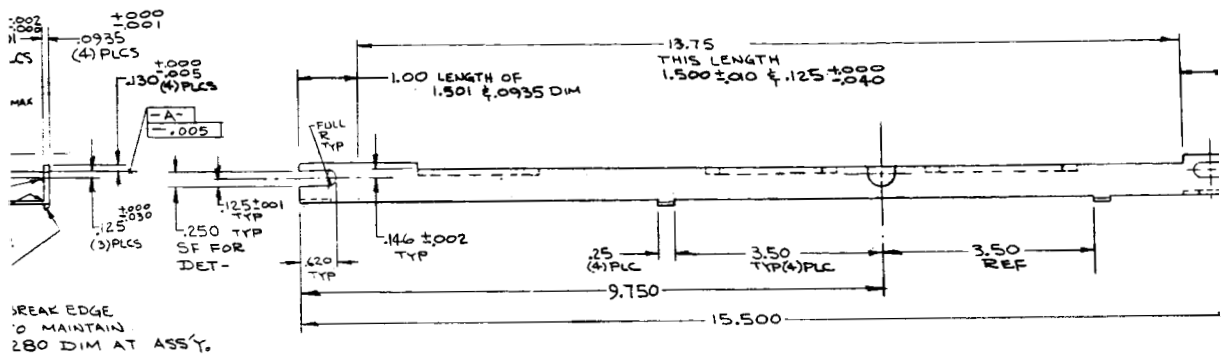
Microwave methods of measuring permittivity are particularly convenient because the test specimens do not require electrodes. In our program, the measurements are made at 9.28 GHz (9.28×10^9 cps) in a resonant cavity TE_{01n} dielectrometer designed and fabricated previously.⁶ Figure A-2 (in Appendix A) is a photograph of the dielectrometer, and Figure 22 is a cross-sectional drawing. Details of the instrument have been presented elsewhere.⁷

A review of theory of operation of the TE_{01n} dielectrometer was given earlier^{6, 8} and is reproduced in Appendix A for convenience. In essence, the circular-cylindrical cavity is tuned to resonance by means of a non-contacting micrometer plunger which forms the lower end of the cavity. A disc-shaped material specimen of known thickness is placed on top of the plunger and the cavity is retuned. The relative dielectric constant is then obtained from the shift in resonance length and the loss tangent is calculated from the half bandwidths of the resonance peaks, under empty and loaded conditions, respectively.

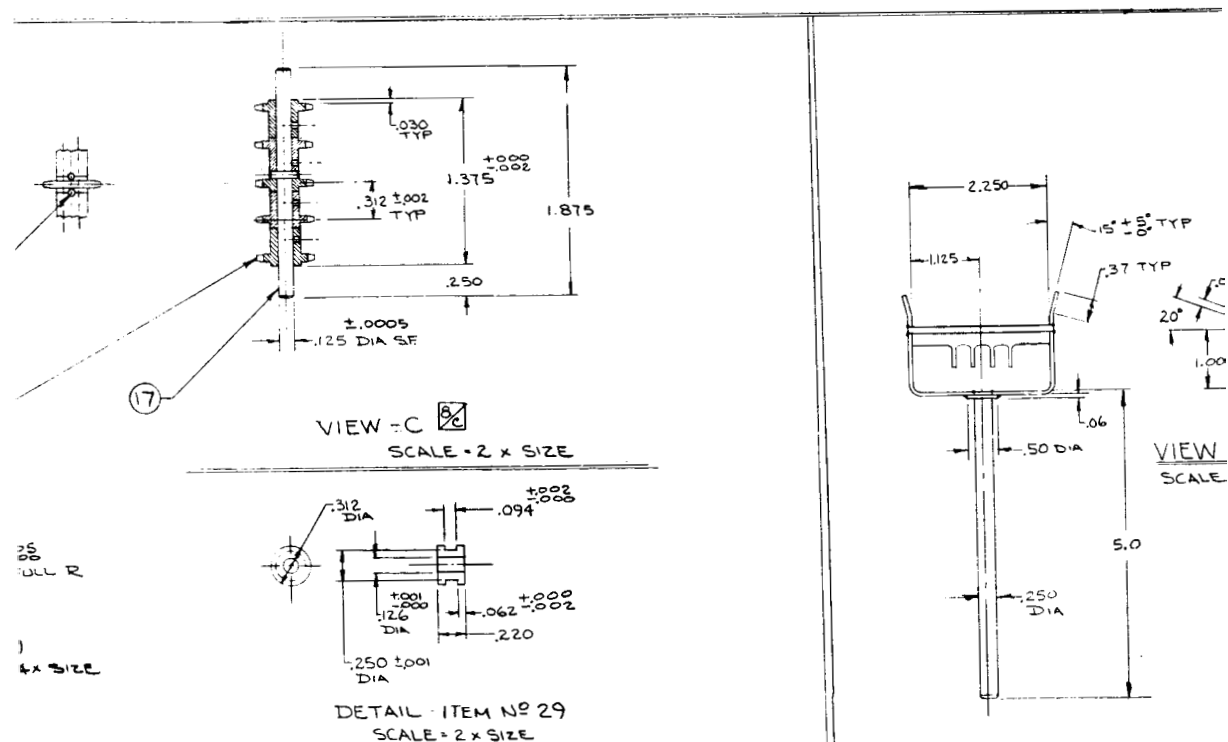
Although the instrument may be operated in air or evacuated, during the study period covered by this report the test specimens were measured in air. To conduct measurements during the course of irradiations, the instrument would be directly coupled to the environmental chamber and operated under vacuum. A proposed system for transferring the specimens between the chamber and the dielectrometer is shown schematically in Figure 6, and in more detail in Figure 23.



02



DETAIL ITEM NO 1

DETAIL ITEM NO 29
SCALE = 2 x SIZE

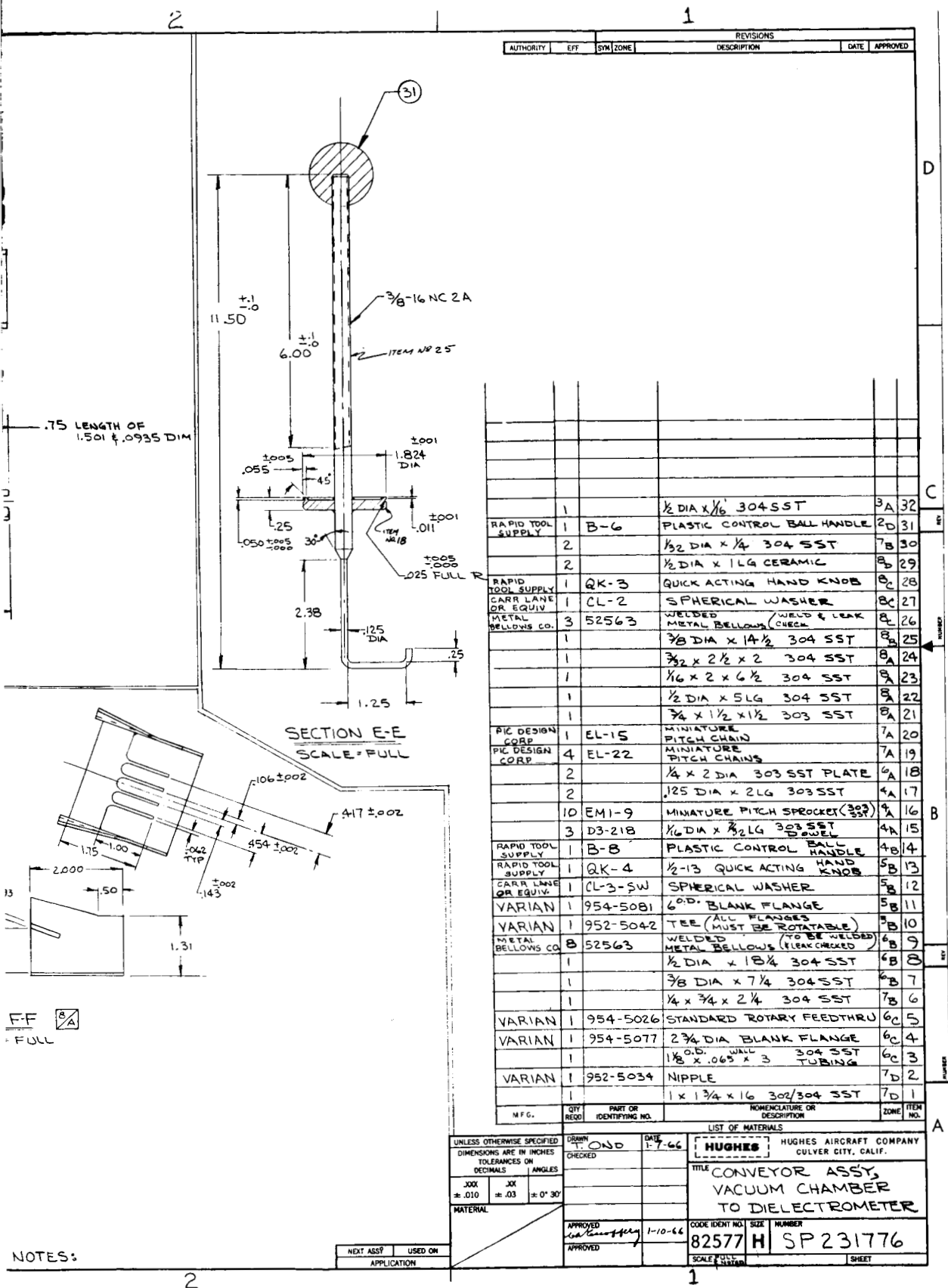


Figure 23. Details of proposed specimen transfer tunnel.

42-3

The circuit used for measuring permittivity with the dielectrometer is shown in Figure 24. A photograph of the dielectrometer assembly and associated electronic components is shown in Figure 25. Here, the instrument was being used in a study of in situ permittivity measurements of specimens in vacuum under ultraviolet irradiation.⁶

Specimens to be measured in the dielectrometer are prepared in the form of flat (within 0.001 inch) discs, 2.135 inches in diameter, and of a thickness, b , approximately half of the wavelength λ_s in the specimen. The specimen wavelength, λ_s , is determined from the expression

$$\lambda_s = \frac{\lambda_o}{\sqrt{\epsilon'_s - \left(\frac{k}{\beta_o}\right)^2}} \quad (4)$$

where λ_o and β_o are the free-space wavelength and phase constant, respectively, ϵ'_s is the specimen's relative dielectric constant, and k is the transverse wave number. These terms are further defined and discussed in Appendix A.

The calculations required to derive the relative dielectric constant and loss are well established.^{9, 10} As shown in Appendix A, the dielectric constant of the specimen relative to that of the dielectric filling the cavity is given by

$$\frac{\epsilon'_s}{\epsilon'_g} = \frac{\beta_s^2 + k^2}{\beta_g^2 + k^2} \left(1 - \frac{\beta_s^2 + k^2}{\beta_s^2} \cdot \frac{\tan^2 \delta}{4} \right) \quad (5)$$

where

β_s = phase constant in the specimen

β_g = phase constant in the cavity (guide) and

$k = x_1/a$,

where x_1 , the least root of the Bessel function $J_1(x)$, equals 3.83171, and a , the cavity radius, is 1.08045 inches for the present dielectrometer.

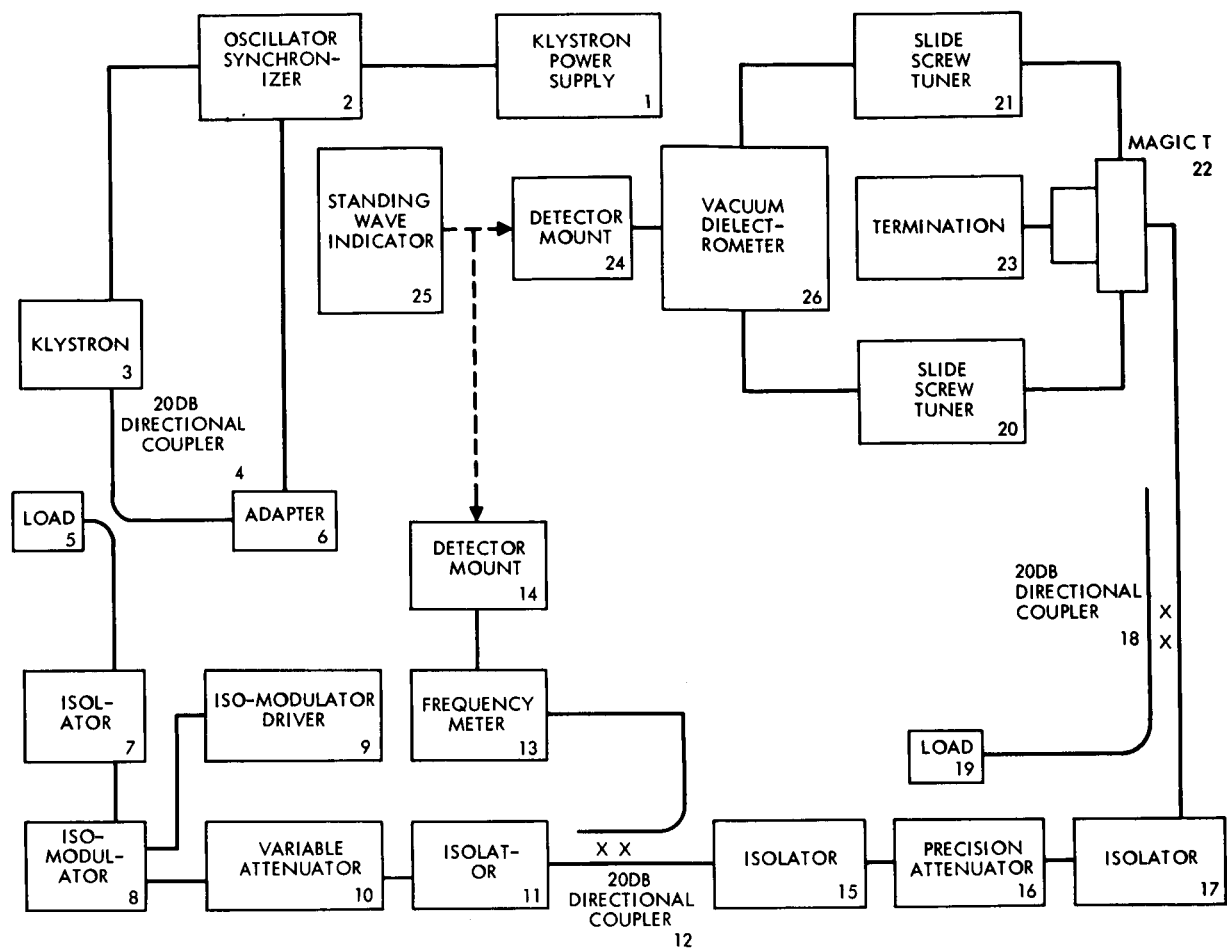


Figure 24. Block diagram for measuring permittivity in microwave dielectric meter.

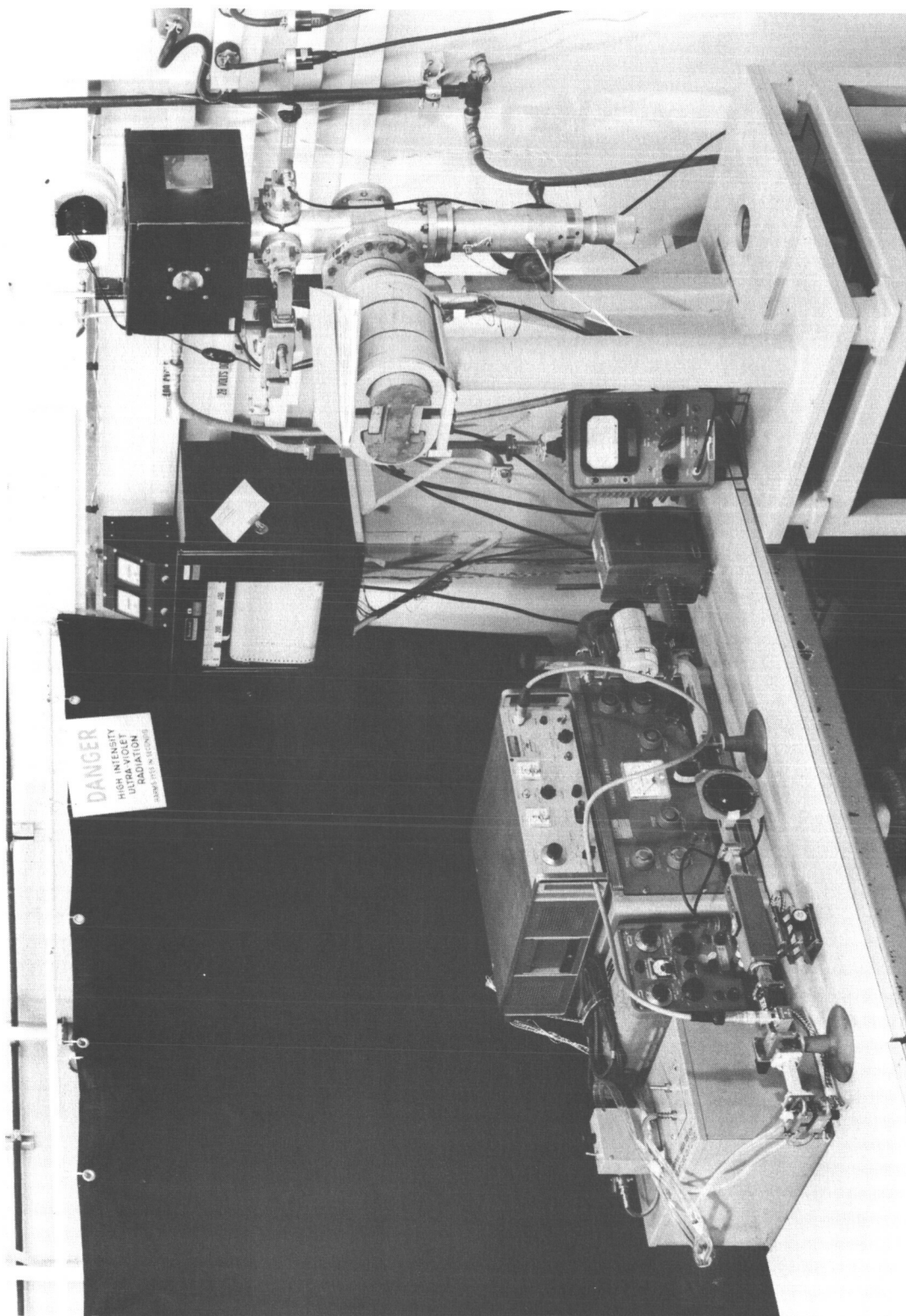


Figure 25. Vacuum microwave dielectrometer assembly
(HAC Photo No. R106546).

The specimen phase-constant, β_g , is obtained by solution of the transcendental equation

$$\frac{\tan \beta_s b}{\beta_s b} = - \frac{\tan \beta_g (\ell - b)}{\beta_g b} = - \frac{\tan \beta_g (X + 2\lambda_g - b)}{\beta_g b} \quad (6)$$

where b is the specimen thickness, ℓ is the TE_{015} resonance length with specimen inserted, $X = \ell - 2\lambda_g = P - TE_{014}$, P is the micrometer reading for the TE_{015} peak with specimen inserted, and TE_{014} is the micrometer reading of the TE_{014} peak in empty cavity.

The cavity phase-constant, β_g , is obtained from the measured guide wavelength, λ_{gs} of the empty cavity by

$$\beta_g = \frac{2\pi}{\lambda_g} = \frac{\pi}{(TE_{015} - TE_{014})} \quad (7)$$

The loss tangent is calculated by the expression

$$\tan \delta = \frac{\beta_g^2}{\beta_o^2 \bar{\epsilon}_s' B^2 b'} \cdot (\Delta\ell - C) \quad (8)$$

where $\bar{\epsilon}_s'$ is obtained from the first term of Equation (5), B is given by

$$B = \left[1 + \left(\frac{\beta_s^2}{\beta_g^2} - 1 \right) \cos^2 \beta_s b \right]^{-\frac{1}{2}} \quad (9)$$

b' is a modified specimen thickness, related to the actual thickness, b , by

$$b' = b \left(1 - \frac{\sin 2\beta_s b}{2\beta_s b} \right) \quad (10)$$

and C is a correction term, generally small with respect to $\Delta\ell$, the half-power bandwidth. The term C is given by

$$C = \frac{d}{a} \left[a \left(1 + \frac{B^2 \beta_s^2}{\beta_g^2} \right) + \frac{k^2}{\beta_g^2} (B^2 b' + \ell') \right] \quad (11)$$

where ℓ' is a modified cavity length given by

$$\ell' = (\ell - b) \left(1 - \frac{\sin 2 \beta_g (\ell - b)}{2 \beta_g (\ell - b)} \right) \quad (12)$$

d is the skin depth of the cavity walls, and a is the cavity radius.

In Equation (8), the quantity d/a cannot be taken from a theoretical calculation, but must be obtained from Q -measurements on the empty cavity, through the expression

$$\frac{d}{a} = \frac{\beta_g^2}{k^2 + 2 \beta_b^2 \left(\frac{a}{L} \right)} \cdot \frac{\Delta L}{L} \quad (13)$$

where ΔL is the half-power bandwidth of the empty cavity, and L is the resonant length.

Figure 26 illustrates a typical resonance curve for the cavity filled with air. When the dielectrometer is evacuated, the bandwidth is somewhat smaller.

From the value of ΔL one can calculate the cavity Q , through the expression

$$\frac{1}{Q} = \frac{\beta_g^2}{\beta_o^2} \cdot \frac{\Delta L}{L} \quad (14)$$

Using this equation for the conditions of Figure 26, a Q value of 23,600 is obtained.

Since the calculations involved in computing the dielectric constant and loss tangent are laborious, they have been programmed for a high speed electronic computer.

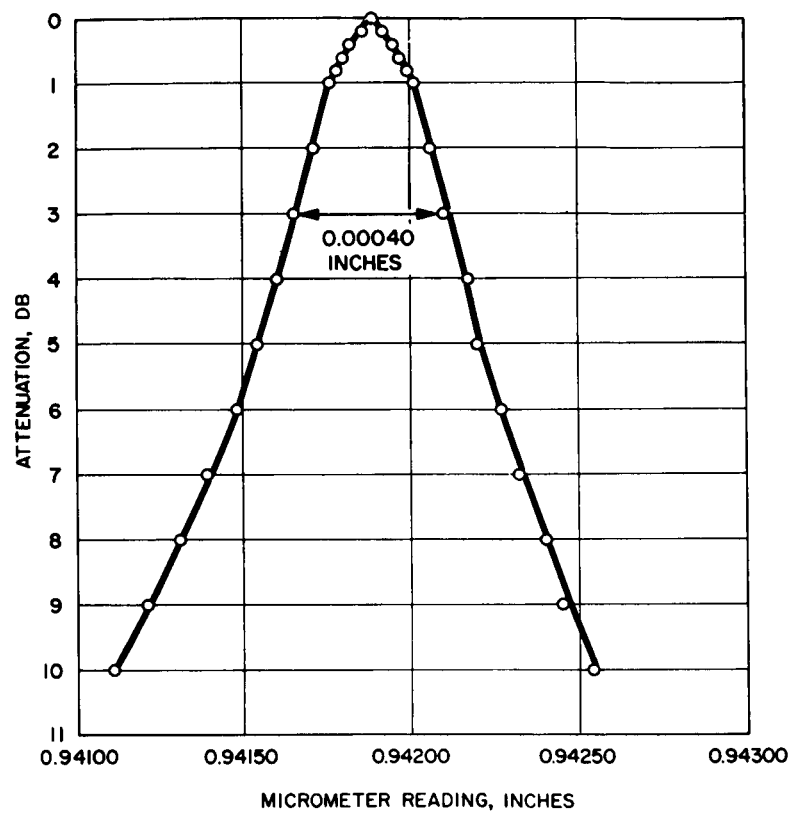


Figure 26. Resonance curve for TE_{015} mode in air-filled cavity.

3.0 DOSIMETRY AND RADIATION CHARACTERIZATION FOR THE ELECTRON BEAM GENERATOR*

3.1 INTRODUCTION

Dosimetry measurements inside the test chamber consisted primarily of variation of absorbed dose rate with electron beam current, planar dose distribution at the sample test position, and electron beam energy. In addition, measurements were made of the relative electron and bremsstrahlung dose at several locations throughout the chamber. The techniques used for the measurements were silver-activated phosphate glass fluorods, lithium fluoride thermoluminescence phosphor, and photographic film. Electron dose measurements were made with unshielded dosimeters while bremsstrahlung measurements were performed under conditions of photon-electron equilibrium.

3.2 DOSIMETRY TECHNIQUES

The silver-activated phosphate glass fluorods are 1 mm in diameter and 6 mm long and are supplied by Bausch and Lomb. Radiation-induced luminescence is measured with a Turner fluorometer. Calibration of the system is accomplished by first exposing a representative group of fluorods in photon-electron equilibrium packages to a known cobalt-60 gamma-ray flux and then calculating the absorbed dose. A typical calibration curve is shown in Figure 27. The useful dose range of this system is 10^2 to 10^4 rads.

The Controls For Radiation Corporation Thermoluminescence Dosimetry System is used by the Dosimetry Laboratory. This system utilizes lithium fluoride as the phosphor which may be packaged in a variety of configurations and amounts. Precise amounts of irradiated phosphor are heated to a prescribed temperature, and an automatic readout of the luminescence is obtained. The system was calibrated

* This section contributed by the Radiation Effects Dosimetry Laboratory, Hughes Aircraft Company, Fullerton, California.

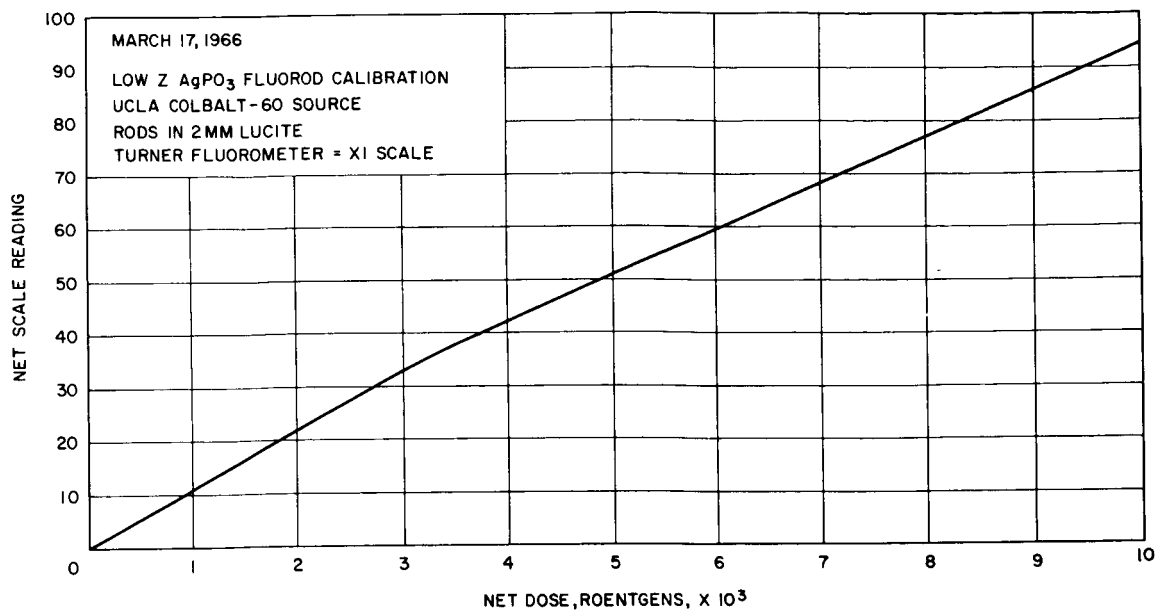


Figure 27. Low Z AgPO_3 fluorod calibration.

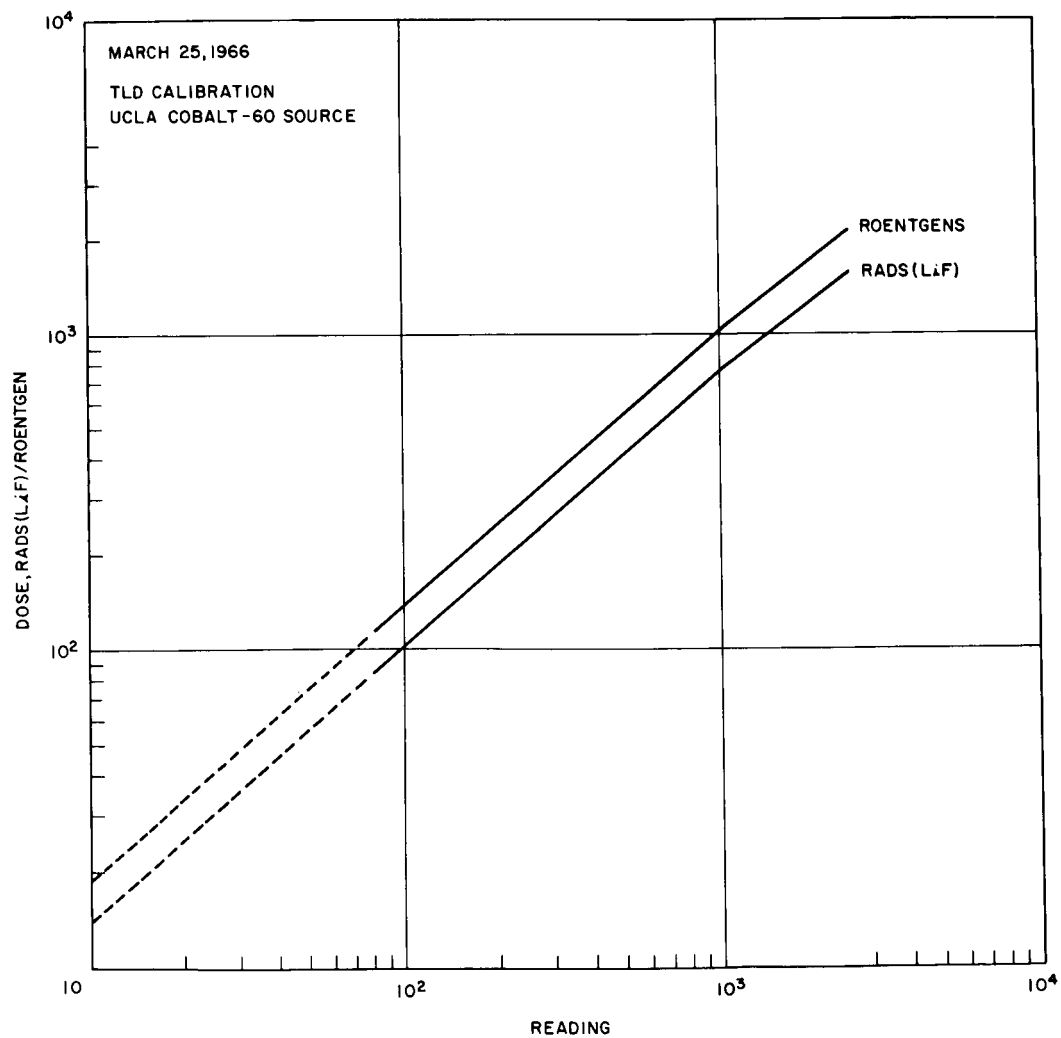


Figure 28. Thermoluminescent dosimeter calibration.

in a manner similar to that for the fluorod system. A typical calibration curve is shown in Figure 28. The dose range of the TLD system is 10 to 10^5 rads.

The photographic film used for these experiments was duPont Type 1290 having a sensitivity range from 10 to 1000 rads depending upon the radiation energy. The relative density of exposed film is measured with a MacBeth-Ansco Densitometer. This system is also calibrated with a standard cobalt-60 gamma-ray flux. The dose ranges selected for film exposures provided a relative sensitivity of about ± 10 percent.

3.3 MEASUREMENTS

The test chamber is designed for irradiation of one sample at a time. In order to ensure that samples within the chamber other than the test sample do not receive a significant dose during irradiation periods, adequate shielding and collimation must be provided. This was accomplished by passing the electron beam through a 2-inch hole bored in a 1/8-inch aluminum plate at the generator window outside the chamber and then through an aluminum collimating tube inside the chamber extending from the chamber window to the sample stand.

Dose rates were measured at the center of the sample test position for several different values of electron beam current using the thermoluminescence dosimeters (TLD). The aluminum plate was used as the beam monitor. The TLD phosphor was packaged in thin polyethylene envelopes. A plot of the results is shown in Figure 29.

The planar dose distribution at the test sample position was measured with unshielded glass fluorods and photographic film. Initial measurements indicated a slight misalignment of the sample position with respect to the collimated beam. When this was corrected, additional measurements revealed a uniform dose distribution within ± 10 percent over the test sample area. It was also found that beam alignment could be accomplished quickly and easily by exposing glass discs.

An estimate of the electron energy spectrum was made from measurements with TLD phosphor and varying thicknesses of aluminum

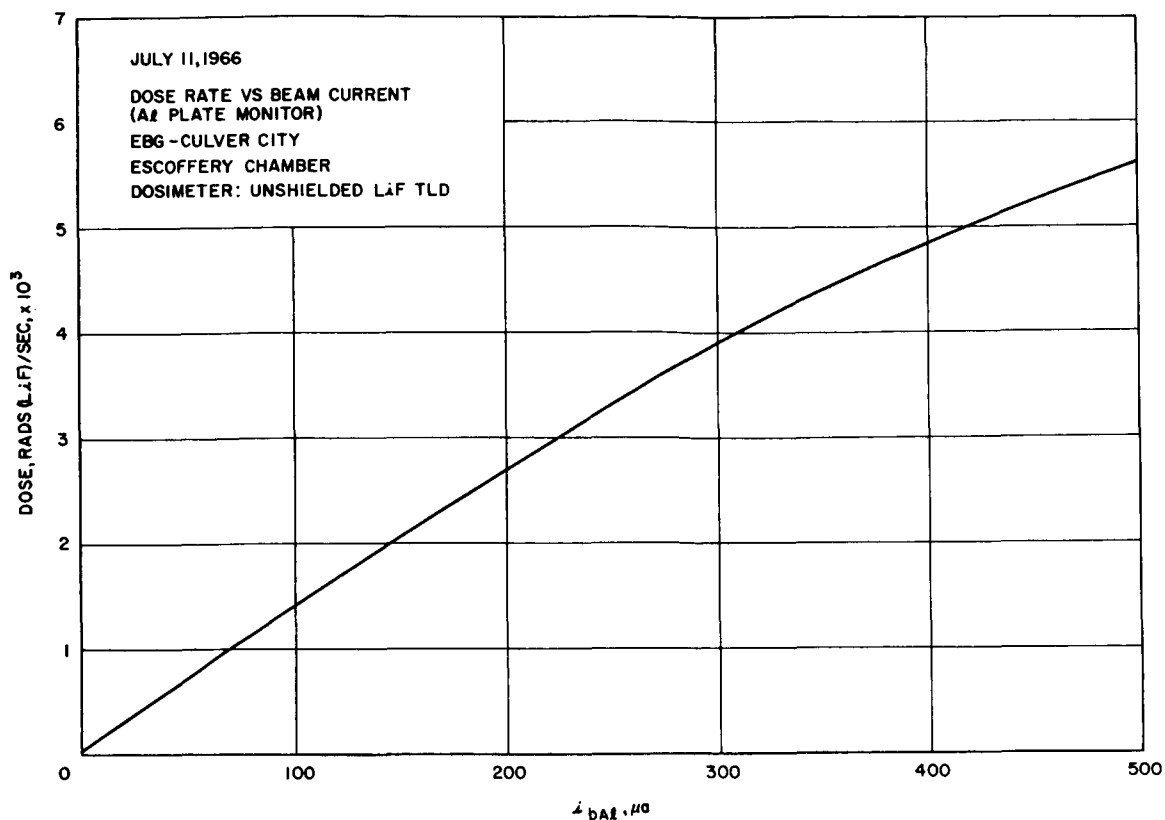


Figure 29. Dose rate versus beam current (A1 plate monitor).

absorbers at a constant total dose. Calculations of the energy spectrum were made from electron range-energy relationships. The results of the calculations are presented in Table 1. The minimum penetrating energy was calculated assuming a maximum range equal to the absorber thickness. The fraction of electrons with energies less than the minimum penetrating energy was determined from the ratio of the response of an unshielded dosimeter to the various responses of the shielded dosimeters. Since the maximum machine energy is 1 Mev, this ratio was assumed to be 1.0 at that energy. In addition to the aforementioned measurements, the ratio of bremsstrahlung dose to electron dose was determined, and an evaluation of the relative accumulated chamber background was performed. The dose ratio was measured at several locations in the chamber with both film and TLD by observing the relative response with and without a 430 mg/cm^2 aluminum absorber. This ratio did not exceed 0.01 with either dosimeter type.

Absorber Thickness (mg/cm ²)	Minimum Penetrating Electron Energy (Mev)	Fraction of Electrons With Energies Less Than Minimum Penetrating Energy
430	1.0	1.00
70	0.3	0.55
50	0.2	0.35
20	0.1	0.10

Table 1. Calculations of electron energy spectrum.

Chamber background measurements were performed with unshielded packages of TLD phosphor placed at several sample locations throughout the chamber. The purpose of these measurements was to determine the dose accumulated by samples not in the direct electron beam during irradiations. Table 2 gives the dose relative to the direct beam for the locations examined. The direct beam was located in sample position 0 during these measurements.

Sample Position	Relative Dose
1	0.002
2	0.001
3	0.001
6	0.00004
12	0.00001
18	0.00003
22	0.001
23	0.002
24	0.003

Table 2. Chamber background dose measurements.

For a plan view of the specimen position layout on the turntable, see Figure 47 in Section 4.5.

4.0 EXPERIMENTAL RESULTS

4.1 STUDIES ON THE MEASUREMENT OF OPTICAL PROPERTIES

To measure solar absorptance of, for instance, thermal control coatings, use is made of the integrating sphere described in Section 2.3. The measurement requires the determination of spectral reflectance over the spectral region of 0.29-2.6 microns and numerical integration. That is, since the coating is opaque:

$$\alpha_{\lambda} = 1 - \rho_{\lambda} \quad (15)$$

where α_{λ} and ρ_{λ} denote the spectral absorptance and spectral reflectance, respectively. Then the value of solar absorptance, α_s , is given by

$$\alpha_s = 1 - \sum \rho_{\lambda} \Delta\lambda \quad (16)$$

The reflectance of the specimen at each spectral point is normalized with respect to the total reflectance of the instrument.

Preliminary studies were directed to developing suitable techniques for optimizing signal strength and detector sensitivity. Readout of signals depends upon proper conversion, sufficient amplification of the signal, and proper differentiation of the signal from noise.

Differentiation between signal and noise is important because the light sources and detectors are inherently noisy (due to a number of reasons),¹¹ and because signal strength in certain regions of the spectrum (notably in the UV) is quite low approaching the noise level. Figure 30 shows the UV output of three light sources.¹² Various light sources were tried and best results were obtained with a 150-watt xenon-arc lamp.

To improve matters, the light beam is chopped (13 cps), and a tuned preamplifier-amplifier and tuned bandpass filter were employed. The system used is the result of extensive testing. As a final test, the system was compared to a Perkin-Elmer Model 107 amplifier and

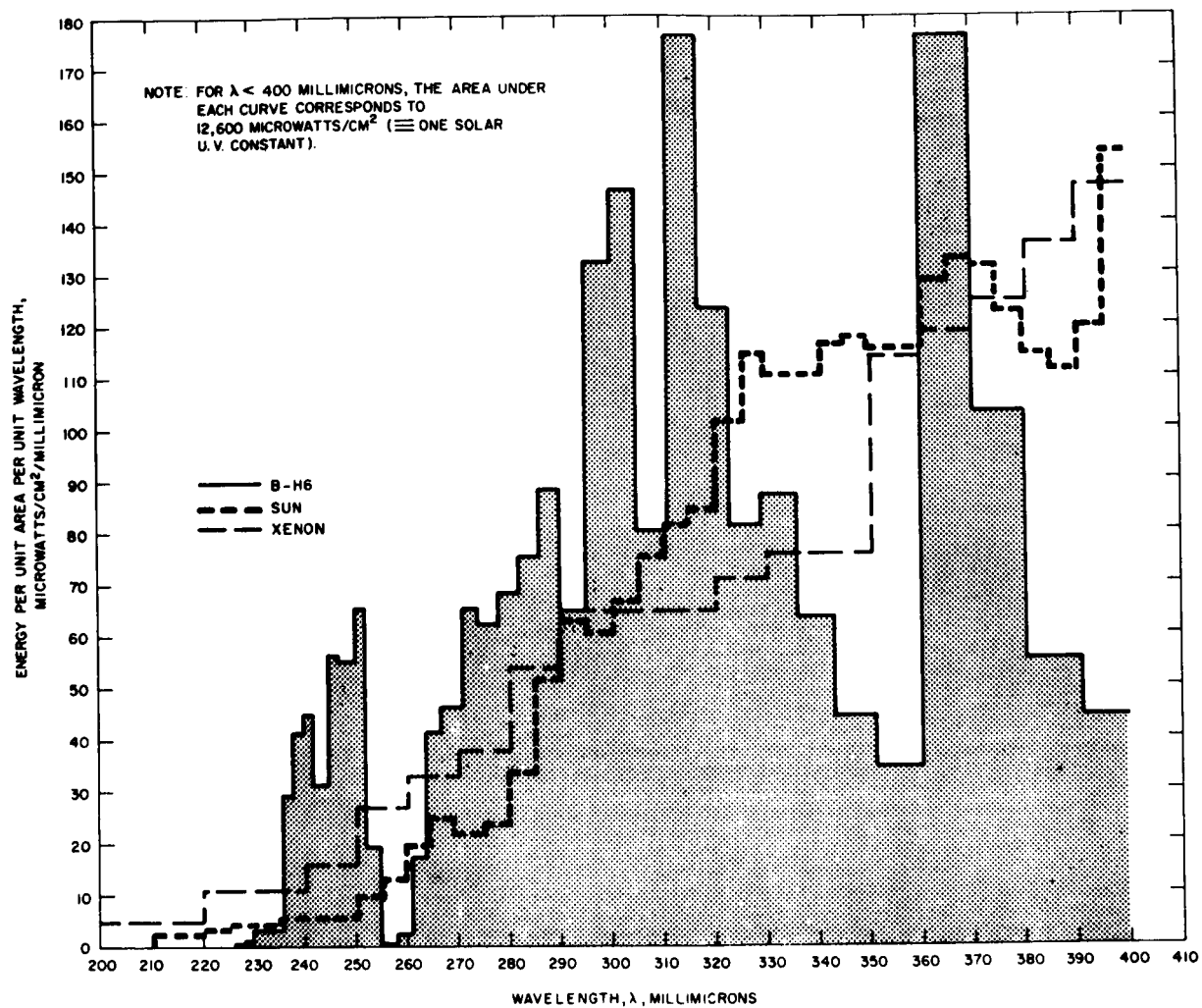


Figure 30. Comparison of the UV output of three sources.¹²

the readout system used on a Perkin-Elmer monochromator. The results are shown below:

	Perkin-Elmer	Hughes Aircraft
Amplification	10^9	10^{12}
Accurate readout ^(a)	10^{-8} volts	10^{-11} volts
Noise level ^(b)	0.02 μ volts	10 μ volts
<p>(a) This portion of the test was unfair to the PE system since a strip chart recorder was used in the PE read-out while the Hughes system used an integrating digital voltmeter.</p> <p>(b) This comparison was at 3 microns wavelength, and again note (a) applies.</p>		

Undoubtedly, the Hughes system was favored by the use of an integrating digital voltmeter* which eliminated a great portion of the noise. While both systems became saturated at maximum sensitivity, the Hughes system also saturated at minimum sensitivity and additional attenuation was required.

Readout on our Hughes system may be accomplished by an oscilloscope, strip chart recorder, or digital voltmeter. The latter has numerous advantages, such as noise reduction, capability for further readout, and the ability to read out in computer language. Figure 31 depicts the signal flow from the light source to the final readout with provisions for direct computer calculations.

Electronic and mechanical modulation of the xenon light source was compared. It was found that:

1. Electronic modulation gave more constant frequency.
2. Electronic modulation could be tuned to the detector's best frequency response.
3. Electronic modulation created an r-f signal to which the detector responded.

*Model 5200, manufactured by Hughes Aircraft Company, Vacuum Tube Products Division, Oceanside, California.

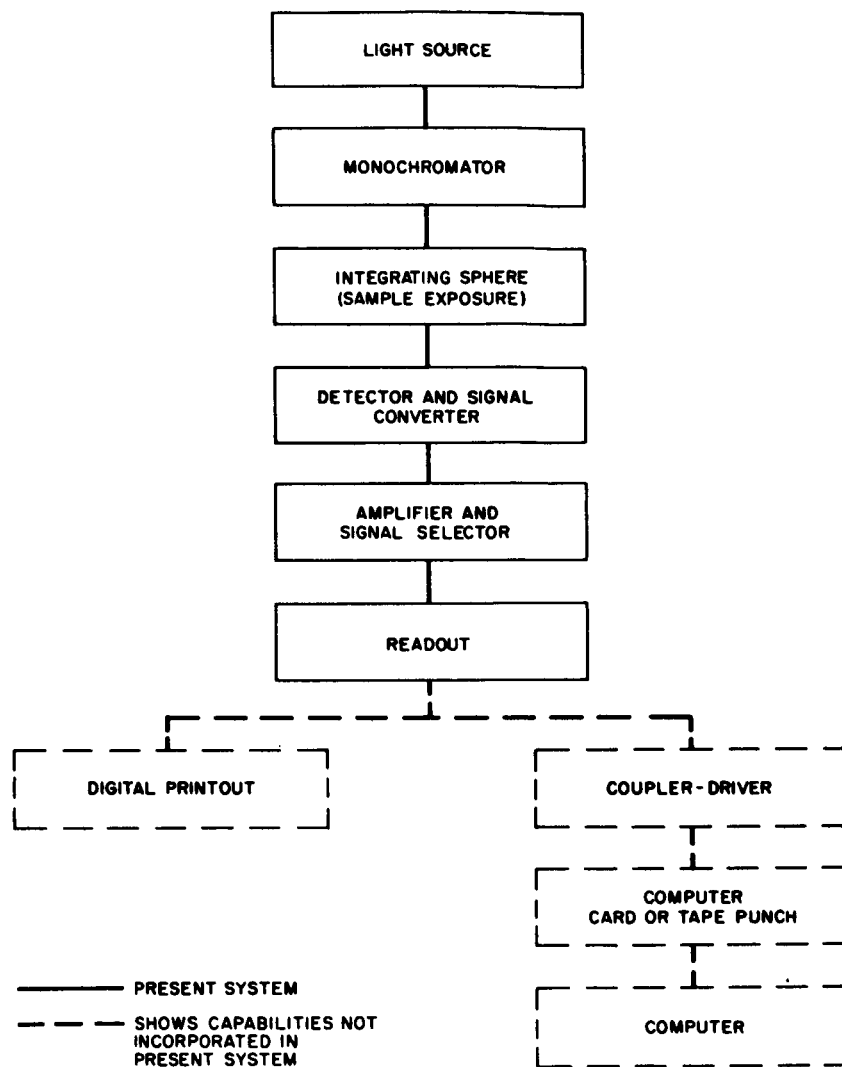


Figure 31. Signal flow-chart, optical measurements.

4. The r-f signals could not be differentiated from the optical signals at certain wavelengths, noticeably in the ultraviolet. It was decided that mechanical modulation was preferable to electronic modulation.

It had been hoped to use a (Reeder Co.) thermopile as a flat-response detector throughout the entire spectral range of interest but this proved unsuccessful. Our studies indicated that the integrating sphere reduces the signal by a factor of 1000 or more, in agreement with work done elsewhere.¹³ This large energy loss, coupled with the thermopile's inherently low value of detectivity,¹¹ indicated that a thermopile detector was not practical.

Other detectors were then investigated. As shown in Figure 32, the detectivity of Si detectors and photomultiplier tubes is about 10^{11} to 10^{12} cm cps^{1/2} W⁻¹, and that of PbS about 10^{10} to 10^{11} cm cps^{1/2} W⁻¹. The detectivity of a thermopile¹¹ is only of the order of 10^9 cm cps^{1/2} W⁻¹.

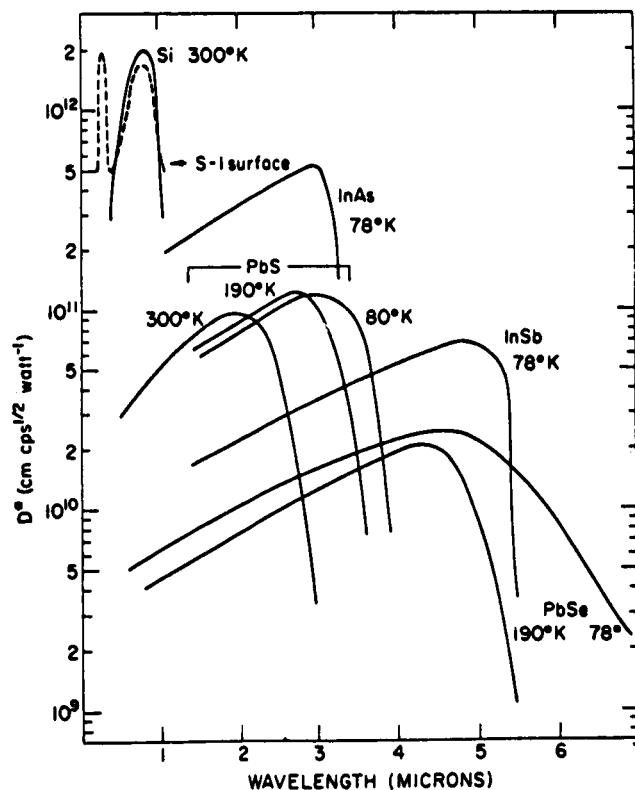


Figure 32. Detectivity of typical detectors.¹¹

Phototubes have a smaller signal-to-noise ratio than photoconductive or photovoltaic cells. A small silicon p-n photodiode, said to be suitable between 300 - 10,000 Angstroms, was satisfactorily tested in the laboratory with a 150-watt xenon light source over the range 2000 - 10,000 Å in the photovoltaic mode. To cover the desired spectral range (0.29 - 2.6), it would be desirable to develop a dual solid-state detector (e. g., Si and PbS) mounted on the same base, with electronic switching performed outside the vacuum chamber at the amplifier-readout station.

A single-beam quartz prism Leiss monochromator was used in initial studies. Later, when a Leiss double-prism monochromator became available it was calibrated and readied for use. Calibration was performed with EG&G model 580/585 grating spectro radiometers with a resolution of 0.01 micron. The signal from the Leiss instrument was passed via the EG&G spectrometer into the detector at 50 mμ intervals. The results are shown in Figures 33 and 34.

Time was not available to install the optical integrating sphere in the vacuum chamber and conduct solar absorptance measurements, but we were able to check out the instrument in air using a PbS detector. The interior surfaces of the sphere were smoked with magnesium oxide, and monochromatic light was obtained from a tungsten filament and a Perkin-Elmer model 98 monochromator.

The spectral reflectance of two thermal control coatings was measured and compared with the values previously obtained on a standard Gier-Dunkle integrating sphere. The results are shown in Figure 35. Agreement is quite good and within experimental error.

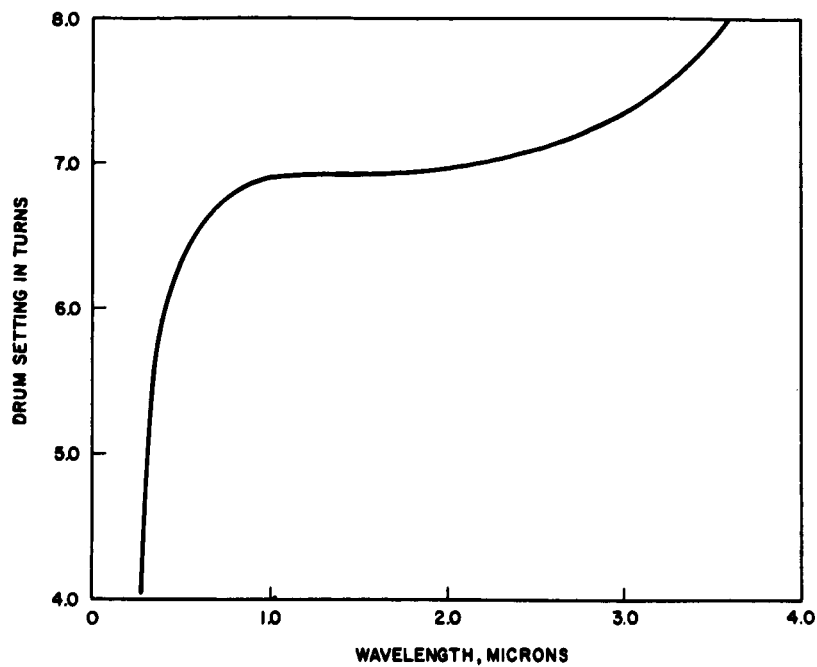


Figure 33. Monochromator calibration curve (0.3 - 3.5 μ).

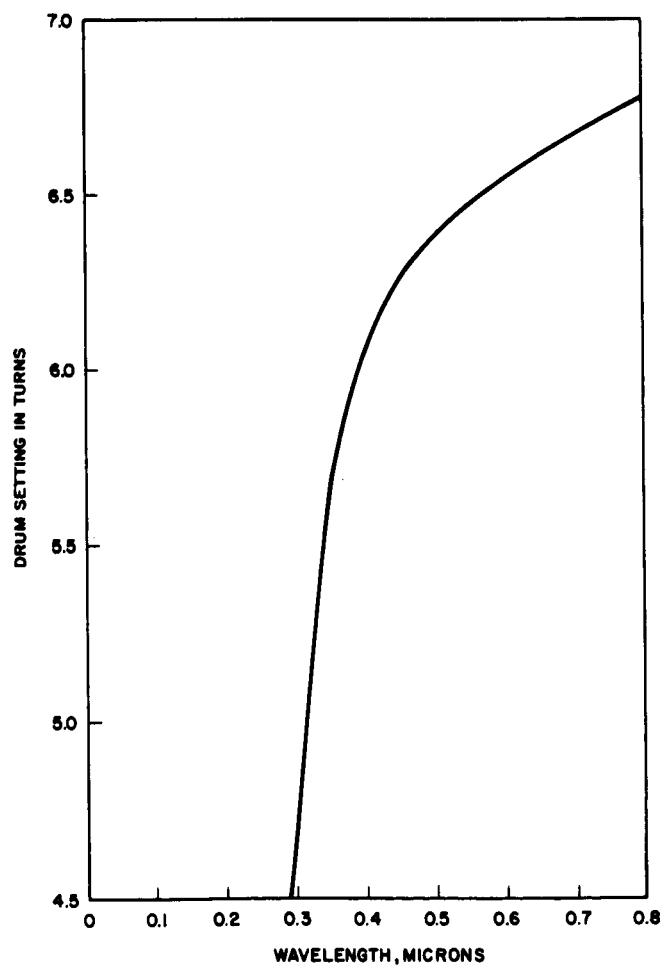


Figure 34. Monochromator calibration curve (0.3 - 0.8 μ).

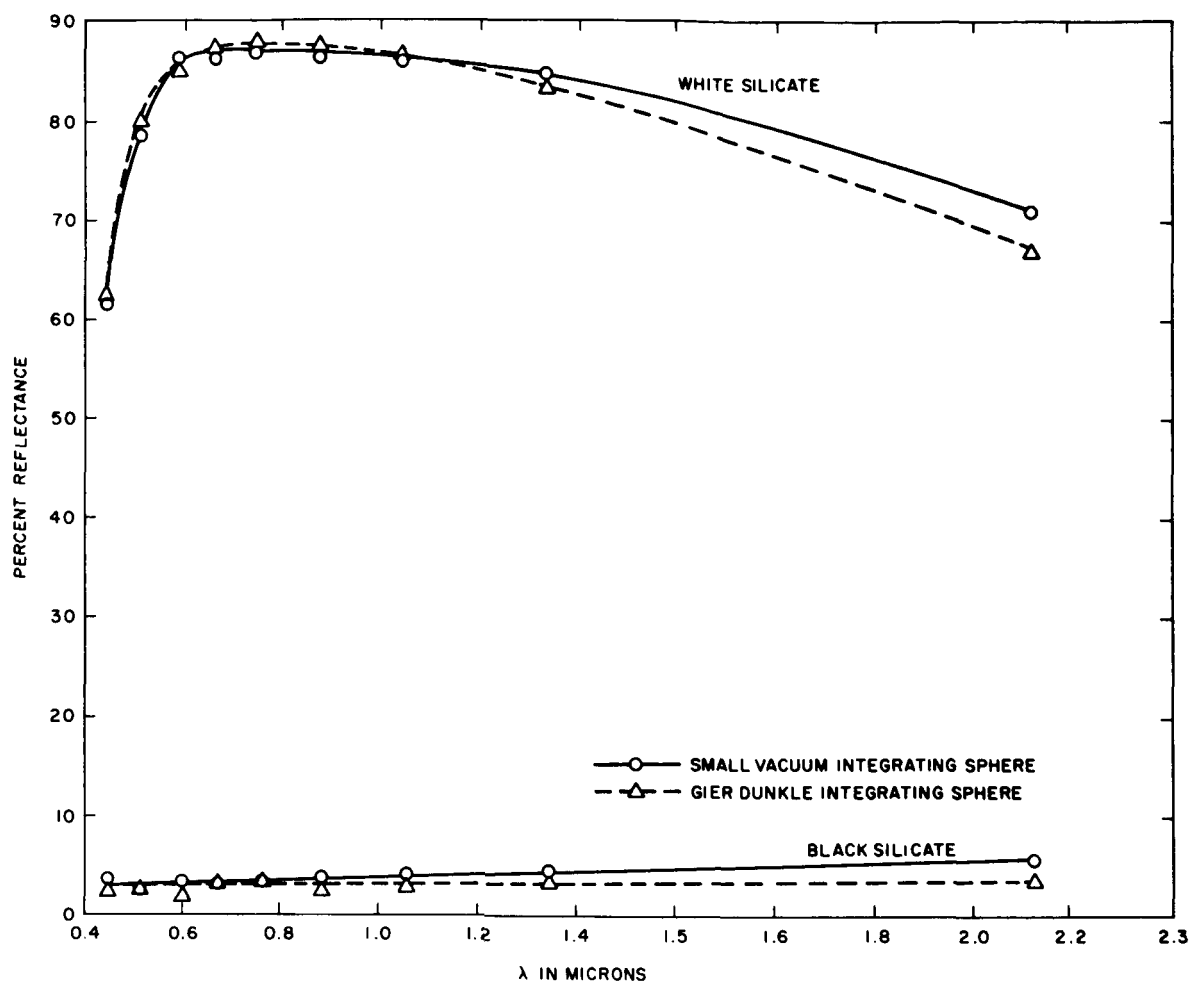


Figure 35. Comparison (in air) of small vacuum integrating sphere with Gier-Dunkle integrating sphere.

4.2 STUDIES ON THE MEASUREMENT OF THERMAL PROPERTIES*

The conventional methods of measuring thermal diffusivity and thermal conductivity are slow and laborious. When these methods are adapted to measurements in vacuum, construction problems are multiplied many times.

Parker et al² have adapted the thermal pulse method of Angstrom to pulses shorter than obtained by Hirschman, Derksen and Monahan.¹⁴ The thermal pulse was obtained from a xenon flash lamp. Later obtained extensions employ a laser.¹⁵ Penneman¹⁶ has used the thermal pulse from a solar furnace and Jenkins¹⁷ has used the pulse technique for measurements in the presence of 2 Mev electrons. Cunningham et al¹⁸ have used a laser to determine thermal diffusivity of graphites and chars.

The method depends upon measuring the temperature rise of the back surface of a sample due to the passage of the thermal pulse through the sample. If the thermal pulse input time is short compared to the time for passage through the sample, the specimen may be treated mathematically as an infinite slab. A large advantage of the technique is that the heat input need not be known for thermal diffusivity measurements. Parker et al² calculated two dimensionless parameters from the treatment of Carslaw and Jaeger. These parameters are:

$$V(L, t) = \frac{T(L, t)}{T_m} \quad (17)$$

and

$$W = \frac{\pi^2 \alpha t}{L^2} \quad (18)$$

where

α is the thermal diffusivity,

L is the thickness of the specimen,

*This section contributed by G. R. Blair.

t is the time,

T is the front surface temperature, and

T_m is the back surface temperature.

The authors plotted V versus W and suggested two ways to determine α :

1. At half maximum temperature rise $V = 0.5$, $W = 1.37$ and hence

$$\alpha = \frac{1.37 L^2}{\pi^2 t_{1/2}} \quad (19)$$

where $t_{1/2}$ is the time taken to reach half maximum temperature.

2. t_x , the extrapolated intercept on the time axis at zero temperature rise, occurs at $W = 0.48$, and therefore

$$\alpha = \frac{0.48 L^2}{\pi^2 t_x} \quad (20)$$

Once T_m has been measured, the thermal conductivity may be obtained from the following equation

$$DC = \frac{Q}{LT_m} \quad (21)$$

and

$$K = \alpha DC \quad (22)$$

where

D = density

C = heat capacity

Q = energy absorbed at front surface
 K = thermal conductivity, and
 α = thermal diffusivity

The curve of V versus W is obtained experimentally from the oscilloscope trace of the temperature history of the backface of the sample.

The technique may be adapted to vacuum systems with minimum effort. The transmission of the energy may be carried out through a suitable window in the chamber wall.

The major problem with this technique is in the amplifier. In exploratory studies, many different amplifiers were tried but the combination of a Tektronix RM 122 preamplifier and a Tektronix 53/54E low-level differential amplifier gave best results. The specimen was encased in a copper housing to eliminate pickup from the flash tube discharge. Shielding of all wires is also most important to remove specimen signal from the flash lamp discharge.

Subsequently, the noise problem was solved by building a special differential amplifier using semiconductors and battery power. The unit was enclosed in a metal box to remove specimen pickup. The amplifier has a (maximum) amplification of 100 and noise in the 4 to 8 microvolt region.

Using a GE FT-320 flash lamp no thermal pulse could be detected on the backface of the target. The use of Sylvania Blue Dot photoflash bulbs generated a sufficiently sharp rise time so that excellent traces of the thermal diffusivity could be obtained.

Because the photoflash bulb has a long pulse duration, when the photoflash bulb is used as the pulse source, the t_x in Equation (17), is used rather than the time to half maximum temperature rise of Equation (16). This method is favored by Taylor.¹⁹

Figure 36 shows the trace obtained on 0.062 aluminum (6061) using the photoflash bulb. The shape of the curve is identical with the theoretical curve. Each time unit is 5 milliseconds. Figure 37 is a trace of light output versus time for the Sylvania Blue Dot bulb. Each

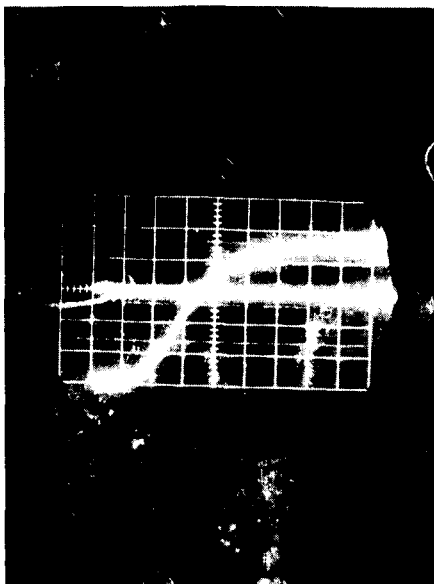


Figure 36. Rear face temperature rise of 0.062" aluminum (time on horizontal axis, 1 cm = 10 milliseconds).

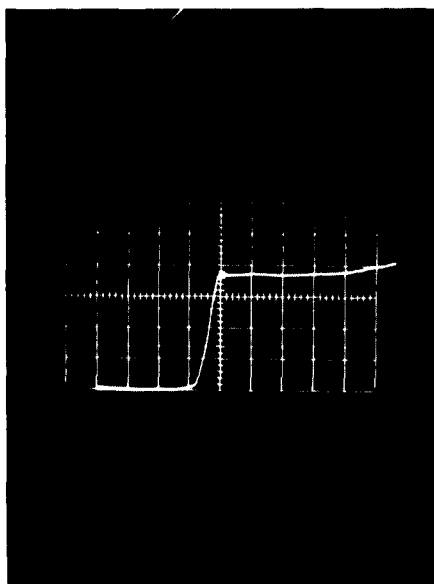


Figure 37. Time trace of Sylvania Blue Dot photoflash bulb (time on horizontal axis, 1 cm = 1 millisecond).

(Polaroid photos)

time unit is one millisecond. The sharp rise time is quite adequate for the purposes of this test.

The use of the flash bulb enables the geometry of source and target to be altered a little more than if a xenon flash bulb were used. Incorporation of an ellipsoidal mirror of proper focal length will enable the source to be placed outside the vacuum chamber, at a reasonable distance from the target.

Using the photoflash bulb technique, some thermal diffusivity measurements were made in air. Target specimens included stainless steel, aluminum, fiberglass laminate, copper, brass, and alumina. Values of thermal diffusivity for stainless steel and for alumina have been calculated from the measured data. These values (in units of cm^2/sec) are shown below and compared to known values. The agreement is quite good.

	<u>Experimental</u>	<u>Literature</u>
Stainless Steel	0.0352	0.0341
Alumina	0.0966	0.96

These values were obtained on specimens with soot-blackened front surfaces 1 inch away from the Blue Dot photoflash bulb. Although the diffusivity value for brass has not yet been calculated, the heat transfer rate through the brass specimen is less than through aluminum, as it should be.

Some tests have been conducted with the heat source at varying distances from the specimen. The specimen temperature follows the $1/r^2$ law quite well. It is rather obvious that a reflector and lens will be required to place sufficient energy at the specimen surface nearly 6 inches or more away.

A few tests were conducted with a Pyrex window between the flash bulb and specimen. These, at the moment, show that the Pyrex window may be used. An anomaly — based on two tests — is that the temperature rise is higher with the window between the flash bulb and specimen. This has not been resolved at this time.

The thermal pulse has also been applied to a 1/2 inch thick stainless steel specimen. It required 1.1 seconds for the pulse to be transmitted and detected on the rear face.

The temperature measurement in all these tests were made with thermocouples attached to the specimens. A more convenient thermal transducer is required, however, before the pulse-technique can be successfully used in the environmental chamber. A sensitive IR detector in close proximity to the specimen rear surface may be a possible solution.

4.3 STUDIES ON THE MEASUREMENT OF DC RESISTIVITY

Figures 38 and 39 are photographs of a breadboard set-up that was used in preliminary exploratory measurements of dc resistivity. As discussed in Section 2.5, the specimens do not have permanent electrodes. Contact is made by pressing smooth copper electrodes on the two opposite faces. The electrical circuit used is shown in Figure 21 (Section 2.5).

A number of resistivity tests were run giving consistent results for the same material. The results compare favorably with published values. We illustrate below values obtained on three specimens:

<u>Material</u>	<u>Volume Resistivity, Ω-cm</u>		
	<u>Measured</u>	<u>Published</u>	<u>(Ref)</u>
H-film (Kapton)	$>10^{18}$	$>10^{18}$	(20)
Polyethylene film	$>10^{18}$	1×10^{18}	(21)
FEP film	$>10^{18}$	$>10^{18}$	(22)

Upon completion of the resistivity station described in Section 2.5, measurements were made on a number of dielectric specimens prior to testing the specimens designated for electron irradiations. The resistivity, ρ , is calculated by the usual formula:

$$\rho = \frac{RA}{t} = \frac{VA}{It} \quad (23)$$

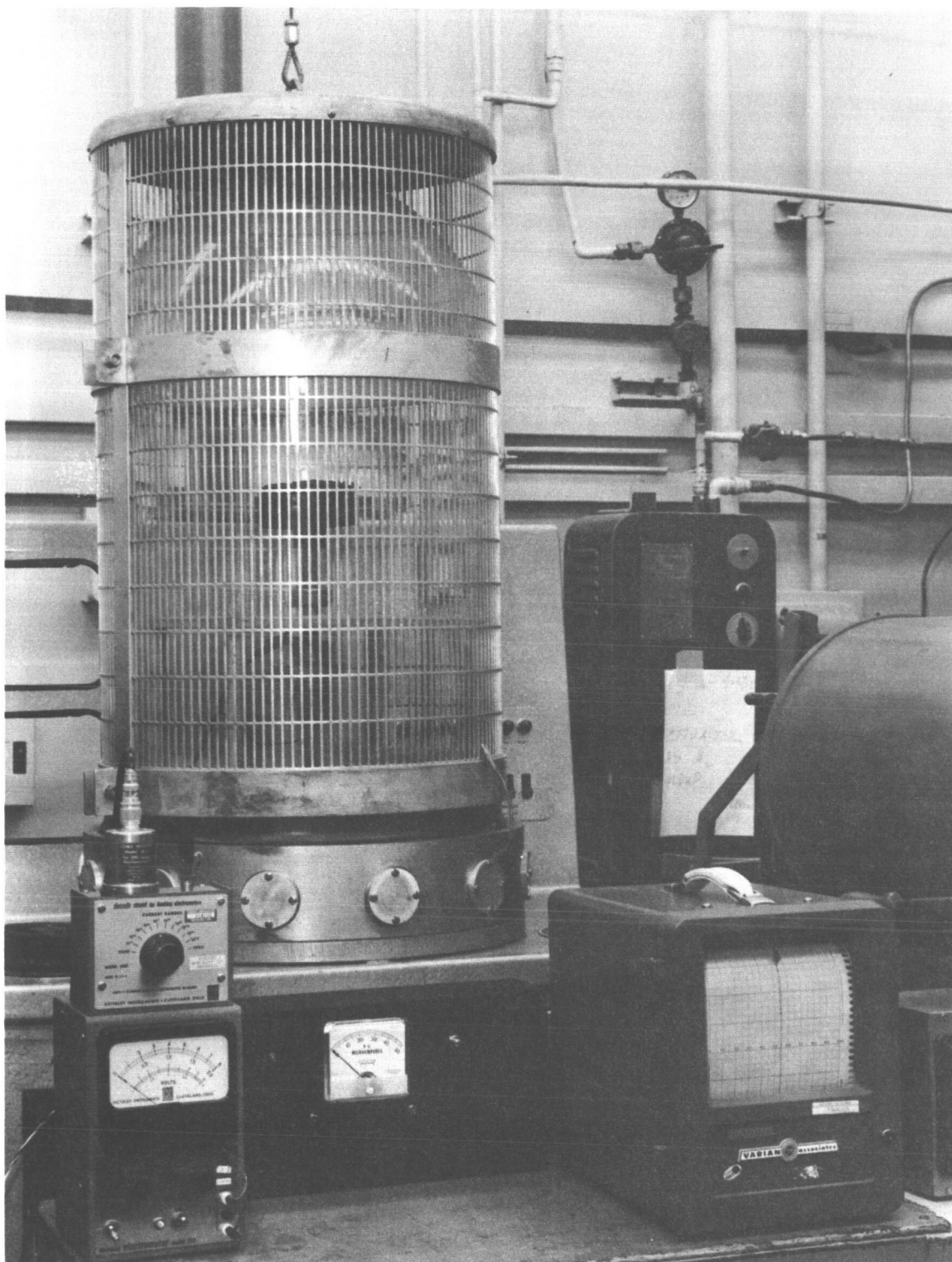


Figure 38. Breadboard set-up for preliminary dc resistivity measurements. (The microammeter in the center has been converted to a two-scale voltmeter, 0-500 and 0-1500 volts.) (HAC Photo No. R106158).

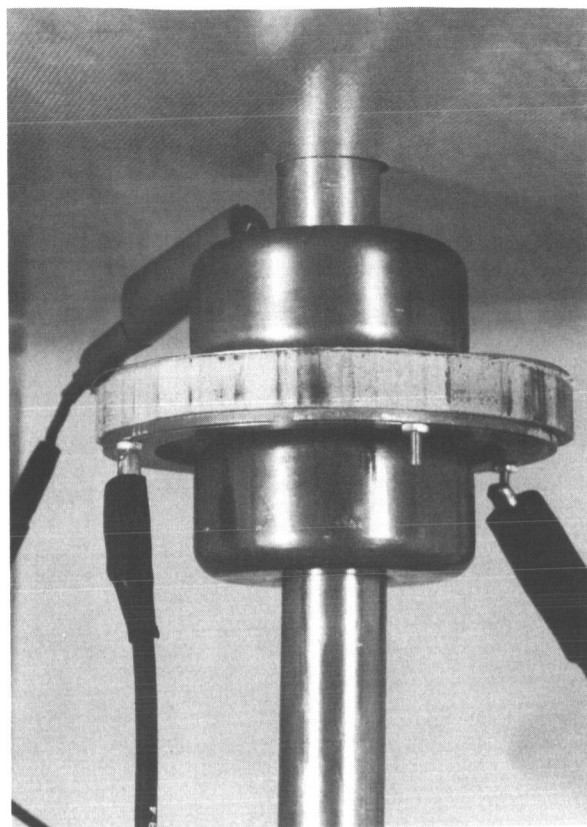


Figure 39. Electrode configuration for preliminary dc resistivity measurements (HAC Photo No. R106159).

where R is the resistance, A the electrode area, t the specimen thickness, V the applied voltage, and I the current. For our set-up, A equals 10 cm^2 and V was 1000 volts dc.

The specimens tested in Run No. 1 (Section 4.5) were of two different thicknesses, respectively. For the 0.310-inch thickness, the resistivity calculation at 1000 volts reduces to

$$\rho = \frac{1.270}{I} \times 10^4 \text{ ohm-cm} \quad (24)$$

and for the 0.280-inch thickness, it becomes

$$\rho = \frac{1.406}{I} \times 10^4 \text{ ohm-cm} \quad (25)$$

The minimum current we could realistically read is about 8×10^{-15} . This corresponds to a maximum detectable resistivity of slightly over 10^{18} ohm-cm.

4.4 STUDIES ON THE MEASUREMENT OF MICROWAVE PERMITTIVITY

A. Effect of Specimen Diameter

The principles for measuring permittivity in the resonant cavity dielectrometer were outlined in Section 2.6. Early in our program it was desired to determine experimentally if a specimen diameter smaller than the customary 2.135 inches could be profitably employed in the 2.160-inch diameter cavity without loss of measurement accuracy.

As previously mentioned, a flat, parallel-faced specimen is placed on top of the tuning plunger which forms one of the cavity end plates. The specimen is made slightly smaller in diameter than the cavity and a clearance exists between specimen and cavity wall. Most workers have indicated that the error due to the presence of this gap is negligible.* This is attributed to the lack of appreciable peripheral electric field in the TE_{01n} mode and to the absence of radial currents in the cavity end plates (see Figure A-3 in Appendix A).

For our tests, we used a laminated disc of polybenzimidazole (PB1) and E-glass, of thickness 0.2991 inch (approximately $\lambda_g/2$) and of initial diameter 2.135 inches. The faces were machined parallel and plane to within 0.001 inch. Measurements were made in air at a fixed frequency of 9.28 GHz as the specimen was progressively reduced in diameter.

As shown in Figure 40, two specimen placements were investigated: (C), with the specimen centered on the plunger, and (S), with the specimen touching the side wall. In each case, after a measurement, the

*Hotson⁽²³⁾, for instance, reported on dielectric-constant measurements made at 9.60 GHz in a 1.886-inch diameter cavity using polystyrene discs ($\epsilon = 2.56$) of varying diameter. His results indicate no noticeable effect up to a 0.093-inch gap, possibly because they are reported to only 3 significant figures.

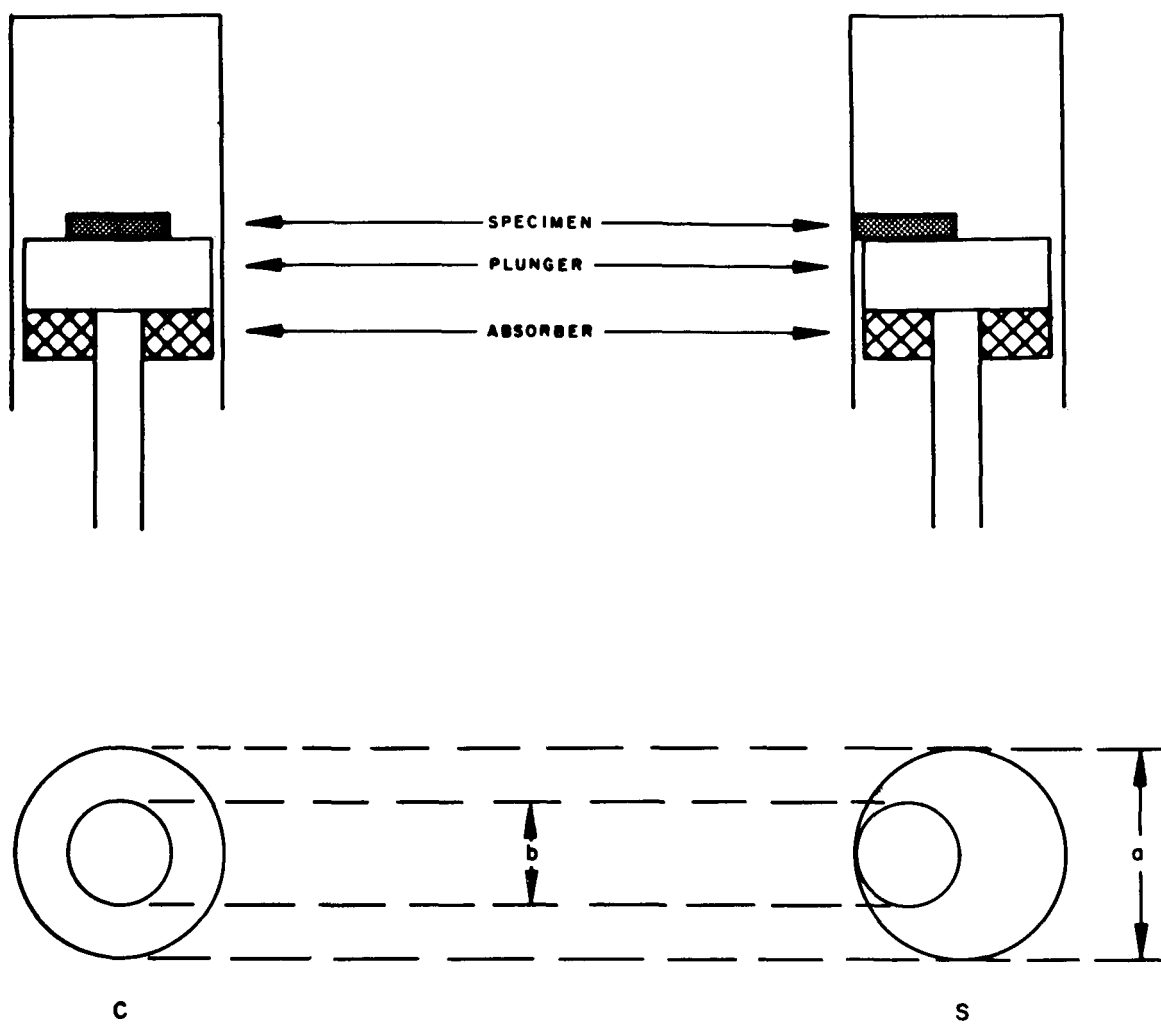


Figure 40. Specimen placement modes.

specimen was inverted and the measurement repeated. Average values of dielectric constant and loss tangent were used in plotting.

The results, shown in Table 3 and Figure 41, indicate that it is not advisable to reduce the specimen diameter from the presently used value. At a 2-inch diameter, values of dielectric constant were 0.2 percent lower, and loss tangent 2.0 percent higher than originally, and the discrepancy increased exponentially with further reduction in specimen diameter.

Our results are similar to but cover a much broader range than those presented by Zal'tsman and Poyarkova.²⁴ These authors made dielectric constant measurements over a 0-0.4 percent diameter decrease range and showed that the relative error $\Delta\epsilon/\epsilon$ could be expressed by the formula

$$\frac{\Delta\epsilon}{\epsilon} = -\frac{2}{3} \xi_{01}^2 \frac{(\epsilon - 1)}{\epsilon} \left(1 - \frac{b}{a}\right)^3 \quad (26)$$

where ξ_{01} is the root of the Bessel function $J_1(x)$, and b and a are the specimen and cavity diameters, respectively.

The values of "apparent error" shown in Table 3 are a first-order approximation based on the assumption that the initial readings at 2.135-inches are "correct." As Table 4 shows, the inaccuracy incurred in the value of dielectric constant by making this assumption is not zero but amounts to 0.1 percent. Table 4 presents the values obtained from Equation (26).

The measured first-order "apparent error" values of Table 3 can be brought into agreement with the "true" calculated values of dielectric constant by graphical transformation (shifting the Y-axis of Figure 41 over to the first measured value on the X-axis).

In summary, then, the results indicate that a clearance (gap) between the dielectric specimen and cavity wall introduces a systematic error in the measurement of complex permittivity by the TE_{01n} resonant cavity technique.

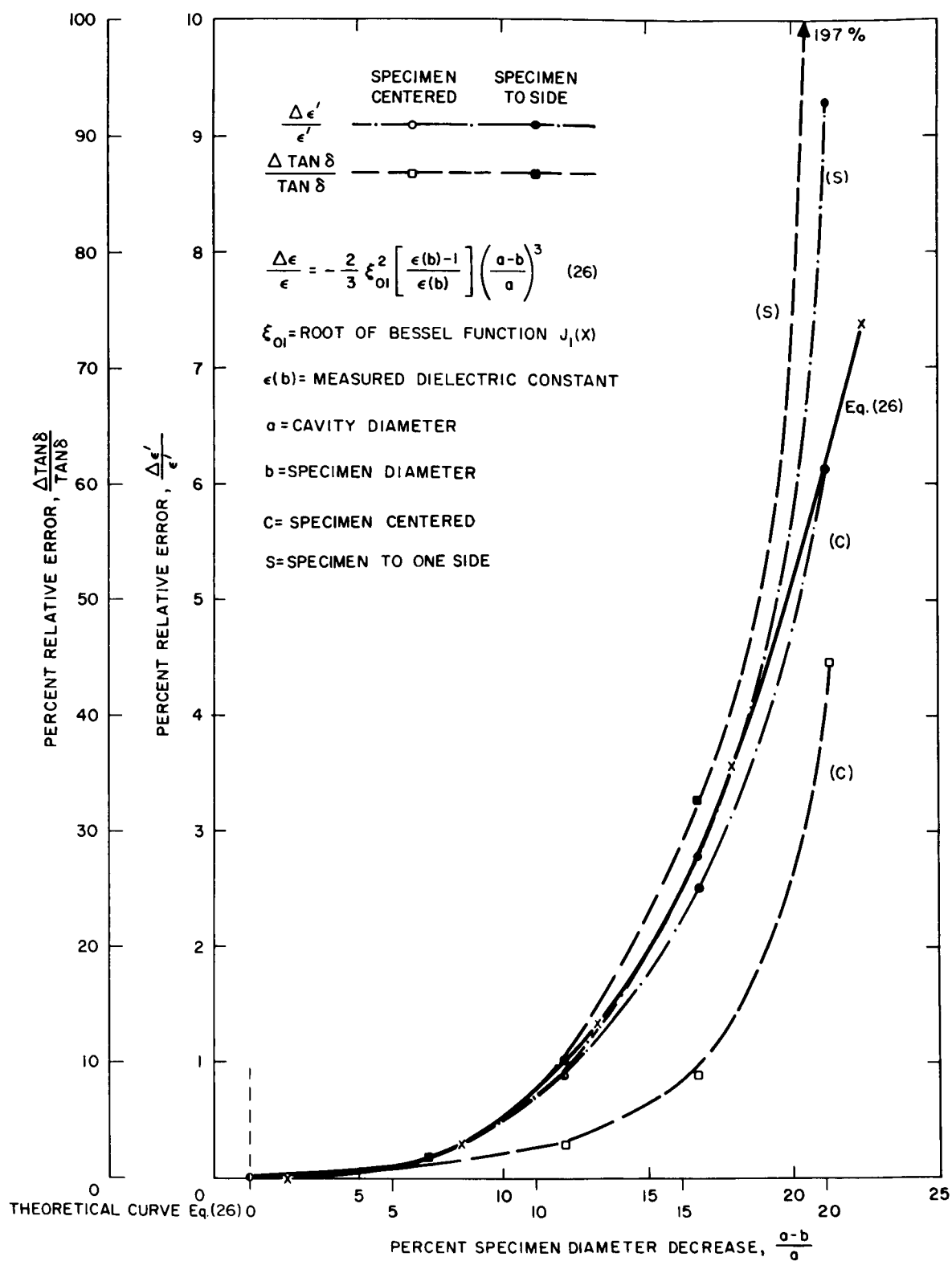


Figure 41. Effect of specimen diameter on dielectric properties measured in a TE_{015} cavity resonator.

Specimen Diameter, b (inches)	Diameter Decrease, $\frac{a-b}{a}$ (percent)	C				S			
		Dielectric Constant, ϵ'	Apparent Error, $\frac{\Delta\epsilon'}{\epsilon'}$ (percent)	Loss Tangent, $\tan \delta$	Apparent Error, $\frac{\Delta \tan \delta}{\tan \delta}$ (percent)	Dielectric Constant, ϵ'	Apparent Error, $\frac{\Delta\epsilon'}{\epsilon'}$ (percent)	Loss Tangent, $\tan \delta$	Apparent Error, $\frac{\Delta \tan \delta}{\tan \delta}$ (percent)
2.135	1.16	4.744		0.01081					
		4.746		0.01079					
		4.745	0	0.01080	0	—	—	—	—
2.000	7.41	4.736		0.01094		4.739		0.00194	
		4.736		0.01110		4.734		0.01115	
		4.736	0.19	0.01102	2.04	4.7365	0.18	0.01104 ₅	2.27
1.900	12.04	4.705		0.01112		4.702		0.01195	
		4.704		0.01112		4.702		0.01187	
		4.704 ₅	0.88	0.01112	2.96	4.702	0.91	0.01191	10.28
1.800	16.67	4.626		0.01168		4.610		0.01409	
		4.627		0.01186		4.615		0.01460	
		4.626 ₅	2.50	0.01177	8.98	4.6125	2.79	0.01434 ₅	32.82
1.700	21.30	4.461		0.01555		4.308		0.03219	
		4.445		0.01571		4.297		0.03189	
		4.453	6.15	0.01563	44.72	4.3025	9.33	0.03204	196.67

Table 3. Effect of specimen diameter on measured dielectric properties in a cavity dielectrometer. The values of "apparent error" shown above are first-order approximations. Values in agreement with Equation (26) are obtained by the graphical transformation shown in Figure 41. (Specimen 0.2930 inch thick; cavity diameter $a = 2.160$ inches; C = centered on plunger; S = near or against side of cavity.)

Specimen Diameter, b (inches)	Diameter Decrease, $\frac{a-b}{a}$ (percent)	Relative Error, $\frac{\Delta\epsilon}{\epsilon}$ (percent)
2.160	0	0
2.135	1.16	0.1206
2.000	7.41	0.3142
1.900	12.04	1.345
1.800	16.67	3.554
1.700	21.30	7.336

Table 4. Dielectric-constant relative-error values calculated by Equation (26), as a function of specimen diameter. (Cavity diameter $a = 2.160$ inches.)

For the dielectric-constant measurements, the magnitude of the error appears to agree with theoretical calculations and is approximately a cubic function of the gap size. (It varies directly with the cube of the specimen diameter, and inversely with the measured dielectric-constant value and the cube of the cavity diameter.)

The inaccuracy in the loss-tangent measurement also increases exponentially with increase in gap size. A theoretical expression for the loss-tangent error needs to be derived.

For both dielectric-constant and loss-tangent measurements, the inaccuracy was least when the specimen was axially centered on the plunger end-plate of the cavity.

B. Effect of Specimen Thickness

A series of tests were run to determine the effect of thickness on the measured values of permittivity for the materials to be used in the first (electron) irradiation run. For convenience in the dc resistivity measurements, it was hoped to use the same thickness throughout.

One specimen from each of the proposed materials (Section 4.5) was prepared and permittivity measurements were made in air as the specimens were machined successively to a thickness of approximately $1/2$, $3/8$, $1/4$ and $1/8$ wavelengths. Specimen wavelength, λ_s , is calculated by Equation (4), Section 2.6.

The results are presented in Figures 42 and 43. With decrease in thickness, the specimens display a gradual increase in (relative) dielectric constant, and a maximum in loss tangent at approximately $1/4$ -wavelength.

Tables 5 and 6 show the values of permittivity measured in air for the 32 specimens of irradiation Run No. 1. These specimens were prepared with the same thickness of 0.310-inch, which corresponds to specimen wavelength thickness (b/λ_s) between 0.3 and 0.5. This range is similar to that used by other workers.⁽²⁵⁾

The apparent high dielectric loss for the Teflon specimens in Table 5 was unexpected. On the basis of the previous measurements (see Figure 43), the Teflon specimens should have shown a loss tangent

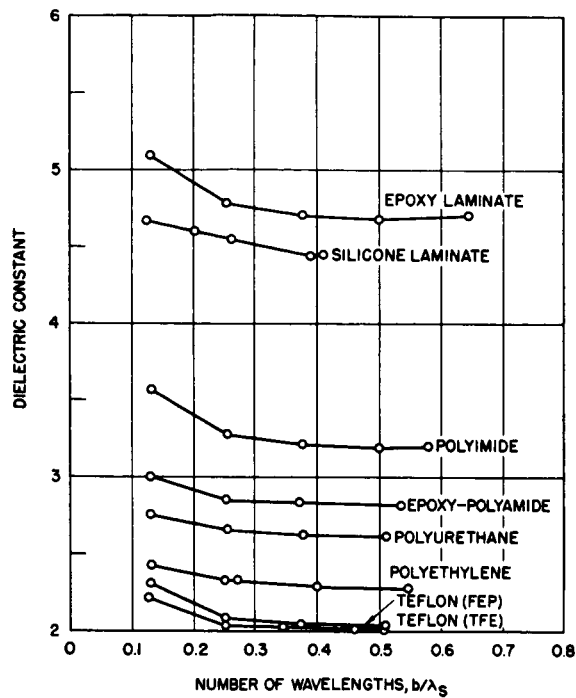


Figure 42. Microwave (9.28 GHz) dielectric constant as a function of specimen thickness.

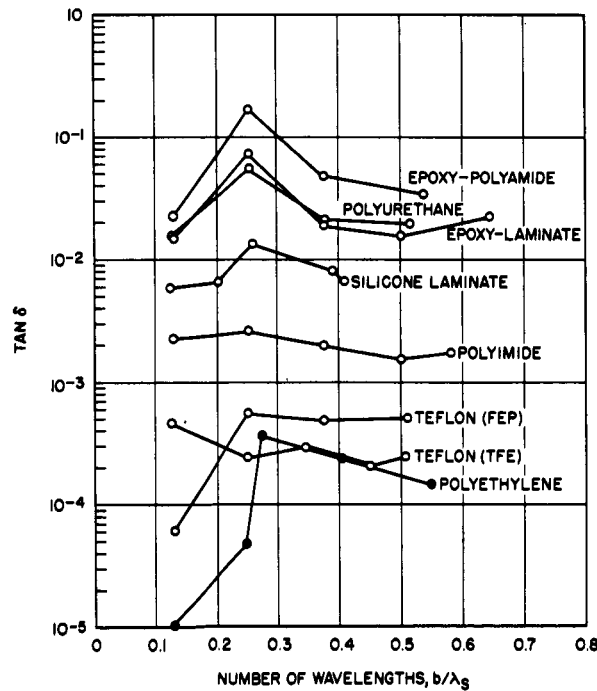


Figure 43. Microwave (9.28 GHz) loss tangent as a function of specimen thickness.

Material	Number	$\frac{b}{\lambda_s}$	$\bar{\epsilon}'_s$	$\tan \delta$
Epoxy laminate	A1U	0.495	4.63 ₃	1.54×10^{-2}
	A1D	0.495	4.63 ₈	1.54
	A2U	0.495	4.63 ₉	1.57
	A2D	0.495	4.64 ₁	1.56
	A3U	0.495	4.64 ₂	1.54
	A3D	0.495	4.64 ₃	1.58
	A4U	0.495	4.64 ₁	1.56
	A4D	0.495	4.64 ₂	1.56
Silicone laminate	B1U	0.414	3.39 ₄	6.50×10^{-3}
	B1D	0.414	3.39 ₄	6.39
	B2U	0.414	3.40 ₁	7.84
	B2D	0.414	3.40 ₂	8.18
	B3U	0.414	3.40 ₁	7.08
	B3D	0.414	3.40 ₁	7.22
	B4U	0.414	3.40 ₀	8.26
	B4D	0.414	3.40 ₀	6.93
Polyurethane	C1U	0.356	2.65 ₂	2.11×10^{-2}
	C1D	0.356	2.64 ₅	2.11
	C2U	0.357	2.66 ₅	2.12
	C2D	0.357	2.65 ₇	2.11
	C3U	0.357	2.65 ₅	2.17
	C3D	0.357	2.65 ₈	2.13
	C4U	0.356	2.65 ₀	2.39
	C4D	0.357	2.65 ₈	2.33

Table 5. Pre-irradiation permittivity of specimens, 0.310 inch thick, at 9.28 GHz.

Material	Number	$\frac{b}{\lambda_s}$	$\frac{1}{\epsilon_s}$	$\tan \delta$
Epoxy-polyamide	D1U	0.368	2.79 ₅	2.69×10^{-2}
	D1D	0.368	2.79 ₅	2.69
	D2U	0.372	2.83 ₉	4.70
	D2D	0.372	2.84 ₁	4.67
	D3U	0.371	2.82 ₇	3.92
	D3D	0.370	2.82 ₂	3.98
	D4U	0.368	2.79 ₃	2.76
	D4D	0.368	2.79 ₇	2.74
Polymide	E1U	0.400	3.21 ₄	2.02×10^{-3}
	E1D	0.401	3.21 ₇	2.14
	E2U	0.401	3.21 ₅	1.99
	E2D	0.401	3.21 ₈	2.10
	E3U	0.401	3.22 ₀	2.11
	E3D	0.401	3.21 ₈	2.04
	E4U	0.401	3.21 ₇	1.95
	E4D	0.401	3.21 ₇	2.10
Teflon (FEP)*	F1U	0.303	2.05 ₇	4.95×10^{-3}
Teflon (TFE)*	G1U	0.302	2.04 ₈	6.38×10^{-3}
Polyethylene	H1U	0.326	2.30 ₂	1.04×10^{-4}
	H1D	0.326	2.30 ₄	1.22
	H2U	0.326	2.30 ₂	0.86
	H2D	0.326	2.30 ₁	1.03
	H3U	0.326	2.30 ₂	0.86
	H3D	0.326	2.30 ₂	1.12
	H4U	0.326	2.29 ₉	1.12
	H4D	0.326	2.29 ₉	1.03
* See Table 6 for subsequent measurements.				

Table 5 (continued). Pre-irradiation permittivity of specimens, 0.310 inch thick, at 9.28 GHz.

Material	Number	$\frac{b}{\lambda_s}$	$\bar{\epsilon}'_s$	$\tan \delta$
Teflon (FEP)	F1U	0.274	2.05 ₉	5.12×10^{-4}
	F1D	0.274	2.06 ₂	5.12
	F2U	0.274	2.06 ₄	6.09
	F2D	0.274	2.06 ₉	6.40
	F3U	0.275	2.08 ₁	6.21
	F3D	0.274	2.06 ₈	5.92
	F4U	0.274	2.06 ₇	5.76
	F4D	0.274	2.06 ₁	5.44
Teflon (TFE)	G1U	0.274	2.06 ₄	2.35×10^{-4}
	G1D	0.274	2.06 ₄	2.19
	G2U	0.272	2.04 ₃	2.73
	G2D	0.272	2.04 ₄	2.40
	G3U	0.274	2.06 ₄	2.03
	G3D	0.274	2.06 ₇	2.35
	G4U	0.274	2.06 ₄	2.21
	G4D	0.274	2.06 ₃	2.05

Table 6. Pre-irradiation permittivity of Teflon specimens, 0.280 inch thick, at 9.28 GHz.

of about $3-5 \times 10^{-4}$ at a thickness of 0.3 wavelength. Instead, values 10-20 times higher were observed.

After conducting a number of different experiments to resolve the mystery, it was noticed that two "poor" Teflon discs, each 0.310 inch thick, showed low loss when stacked together in the dielectrometer.

Hence, a test was then made wherein the loss of a Teflon specimen was carefully examined in the vicinity of 0.3 wavelength. A 1/2-inch thick disc was gradually thinned on a belt sander and its half power bandwidth, Δl , measured. The results are shown in Figure 44.

The loss tangent is directly related to Δl by the expression given in Equation (8) of Section 2.6. If the peak point in Figure 44 is fed into Equation (8), a loss-tangent value of 1.3×10^{-2} is obtained, about 2 decades too high.

The sharp but high peak in Figure 44 may be due to mode conversion in our particular cavity and is obviously not indicative of the specimen's dielectric properties. Its appearance at 0.3 wavelength instead of at $\lambda/4$ may be associated with a low value of dielectric constant. Polyethylene was also found to exhibit an anomalous loss at about 0.3 wavelength, as shown in Figure 45.

A final set of Teflon specimens was then prepared, machining them to a thickness of 0.280 inch. The measured permittivity values are shown in Table 6.

4.5 ELECTRON IRRADIATION RUN NO. 1

A. Specimen Preparation

The test specimens were prepared from the following material classes:

1. Epoxy-fiberglass laminate
2. Silicone-fiberglass laminate
3. Polyurethane
4. Epoxy-polyamide
5. SP-1 polyimide
6. FEP Teflon
7. TFE Teflon
8. Polyethylene

The epoxy-fiberglass laminate conforms to specification MIL-P-18177. It was obtained from Mica Corporation as Micaply EG 758, type GEE. The resin content is approximately 40 percent.

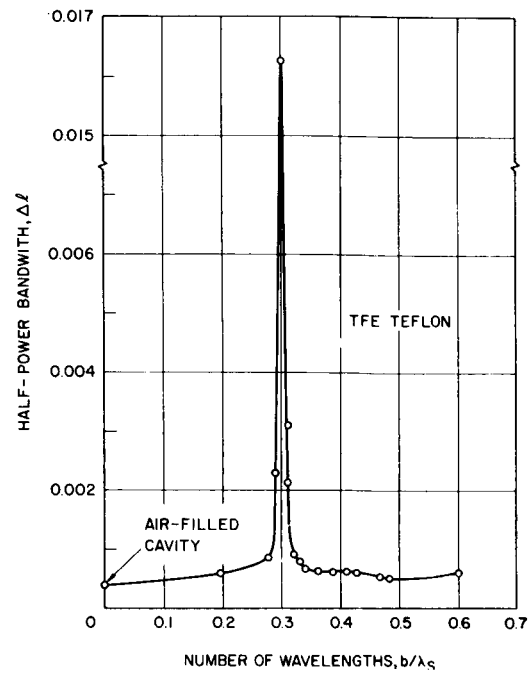


Figure 44. Resonance half-power bandwidth of TFE Teflon as a function of specimen thickness.

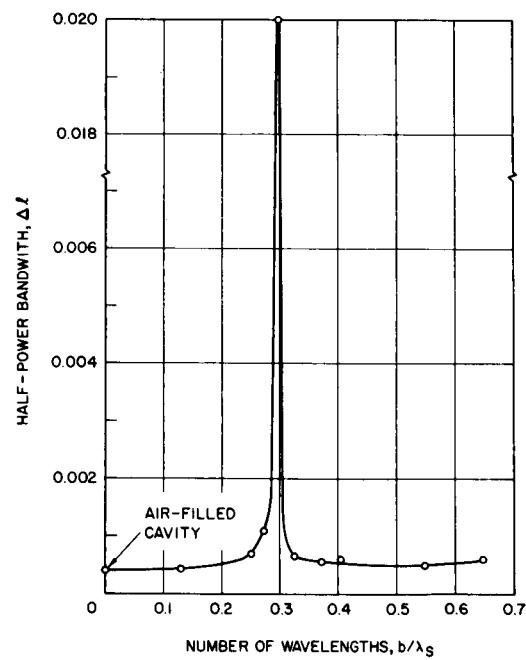


Figure 45. Resonance half-power bandwidth of polyethylene as a function of specimen thickness.

The silicone-fiberglass laminate was prepared as follows: Thirty-five plies of DC 2106 (Dow Corning Co.) impregnated S(994)-glass cloth were press-cured at 200 psi for 2 hours at 250°F. The cured laminate was postcured for 48 hours at 302°F, 48 hours at 390°F, and, finally, 72 hours at 482°F. The resin content is 41.6 percent.

The polyurethane was made from components supplied by Thiokol Chemical Co. as Solithane 113. The formulation consists in mixing 100 parts of the isocyanate resin with 74 parts of the polyol curing agent, and curing overnight at 180°F. Castings, 2-1/2-inch in diameter, were prepared first and then subsequently machined into the test specimens.

The epoxy-polyamide was made by mixing 100 parts of Epon 828 (Shell Chemical Co.) with 21 parts of Versamid 125 (General Mills Co.) and 13 parts of menthane diamine, and then curing overnight at 180°F. Castings 2-1/2-inch in diameter were prepared first and then subsequently machined into the test specimens. The material conforms to Hughes specification HP-16-66, Type II, Class I.

The SP-1 polyimide is the base unmodified resin used in duPont's Vespel parts. The specimens were graciously supplied by N. W. Todd of E. I. duPont de Nemours and Company.

The FEP Teflon was manufactured by Raybestos Manhattan Inc. as a 2-1/2-inch diameter rod.

The TFE Teflon was obtained from Western Fibrous Co. in the form of 1/2-inch thick sheet.

The polyethylene material is low density grade, per specification MIL-P-227488. It was manufactured by Allied Resinous Inc. (and obtained through Cadillac Plastics and Chemical Co.) as a 2-1/2-inch diameter rod.

The test specimens were prepared as flat discs, 2.135 (+ 0.000; - 0.005) inches in diameter, and thickness 0.310 inch for all except the Teflon specimens. The latter were made 0.280-inch thick, for reasons outlined in Section 4.4. Four specimens were prepared from each material, for a total of 32 specimens.

B. Electron Irradiation

It had originally been planned to keep one specimen outside the chamber as a control, and to introduce the other three specimens from each material class into the environmental chamber. Time did not permit a duplicate irradiation schedule however, so only two specimens (No. 1 and No. 3) from each class were placed in the chamber. No. 1 was irradiated and No. 3 served as a vacuum control.

Irradiation was provided by a resonant-transformer²⁶ 1 Mev electron beam generator, shown in Figure 46. The environmental chamber was pumped down to the low 10^{-9} torr range and placed below the generator with the target (test specimen) at a distance of 10 inches from the exit window of the generator. The electron beam traversed a 3-inch long air passage before entering the chamber at the 6-mil thick titanium window (described in Section 2.2). A 1/8-inch aluminum plate with a 2-inch diameter hole provided preliminary beam collimation outside the chamber, and a 2-inch diameter aluminum tube inside the chamber provided additional collimation. Current picked up on this aluminum plate (insulated from ground) was used to monitor dose rate in accordance with the calibration curve of Figure 29 in Section 3. Current on the generator console meter read approximately twice the aluminum plate values.

The irradiation was conducted according to the schedule shown in Table 7.

Step	Current (μ a)	Time (sec)	Dose Rate (rads/sec)	Dose (rads)	Accumulated Dose (rads)
1A	7	100	1×10^2	1.0×10^4	1.0×10^4
1B	72	100	1×10^3	1.0×10^5	1.1×10^5
1C	645	100	9×10^3	9.0×10^5	1.0×10^6
1D	1290	500	1.8×10^4	9.0×10^6	1.0×10^7
1E	2580	2500	3.6×10^4	9.0×10^7	1.0×10^8

Table 7. Parameters for irradiation Run No. 1.

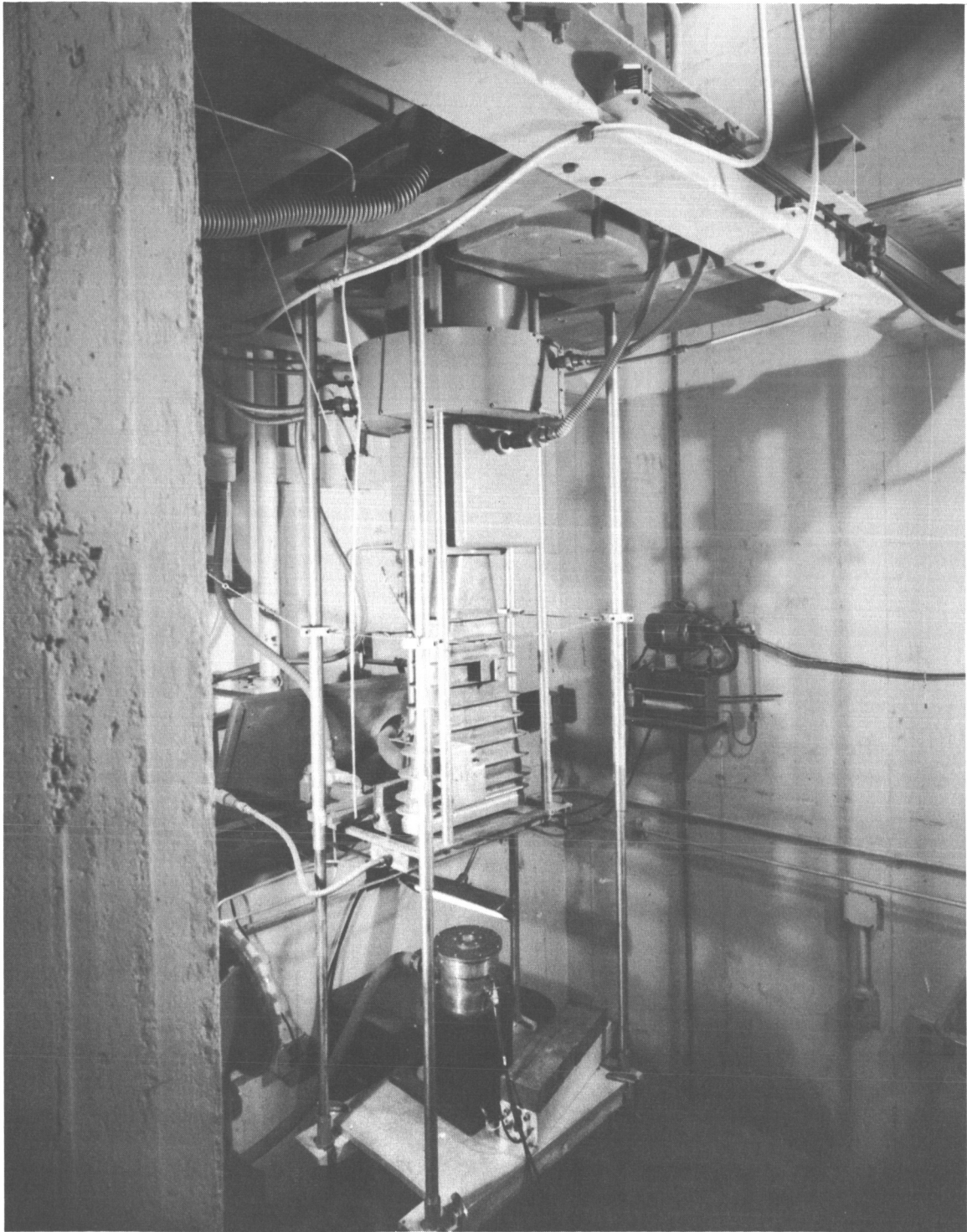


Figure 46. Electron beam generator.
(HAC Photo No. GS64-05-014)

Figure 47 illustrates the numbering system for the turntable specimen holders. The disposition of the various specimens on the turntable is indicated below:

<u>Specimen</u>	<u>Position</u>
Epoxy laminate A1	1
Silicone laminate B1	3
Polyurethane C1	5
Epoxy-polyamide D1	7
Polyimide E1	9
FEP Teflon F1	11
TFE Teflon G1	13
Polyethylene H1	15
Epoxy laminate A3	17
Silicone laminate B3	18
Polyurethane C3	19
Epoxy-polyamide D3	20
Polyimide E3	21
FEP Teflon F3	22
TFE Teflon G3	23
Polyethylene H3	24

At each dose level, all the No. 1 specimens (positions 1-15) were irradiated in sequence before making the dc resistivity measurements. The No. 3 specimens were not directly irradiated. Time did not permit extending the radiation dose beyond 10^8 rads (which corresponds to an exposure of approximately 10^{14} - 10^{15} electrons/cm²).

At the conclusion of the final irradiation and corresponding dc resistivity measurements, air was admitted into the chamber and resistivity measurements were again taken. Four weeks later, further resistivity measurements were made in air, in the chamber, on all specimens (Nos. 1 through 4). These final measurements in air are of dubious value as some of the specimens (A, C, and D) show strong effects of moisture. The control specimens A2 and A4, C2 and C4, and D2 and D4, for instance, had to be oven dried at 100°C for 24 hours to stabilize them (see Figure 53).

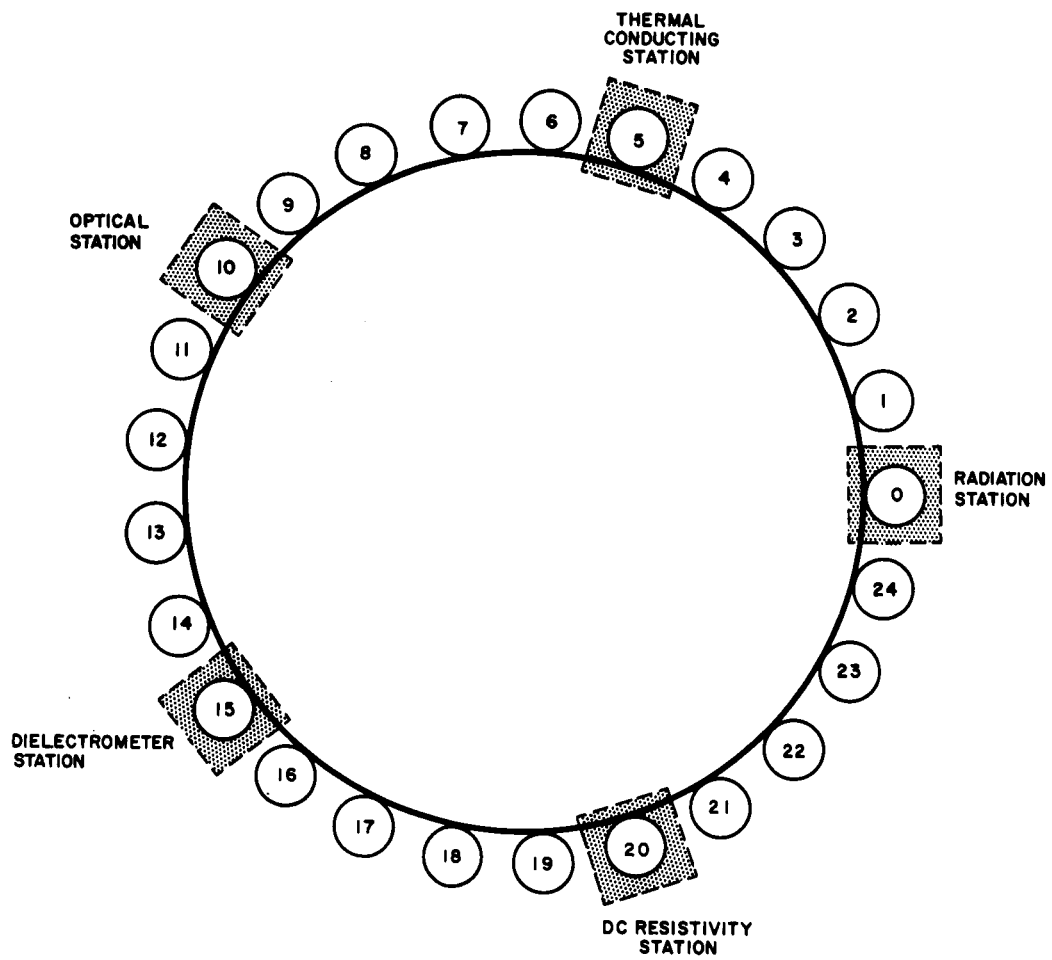


Figure 47. Specimen layout positions on turntable (top view).

Post-irradiation measurements were also made of dielectric constant and dissipation factor at 1 kHz on all the specimens. These measurements were made in a Hartshorn holder (General Radio Co. Dielectric Sample Holder 1690-A) in conjunction with a General Radio Co. Model 716-C Capacitance Bridge, Model 1231-B Amplifier and Null Detector, and Model 1302-A oscillator.

C. Results, Observations, and Discussion

Figures 48 through 52 are photographs of the test specimens. The translucent specimens (C1, D1, F1, and H1) display typical Lichtenberg figures (trees). Some of the specimens also showed a discoloration on their top, irradiated surface. The discolored area appears to be limited to a depth of approximately 1 mm.

The visual appearance of the top surface of the various specimens after irradiation is somewhat as follows:

A1, Epoxy laminate: Changed from green to brown.

B1, Silicone laminate: Slightly lighter in color than the original tan.

C1, Polyurethane: Lemon color had changed to brown-orange. Texture also somewhat harder. Displayed "trees."

D1, Epoxy-polyamide: Darker, browner. Specimen thickness had increased by about 0.003 inch. Displayed "trees."

E1, Polyimide: No apparent change.

F1, FEP Teflon: Same color. Displayed "trees."

G1, TFE Teflon: No apparent change.

H1, Polyethylene: Original white had yellowed somewhat. Displayed "trees."

Specimen G1 (TFE Teflon) came out of its holder after it had received a dose of 10^5 rads and could not be irradiated any further.

Upon irradiation, most of the specimens had a tendency to stick to the radiation station holding clamp. It might be advisable in future runs to support the specimens on the radiation station heat sink without clamping them.

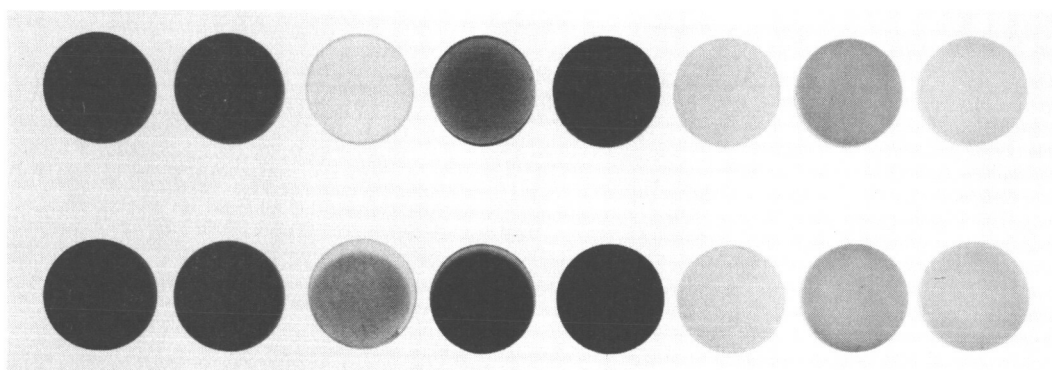


Figure 48. View of non-irradiated (top row) and irradiated (bottom row) specimens. Specimens are in alphabetical sequence beginning with A on the left (HAC Photo No. R112542).

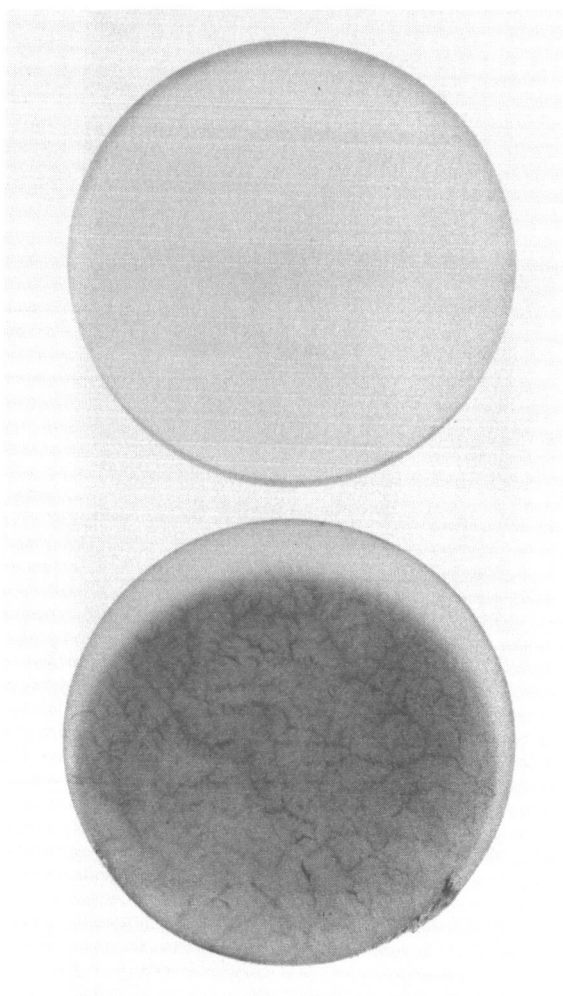


Figure 49. Non-irradiated and irradiated polyurethane (HAC Photo No. R112543).

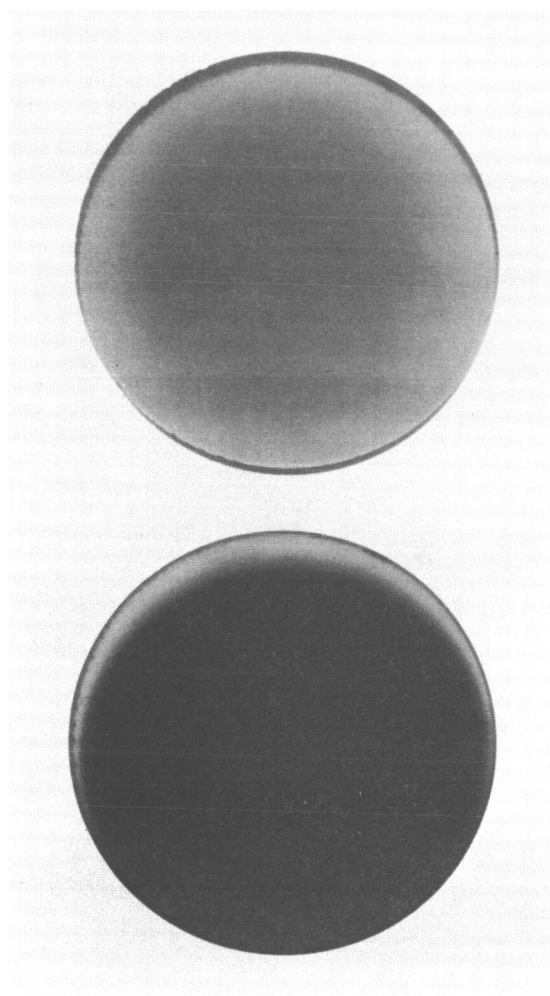


Figure 50. Non-irradiated and irradiated epoxy-polyamide (HAC Photo No. R112544).

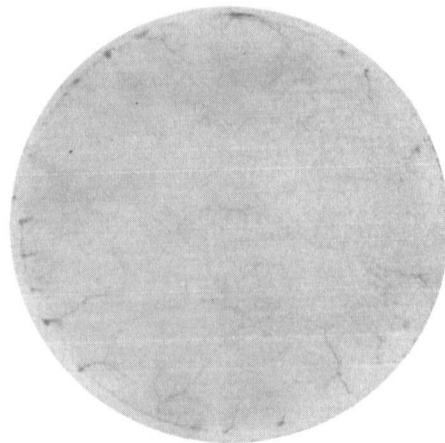
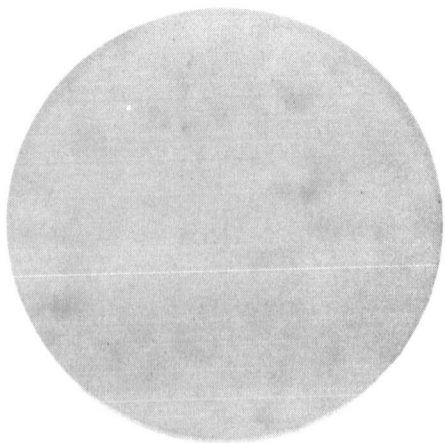


Figure 51. Non-irradiated and irradiated TFE Teflon (HAC Photo No. R112545).

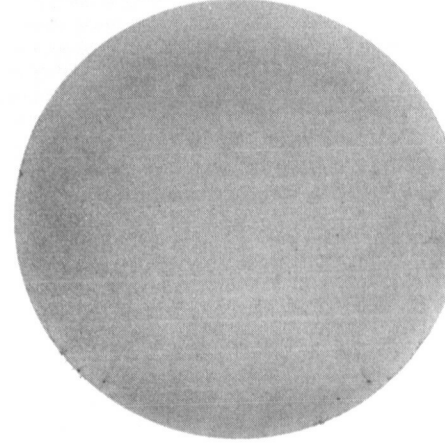
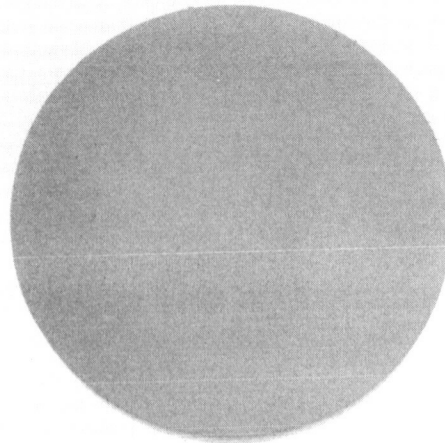


Figure 52. Non-irradiated and irradiated polyethylene (HAC Photo No. R112546).

The pressure in the chamber during irradiation was maintained in the 10^{-9} - 10^{-8} torr range except at the higher dose rates that had to be used for the last two decades (10^7 and 10^8 rads). In the 10^7 rad run, the gas pressure rose into the low 10^{-7} torr range on irradiating the polyurethane and the polyethylene. In the 10^8 rad run, it went into the low 10^{-7} torr when irradiating the epoxy-polyamide, into the high 10^{-7} torr with the polyurethane, and into the 10^{-6} range with the polyethylene and the (F1) Teflon.

The outgassing at high dose rates of the polyethylene was probably thermal in origin for the high vapor pressure manifested itself as soon as the electron beam was turned on and remained fairly constant. The F1 Teflon specimen, however, did not start outgassing until the 10^8 rad irradiation (step 1E of Table 8) had been in progress for about 10 minutes, and the pressure continually increased, reaching even the low 10^{-5} torr region by the end of the irradiation period.

Table 8 and Figure 53 show the measured values of resistivity as a function of dose. Resistivity was calculated by Equations (21) and (22) given in Section 4.3.

It appears that the FEP Teflon and the silicone fiberglass laminate were quite stable. It is unfortunate that the TFE Teflon specimen (G1) could not be irradiated, but the fact that the "control" G3 showed a decrease in air-measured resistivity might indicate that TFE is less radiation resistant than the FEP variety. Further irradiation tests are obviously required.

The polyurethane specimen C1 was affected after a 10^5 rad dose, and the accompanying C3 vacuum-control was also affected during the final irradiation step. Another vacuum-control to show a radiation effect was the polyethylene No. 3. These two specimens apparently were affected by stray, possibly bremsstrahlung, radiation.

The epoxy specimens A1 and D1 showed a drop in resistivity after 10^6 rads but appear to recover on further irradiation.

The polyethylene specimen H1 was affected after 10^8 rads but appears to have recovered after 4 weeks storage in air.

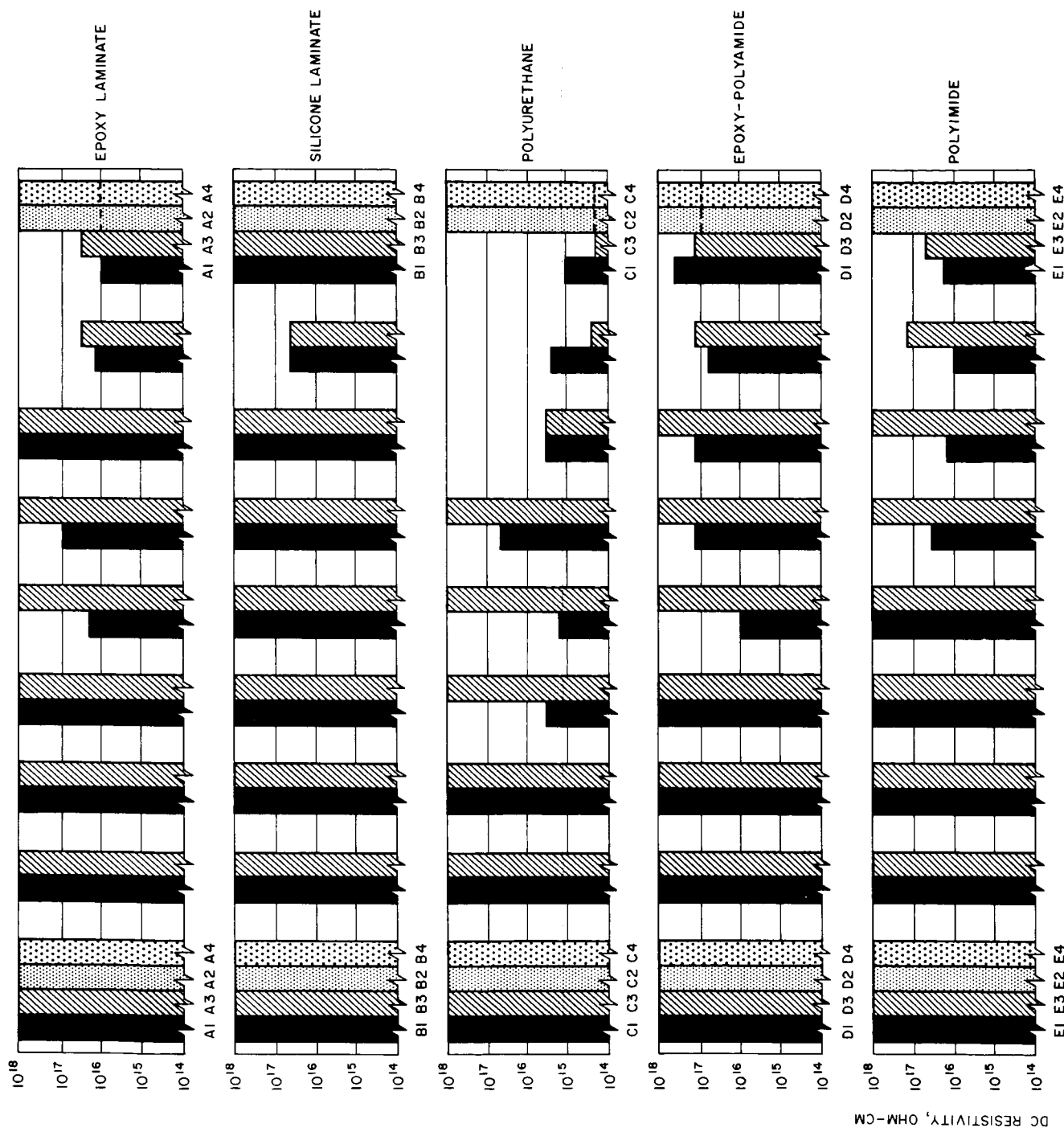
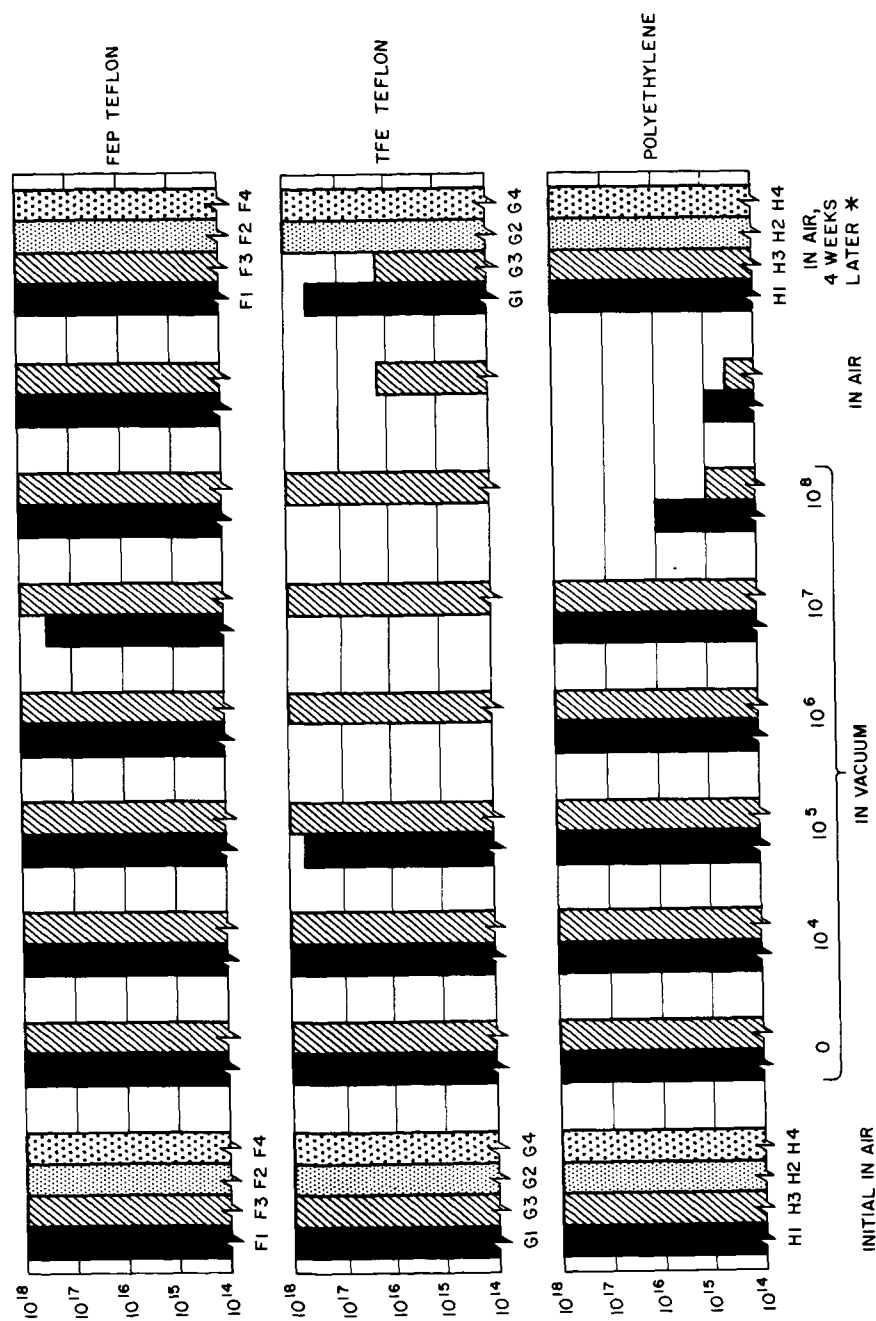


Figure 53. Resistivity measurements as a function of 1 Mev electron dose in rads. (*In the final air measurements, the dashed lines in the A2, A4, C2, C4, and D2, D4 controls represent values obtained before these specimens were oven dried. The No. 1 and No. 3 specimens were not oven dried.)



Specimen	Initial, In Air	Dose, in rads						10^8 In Air	10^8 In Air 4 Weeks Later	
		0	10^4	10^5	10^6	10^7	10^8			
		← In Vacuum →								
Epoxy laminate	A1	$>10^{18}$	$>10^{18}$	$>10^{18}$	$>10^{18}$	3×10^{16}	1×10^{17}	$>10^{18}$	3×10^{16}	1×10^{16}
(Control)	A3	$>10^{18}$	$>10^{18}$	$>10^{18}$	$>10^{18}$	$>10^{18}$	$>10^{18}$	$>10^{18}$	6×10^{16}	4×10^{16}
Silicone laminate	B1	$>10^{18}$	$>10^{18}$	$>10^{18}$	$>10^{18}$	$>10^{18}$	$>10^{18}$	$>10^{18}$	6×10^{16}	$>10^{18}$
(Control)	B3	$>10^{18}$	$>10^{18}$	$>10^{18}$	$>10^{18}$	$>10^{18}$	$>10^{18}$	$>10^{18}$	6×10^{16}	$>10^{18}$
Polyurethane	C1	$>10^{18}$	$>10^{18}$	$>10^{18}$	6×10^{15}	3×10^{15}	7×10^{16}	6×10^{15}	4×10^{15}	1×10^{15}
(Control)	C3	$>10^{18}$	$>10^{18}$	$>10^{18}$	$>10^{18}$	$>10^{18}$	$>10^{18}$	6×10^{15}	4×10^{14}	10^{14}
Epoxy-polyamide	D1	$>10^{18}$	$>10^{18}$	$>10^{18}$	$>10^{18}$	1×10^{16}	2×10^{17}	2×10^{17}	8×10^{16}	6×10^{17}
(Control)	D3	$>10^{18}$	$>10^{18}$	$>10^{18}$	$>10^{18}$	$>10^{18}$	$>10^{18}$	$>10^{18}$	2×10^{17}	2×10^{17}
Polyimide	E1	$>10^{18}$	$>10^{18}$	$>10^{18}$	$>10^{18}$	$>10^{18}$	6×10^{16}	2×10^{16}	1×10^{16}	3×10^{16}
(Control)	E3	$>10^{18}$	$>10^{18}$	$>10^{18}$	$>10^{18}$	$>10^{18}$	$>10^{18}$	$>10^{18}$	2×10^{17}	7×10^{16}
FEP Teflon	F1	$>10^{18}$	$>10^{18}$	$>10^{18}$	$>10^{18}$	$>10^{18}$	5×10^{17}	$>10^{18}$	$>10^{18}$	$>10^{18}$
(Control)	F3	$>10^{18}$	$>10^{18}$	$>10^{18}$	$>10^{18}$	$>10^{18}$	$>10^{18}$	$>10^{18}$	$>10^{18}$	$>10^{18}$
TFE Teflon	G1	$>10^{18}$	$>10^{18}$	$>10^{18}$	7×10^{17}	-	-	-	-	6×10^{17}
(Control)	G3	$>10^{18}$	$>10^{18}$	$>10^{18}$	$>10^{18}$	$>10^{18}$	$>10^{18}$	$>10^{18}$	2×10^{16}	2×10^{16}
Polyethylene	H1	$>10^{18}$	$>10^{18}$	$>10^{18}$	$>10^{18}$	$>10^{18}$	$>10^{18}$	1×10^{16}	1×10^{15}	$>10^{18}$
(Control)	H3	$>10^{18}$	$>10^{18}$	$>10^{18}$	$>10^{18}$	$>10^{18}$	$>10^{18}$	1×10^{15}	5×10^{14}	$>10^{18}$
Note: Specimen G1 came out of its holder after 10^5 rads and remained in vacuum without further direct irradiation.										

Table 8. DC volume resistivity of 0.3-inch thick specimens irradiated in vacuum with 1 Mev electrons as a function of dose (in rads). Resistivity values for the vacuum controls, which were not directly irradiated, are shown under each specimen.

Somewhat unexpected was the behavior of the polyimide resin. As far as resistivity is concerned, the E1 specimen was definitely affected by radiation after a 10^7 rad dose. The vacuum-control E3 also showed evidence of having been affected by stray radiation for in the post-irradiation measurements in air it was inferior to the non-vacuum controls E2 and E4 (which showed a resistivity greater than 10^{18} ohm-cm)

The measured changes in volume resistivity of the irradiated specimens are not as great as might be observed with thin films or with thinner specimens. It is recommended in future irradiation studies of this type that thin specimens be used, and also that surface resistance measurements be made. By suitable switching arrangements,²⁷ it is possible to make use of the measuring circuit of Figure 21 (Section 2.5) to determine surface as well as volume resistance. The surface resistance should, of course, be measured on the surface that is directly exposed to the radiation.

As mentioned earlier, microwave permittivity measurements were made (in air) on all the specimens prior to and after the irradiation. Tables 9 and 10 summarize the results. With the exception of the polyurethane specimen C1 and the FEP Teflon F1, no significant change in permittivity occurred. The polyurethane specimen also displayed an early drop in resistivity during the irradiation. Examination of Table 10 also reveals that although all of the polyimide specimens became lossier with time, the two specimens (E1 and E3) that were placed in the vacuum chamber displayed a smaller increase in loss tangent.

A final series of measurements were conducted on the irradiated specimens and their controls. This consisted of determining the low frequency (1 kHz) dielectric constant and dissipation factor using General Radio Capacitance Bridge (716-C) and Hartshorn type holder (1690-A). The results are given in Table 11.

Since low-frequency measurements had not been made prior to the irradiation, it is not possible to determine directly if any changes took place in the irradiated specimens. But indirectly, it is possible to compare the irradiated specimens with the controls by intercomparing the values of all the specimens in a material class, and also by comparing the final values of low-frequency and of microwave permittivity. As shown in Table 11, only the polyurethane C1 and the epoxy-polyamide D1 showed any appreciable change.

(a) Material	(b) Specimen	Initial (c)		Final (d)		$\Delta \bar{\epsilon}'_s$, percent	$\Delta \tan \delta$, percent
		$\bar{\epsilon}'_s$	$\tan \delta$	$\bar{\epsilon}'_s$	$\tan \delta$		
Epoxy laminate	A1U	4.633	0.0154	4.639	0.0149	0.13	-3.2
	A1D	4.638	0.0154	4.640	0.0150	0.04	-2.6
	A3U	4.642	0.0154	4.639	0.0148	-0.06	-3.9
	A3D	4.643	0.0158	4.641	0.0147	-0.04	-7.0
	A2U	4.634	0.0157	4.642	0.0152	0.06	-3.2
	A2D	4.641	0.0156	4.640	0.0150	-0.02	-3.8
	A4U	4.641	0.0156	4.637	0.0147	-0.09	-5.8
	A4D	4.642	0.0156	4.640	0.0148	-0.04	-5.1
Silicone laminate	B1U	3.394	0.00650	3.391	0.00630	-0.09	-3.1
	B1D	3.394	0.00639	3.389	0.00613	-0.15	-4.1
	B3U	3.401	0.00708	3.397	0.00699	-0.12	-1.3
	B3D	3.401	0.00722	3.398	0.00701	-0.09	-2.9
	B2U	3.401	0.00784	3.401	0.00783	0.00	-0.1
	B2D	3.402	0.00818	3.407	0.00816	0.15	-0.2
	B4U	3.400	0.00826	3.405	0.00816	0.15	-1.2
	B4D	3.400	0.00693	3.404	0.00699	0.11	0.9
Polyurethane	C1U	2.652	0.0211	2.681	0.0177	1.09	-16.1
	C1D	2.645	0.0211	2.720	0.0174	2.84	-17.5
	C3U	2.655	0.0217	2.651	0.0195	-0.15	-10.1
	C3D	2.658	0.0213	2.658	0.0195	0.00	-8.4
	C2U	2.665	0.0212	2.673	0.0190	0.30	-10.4
	C2D	2.657	0.0211	2.666	0.0207	0.34	-1.9
	C4U	2.650	0.0239	2.652	0.0220	0.08	-8.0
	C4D	2.658	0.0233	2.662	0.0217	0.15	-6.9

Table 9. Microwave (9.28 GHz) permittivity in air of Run No. 1 specimens.

(a) Material	(b) Specimen	Initial (c)		Final (d)		$\Delta \bar{\epsilon}'_s$, percent	$\Delta \tan \delta$, percent
		$\bar{\epsilon}'_s$	$\tan \delta$	$\bar{\epsilon}'_s$	$\tan \delta$		
Epoxy-Polyamide	D1U	2.795	0.0269	2.817	0.0204	0.79	-24.2
	D1D	2.795	0.0269	2.798	0.0204	0.11	-24.2
	D3U	2.827	0.0392	2.839	0.0287	0.42	-26.8
	D3D	2.822	0.0398	2.875	0.0291	0.11	-26.9
	D2U	2.839	0.0470	2.843	0.0301	0.14	-36.0
	D2D	2.841	0.0467	2.838	0.0313	-0.11	-33.0
	D4U	2.793	0.0276	2.810	0.0234	0.61	-15.2
	D4D	2.797	0.0274	2.823	0.0238	0.93	-13.1
Polyimide	E1U	3.214	0.00202	3.250	0.00345	1.12	70.8
	E1D	3.217	0.00214	3.248	0.00343	0.96	60.3
	E3U	3.220	0.00211	3.250	0.00327	0.93	55.0
	E3D	3.218	0.00204	3.253	0.00327	1.09	60.3
	E2U	3.215	0.00199	3.265	0.00402	1.56	102.0
	E2D	3.218	0.00210	3.266	0.00399	1.49	90.5
	E4U	3.217	0.00195	3.294	0.00533	2.39	173.3
	E4D	3.217	0.00210	3.291	0.00541	2.30	157.6
Teflon (FEP)	F1U	2.059	0.00051	2.063	0.00059	0.19	15.7
	F1D	2.062	0.00051	2.079	0.00058	0.83	13.7
	F3U	2.081	0.00062	2.075	0.00063	-0.29	1.6
	F3D	2.068	0.00059	2.067	0.00059	-0.05	0.0
	F2U	2.064	0.00061	2.067	0.00059	0.14	-3.3
	F2D	2.069	0.00064	2.066	0.00060	-0.14	-6.3
	F4U	2.067	0.00058	2.066	0.00059	-0.04	1.7
	F4D	2.061	0.00054	2.061	0.00053	0.00	-1.8

Table 9 (continued). Microwave (9.28 GHz) permittivity in air of Run No. 1 specimens.

(a) Material	(b) Specimen	Initial (c)		Final (d)		$\Delta \bar{\epsilon}_s'$ percent	$\Delta \tan \delta$, percent
		$\bar{\epsilon}_s'$	$\tan \delta$	$\bar{\epsilon}_s'$	$\tan \delta$		
Teflon (TFE)	G1U	2.064	0.00024	2.069	0.00020	0.24	-16.7
	G1D	2.064	0.00022	2.078	0.00023	0.68	4.5
	G3U	2.064	0.00020	2.071	0.00023	0.34	15.0
	G3D	2.067	0.00024	2.091	0.00026	1.16	8.3
	G2U	2.043	0.00027	2.047	0.00026	0.20	-3.7
	G2D	2.044	0.00024	2.049	0.00024	0.24	0.0
	G4U	2.064	0.00022	2.072	0.00027	0.39	22.7
	G4D	2.063	0.00021	2.071	0.00023	0.39	9.5
Polyethylene	H1U	2.302	0.00010	2.310	0.00020	0.35	100
	H1D	2.304	0.00012	2.303	0.00015	-0.04	25.0
	H3U	2.302	0.00009	2.314	0.00012	0.52	33.3
	H3D	2.302	0.00011	2.297	0.00012	-0.22	9.1
	H2U	2.302	0.00009	2.313	0.00012	0.48	33.3
	H2D	2.301	0.00010	2.297	0.00012	-0.17	20.0
	H4U	2.299	0.00011	2.298	0.00012	-0.04	9.1
	H4D	2.299	0.00010	2.299	0.00012	0.00	20.0
<p>Notes: (a) Materials used are described in the text.</p> <p>(b) Test specimens are discs, 2.135-inch in diameter. Thickness is 0.310-inch for all but those made from Teflon. The latter, specimens F and G, are 0.280-inch thick for reasons explained in the text. The letters U and D refer to "up" and "down" (i. e., inverted) positions, respectively.</p> <p>(c) The relative dielectric constant and loss tangent are calculated from Equations (5) and (8), respectively, Section 2.6.</p> <p>(d) The No. 1 specimens in each category (except for G1) were irradiated with 1 Mev electron to a total dose of 10^8 rads. Specimen G1 came out of its holder after it had received a dose of 10^5 rads, and remained in vacuum without further direct irradiation. The No. 3 specimens were placed in the same environment as the No. 1 specimens but were not directly irradiated. The No. 2 and No. 4 specimens in each category were kept outside of the environmental chamber as non-vacuum controls.</p>							

Table 9 (continued). Microwave (9.28 GHz) permittivity in air of Run No. 1 specimens.

		Dielectric Constant			Loss Tangent		
		Initial	Final	Percent Change	Initial	Final	Percent Change
Epoxy laminate	A1	4.63	4.64	0.0	0.015	0.015	0.0
	A3	4.64	4.64	0.0	0.016	0.015	- 6.2
	A2	4.64	4.64	0.0	0.016	0.015	- 6.2
	A4	4.64	4.64	0.0	0.016	0.015	- 6.2
Silicone laminate	B1	3.39	3.39	0.0	0.0064	0.0062	- 3.1
	B3	3.40	3.40	0.0	0.0071	0.0070	- 1.4
	B2	3.40	3.40	0.0	0.0080	0.0080	0.0
	B4	3.40	3.40	0.0	0.0076	0.0076	0.0
Polyurethane	C1	2.65	2.70	1.9	0.021	0.017	-19.1
	C3	2.66	2.66	0.0	0.021	0.020	- 4.8
	C2	2.66	2.67	0.4	0.021	0.020	- 4.8
	C4	2.65	2.66	0.4	0.023	0.022	- 4.3
Epoxy-Polyamide	D1	2.80	2.81	0.4	0.027	0.020	-26.0
	D3	2.82	2.83	0.4	0.040	0.029	-27.5
	D2	2.84	2.84	0.0	0.047	0.030	-36.2
	D4	2.80	2.82	0.7	0.027	0.024	-11.2
Polyimide	E1	3.21	3.25	1.2	0.0020	0.0034	70.0
	E3	3.22	3.25	0.9	0.0020	0.0033	65.0
	E2	3.22	3.27	1.5	0.0020	0.0041	105
	E4	3.22	3.29	2.2	0.0020	0.0053	165
Teflon (FEP)	F1	2.06	2.07	0.5	0.0005	0.0006	20
	F3	2.07	2.07	0.0	0.0006	0.0006	0
	F2	2.07	2.07	0.0	0.0006	0.0006	0
	F4	2.06	2.06	0.0	0.0006	0.0006	0
Teflon (TFE)	G1	2.06	2.07	0.5	0.0002	0.0002	0
	G3	2.06	2.08	1.0	0.0002	0.0002	0
	G2	2.04	2.05	0.5	0.0002	0.0002	0
	G4	2.06	2.07	0.5	0.0002	0.0002	0
Polyethylene	H1	2.30	2.31	0.4	0.0001	0.0002	100
	H3	2.30	2.30	0.0	0.0001	0.0001	0
	H2	2.30	2.30	0.0	0.0001	0.0001	0
	H4	2.30	2.30	0.0	0.0001	0.0001	0

Table 10. Rounded average values of microwave (9.28 GHz) permittivity of Run No. 1 specimens.

(Same notes of Table 9 apply here.)

Material	Specimen	Dielectric Constant			Loss Factor		
		1 kHz	9 GHz	Ratio	1 kHz	9 GHz	Ratio
Epoxy laminate	A1	4.93	4.64	1.06	0.0078	0.0149	0.52
	A3	4.96	4.64	1.07	0.0070	0.0148	0.47
	A2	4.96	4.64	1.07	0.0070	0.0151	0.46
	A4	4.95	4.64	1.07	0.0078	0.0148	0.53
Silicone laminate	B1	3.29	3.39	0.97	0.0047	0.0062	0.76
	B3	3.30	3.40	0.97	0.0035	0.0070	0.50
	B2	3.33	3.40	0.98	0.0046	0.0080	0.57
	B4	3.30	3.40	0.97	0.0105	0.0076	1.38
Polyurethane	C1	3.95	2.70	1.46	0.146	0.0175	0.53
	C3	4.31	2.66	1.62	0.176	0.0195	0.90
	C2	4.25	2.67	1.59	0.171	0.0198	0.86
	C4	4.43	2.66	1.66	0.188	0.0219	0.86
Epoxy-Polyamide	D1	2.97	2.81	1.06	0.0091	0.0204	0.45
	D3	3.17	2.83	1.12	0.0097	0.0290	0.34
	D2	3.21	2.84	1.12	0.0096	0.0307	0.31
	D4	3.16	2.82	1.12	0.0097	0.0236	0.41
Polyimide	E1	3.25	3.25	1.00	0.0012	0.0034	0.35
	E3	3.24	3.25	1.00	0.0012	0.0033	0.36
	E2	3.25	3.27	0.99	0.0012	0.0040	0.30
	E4	3.30	3.29	1.00	0.0012	0.0053	0.23
Teflon (FEP)	F1	2.21	2.07	1.07	0.000X	0.0006	—
	F3	2.21	2.07	1.07	0.000X	0.0006	—
	F2	2.22	2.07	1.07	0.000X	0.0006	—
	F4	2.22	2.07	1.07	0.000X	0.0006	—
Teflon (TFE)	G1	2.20	2.07	1.06	0.000X	0.0002	—
	G3	2.20	2.08	1.06	0.000X	0.0002	—
	G2	2.21	2.05	1.08	0.000X	0.0002	—
	G4	2.21	2.07	1.07	0.000X	0.0002	—
Polyethylene	H1	2.27	2.31	0.98	0.000X	0.0001	—
	H3	2.27	2.30	0.99	0.000X	0.0001	—
	H2	2.27	2.30	0.99	0.000X	0.0001	—
	H4	2.29	2.30	0.99	0.0016	0.0001	16

Table 11. Final values of permittivity at a frequency of 1 kHz and 9.28 GHz, respectively.

APPENDIX A

PRECEDING PAGE BLANK NOT FILMED.

APPENDIX A

REVIEW OF THE THEORY OF THE
 TE_{01n} RESONANT CAVITY DIELECTROMETERby
C. A. Escoffery

ABSTRACT

The background theory is reviewed for electromagnetic waves in a resonant right-circular cylinder, with particular reference to the TE_{01n} mode. A variable length TE_{01n} resonator tuned by a non-contacting plunger serves as a dielectrometer. The dielectric constant and loss tangent of a low-loss material specimen are obtained from the shift in resonant length and from the half-power bandwidth when the specimen is placed on the plunger and the cavity retuned.

1. INTRODUCTION

The Hughes X-band vacuum dielectrometer was designed⁽¹⁾ to monitor the dielectric properties of a material specimen while exposed to a simulated space environment. Figure A-1 is an artist's drawing and Figure A-2 a photograph of the dielectrometer.

The dielectric measurements are made in a suitably excited right-circular cylindrical cavity of variable length operating at a fixed frequency of 9.28 GHz. Excitation is such as to establish a TE_{01n} mode, and resonance is established by adjusting the position of a non-contacting plunger. The cavity, made out of invar, has an internal diameter of 2.1609 inches, permitting measurements above the critical frequency f_c ($f_c = 1.220 \times 3 \times 10^{10} / 2.161 \times 2.54$) of 6.66 GHz. The internal surface of the cavity is silver plated. Cavity wavelength in vacuo, λ_{gv} , at an operating frequency of 9.28 GHz is 1.8266 inches.* Total cavity length is sufficient to permit resonance at the TE_{016} mode, but measurements are preferably made between the TE_{014} and TE_{015} modes, for which range it was found that spurious modes were 32 db below the TE_{015} mode.

*Cavity wavelength, λ_g , in air is a function of the air's relative permittivity (Eq. 47), which in turn, depends on temperature and moisture content. An average value of λ_g is 1.8254 inches.

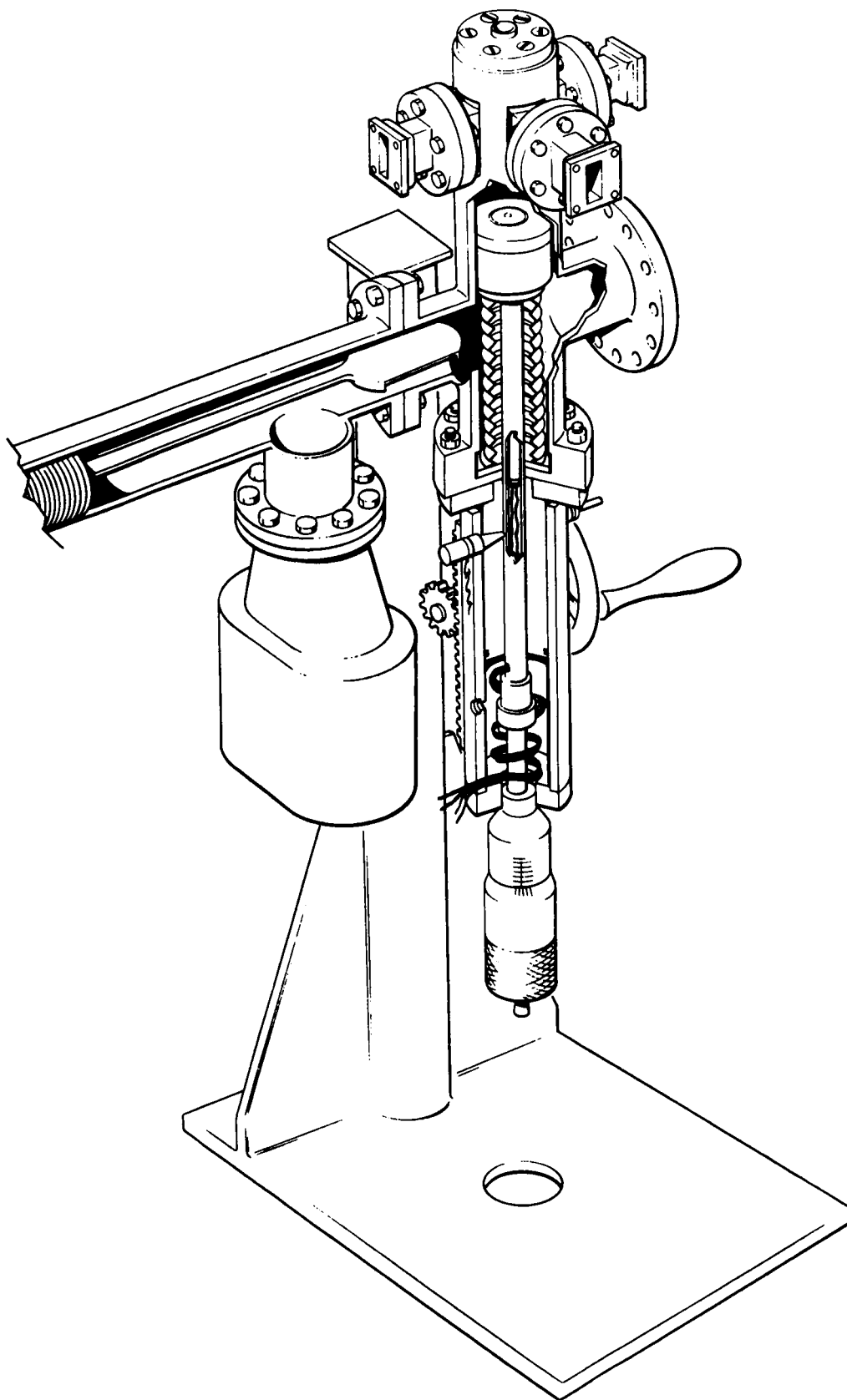


Figure A-1. Cutaway drawing of vacuum dielectrometer.
(The proposed specimen manipulator above
the ion-pump was not built.)

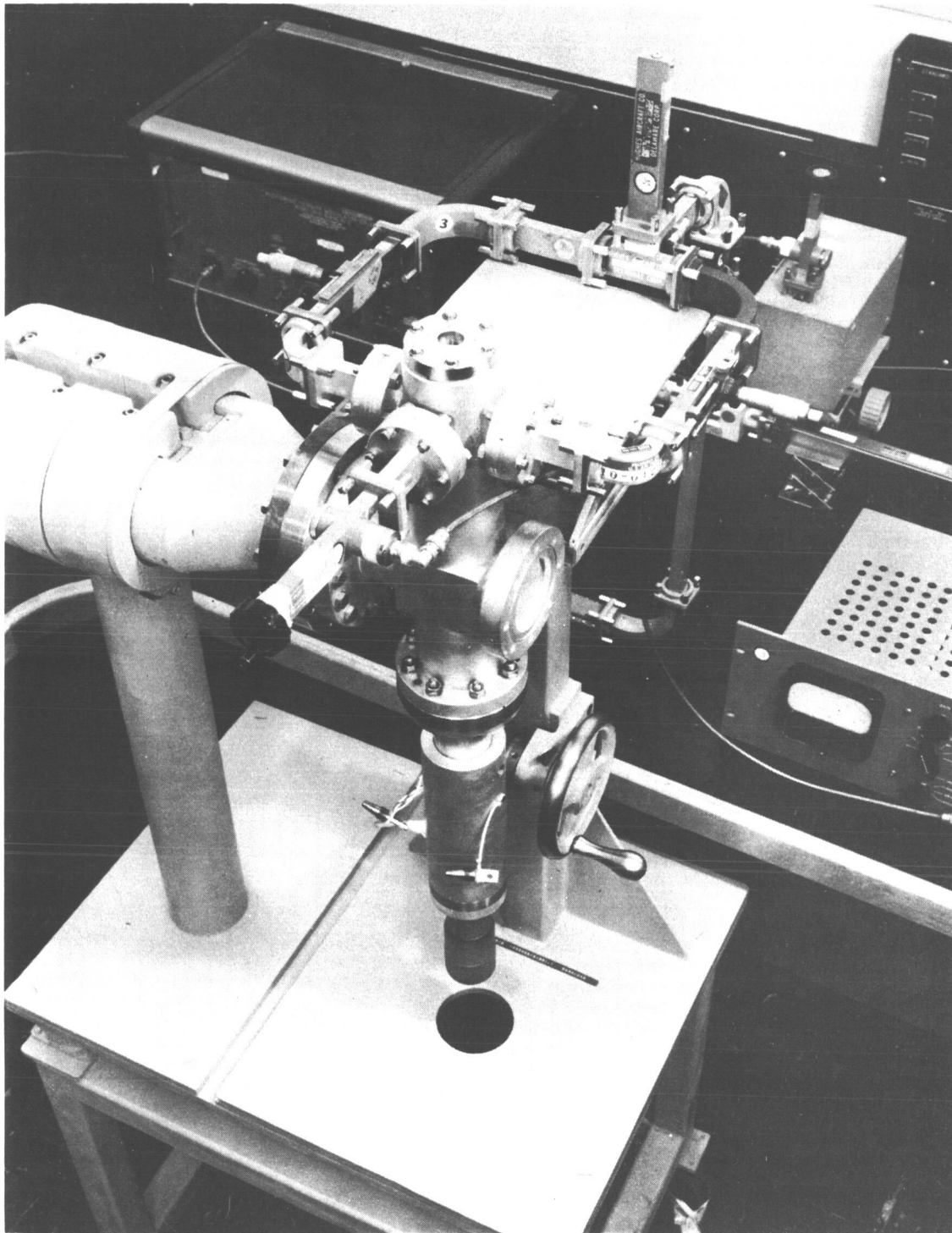


Figure A-2. Photograph of dielectrometer (insertion port open).

The practical advantages offered by the TE_{01n} mode are well known and are frequently utilized in the design of cavity wavemeters and dielectrometers. Perhaps the most useful property of the TE_{01n} mode is its symmetry (Figure A-3). The transverse part of the magnetic field (dashed lines in Figure A-3) has a radial component only, so that there are no radial electric currents on the cavity end plates. The absence of these currents permits tuning of the cavity with a non-contacting plunger on which loosely fitting disc-shaped dielectric specimens are placed for property measurements.

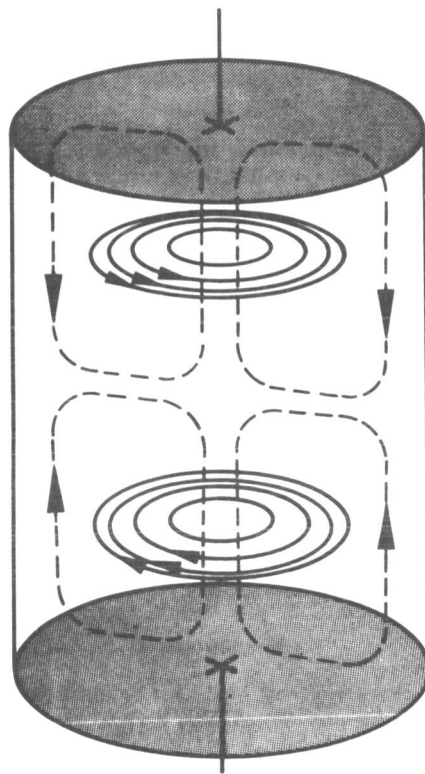


Figure A-3. Field configuration in the TE_{012} mode.

A brief review is given herein of the theory and formulas^(2,3) for the calculation of specimen relative dielectric constant and loss tangent. In essence, the resonant length of the empty cavity is measured first. The specimen is then inserted and the shift in resonant length and the

cavity Q is measured. (The Q is determined from the half-power points at resonance, i. e., the usual 3-db bandwidth.) From this information, the dielectric properties of the specimen may be calculated.

2. DEFINITIONS

The complex permittivity of a material is defined by

$$\epsilon^* = \epsilon' - j \epsilon'' \quad (1)$$

where ϵ^* is the complex permittivity, and ϵ' and ϵ'' designate the dielectric constant and loss factor, respectively. If ϵ_0 denotes the permittivity of vacuum, the complex relative permittivity, $\bar{\epsilon}^*$, is given by

$$\bar{\epsilon}^* \equiv \frac{\epsilon^*}{\epsilon_0} = \bar{\epsilon}' - j \bar{\epsilon}'' \quad (2)$$

where the bar symbol is used to designate values relative to vacuum.

The loss tangent is defined by

$$\tan \delta \equiv \frac{\epsilon''}{\epsilon'} = \frac{\bar{\epsilon}''}{\bar{\epsilon}'} \quad (3)$$

Analogous expressions hold for magnetic permeability. Thus, the complex permeability is given by

$$\mu^* = \mu' - j \mu'' \quad (4)$$

and the complex relative permeability by

$$\bar{\mu}^* \equiv \frac{\mu^*}{\mu_0} = \bar{\mu}' - j \bar{\mu}'' \quad (5)$$

In rationalized MKS units, the vacuum permittivity and permeability are equal, respectively, to

$$\epsilon_0 = \frac{1}{4\pi c^2} = 8.854 \times 10^{-12} \text{ farad/m} \quad (6)$$

$$\mu_0 = 4\pi \times 10^{-7} = 1.257 \times 10^{-6} \text{ henry/m} \quad (7)$$

where c , the velocity of light, is:

$$c = (\epsilon_0 \mu_0)^{-1/2} \cong 3 \times 10^8 \text{ m/sec} \quad (8)$$

The relative permittivity and relative permeability of air are pure numbers, essentially unity.

3. FIELD EQUATIONS

Consider the geometry illustrated in Figure A-4, which represents a perfectly homogeneous dielectric medium enclosed within a right-circular cylindrical cavity whose walls are perfect conductors. It is desired to determine the resonant frequencies and modes of the cavity. This can be done by considering them as the resultant of standing waves caused by the superposition of traveling waves that exist in transmission lines. Alternatively, the field equations may be solved directly for the natural frequencies of the cavity. We shall follow the latter approach, with particular reference to the TE_{01n} mode.

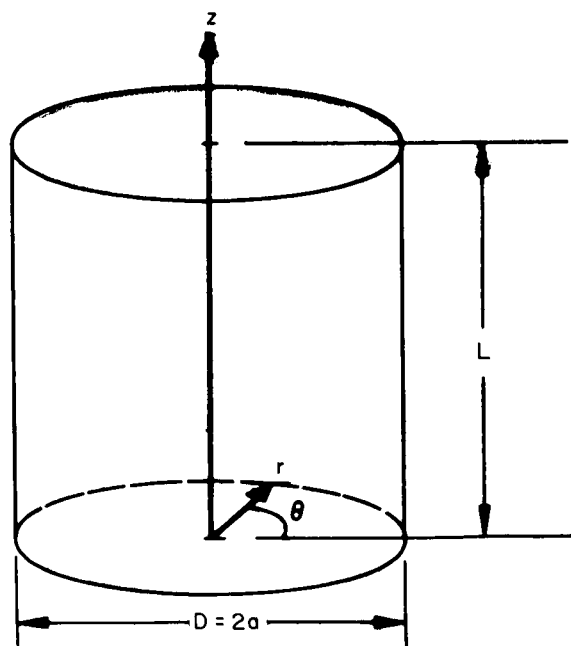


Figure A-4. Cavity geometry.

Maxwell's field equations may be written as

$$\nabla \times H = \epsilon^* \frac{\partial E}{\partial t} \quad (9)$$

$$\nabla \times E = -\mu^* \frac{\partial H}{\partial t} \quad (10)$$

and since the field contains no free electric charges or magnetic poles

$$\nabla \cdot E = 0 \quad (11)$$

$$\nabla \cdot H = 0 \quad (12)$$

To separate the electric and magnetic field vectors E and H it is convenient to differentiate with respect to time. We then obtain the well-known differential wave equations for the electromagnetic field:

$$\nabla^2 E = \frac{1}{v^2} \frac{\partial^2 E}{\partial t^2} \quad (13)$$

$$\nabla^2 H = \frac{1}{v^2} \frac{\partial^2 H}{\partial t^2} \quad (14)$$

where the phase velocity, v , is given by

$$v = (\epsilon^* \mu^*)^{-1/2} = \omega/k \quad (15)$$

and ω and k are the (angular) frequency and wave number, respectively.

Since by Fourier expansion any vibration can be represented by a summation of simple harmonic vibrations, it is customary to adopt a sinusoidal time-dependence of the form $e^{-j\omega t}$ so that

$$E = E(q) e^{-j\omega t} \quad (16)$$

$$H = H(q) e^{-j\omega t} \quad (17)$$

The solutions to Maxwell's equations can be facilitated by various mathematical techniques. ^(4 - 11) In the case of the cylindrical cavity, we set up Maxwell's differential equations in cylindrical coordinates, and the solutions ^(12 - 15) lead to an infinite number of normal-mode fields. These modes are divided into TE and TM-classes, ⁽¹⁴⁾ specified in terms of three integers, ℓ , m , and n , that refer, respectively, to field variations of E_r (or H_r) with respect to θ ; of E_θ (or H_θ) with respect to r ; and of E_r (or H_r) with respect to z .

The resonant frequencies (which include the roots, $\chi_{\ell, m}$, of Bessel functions) can be written as

$$f_{\ell, m, n}^2 = f_c^2 + \left(\frac{vn}{2L}\right)^2 \quad (18)$$

where v is given by Eq. 15), L is the cavity resonant length, and f_c is the cut-off frequency. For a perfect dielectric medium (vacuum), the cut-off frequency is given by

$$f_{c, \text{vac}} = \frac{c\chi_{\ell m}}{\pi D} \quad (19)$$

where D is the cavity diameter ($= 2a$), $\chi_{\ell m}$ is described further on (p. A-11), and c is the velocity of light, Eq. (8).

For any other medium, the cut-off frequency is

$$f_c = \frac{\chi_{\ell m} v}{\pi D} = \frac{\chi_{\ell m} (\epsilon^* \mu^*)^{-1/2}}{\pi D} \quad (20)$$

Equation (18) is often expressed in the form

$$(f D)^2 = \left(\frac{v \chi_{\ell m}}{\pi}\right)^2 + \left(\frac{vn}{2}\right)^2 \left(\frac{D}{L}\right)^2 \quad (21)$$

from which it is seen that $(f D)^2$ versus $(D/L)^2$ is a straight line with intercept $(v \chi_{\ell m}/\pi)^2$ and slope $(vn/2)^2$. This type of plot is called a mode chart. Such a chart is shown in Figure A-5 for the operating region of the Hughes dielectrometer. For an air-filled cavity, the term v in Eq. (21) may, to a first approximation, be replaced by c .

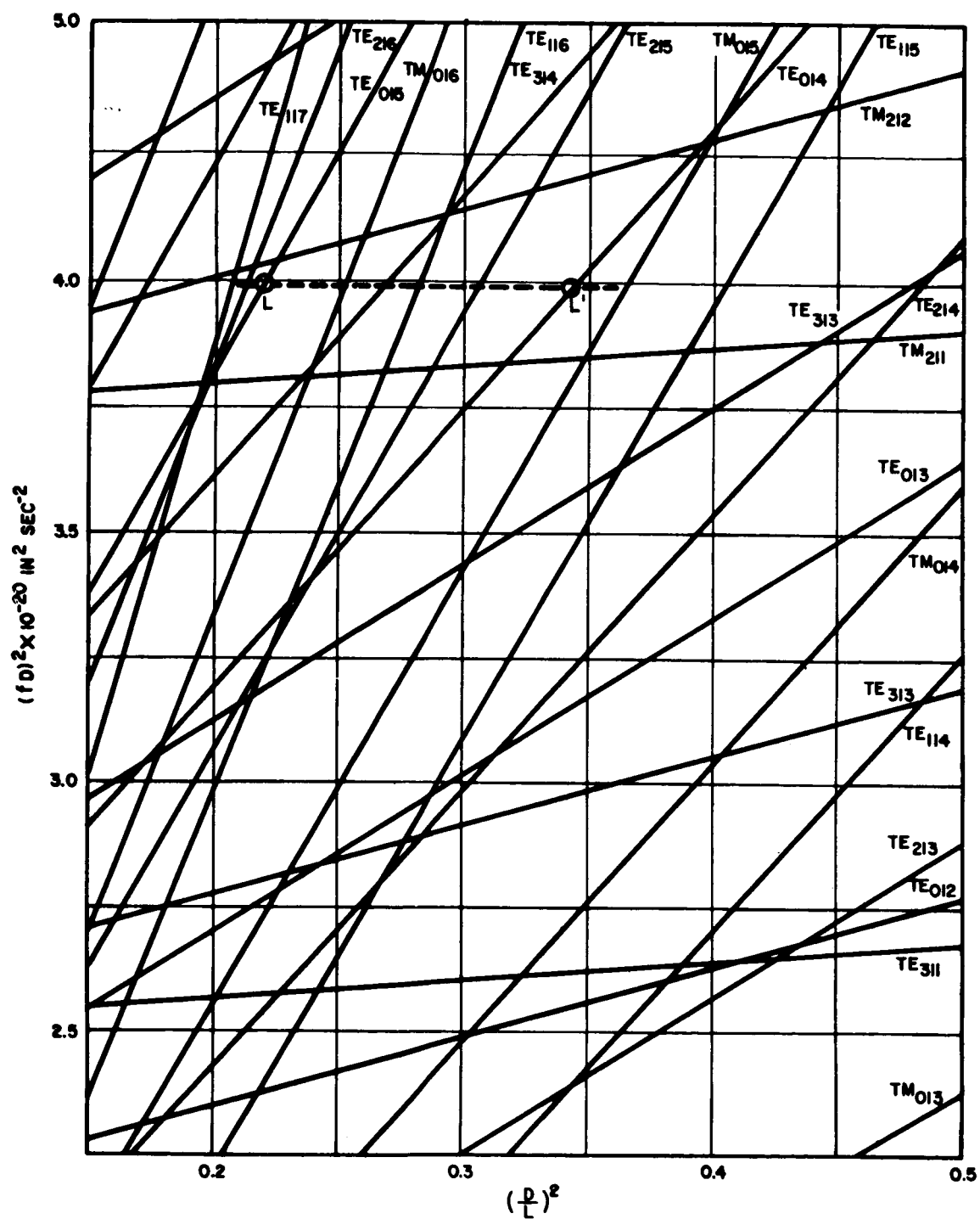


Figure A-5. Section of mode chart.

4. NORMAL-MODE FIELDS

The normal-mode fields for the right-circular cylindrical cavity are given by the following equations, ⁽¹⁵⁾ where the time dependence, though not shown for convenience, is implicit.

For the TE-modes ($m > 0, n > 0$):

$$E_r = -l \frac{J_l(k_1 r)}{k_1 r} \sin l \theta \sin k_3 z \quad (22)$$

$$E_\theta = -J'_l(k_1 r) \cos l \theta \sin k_3 z \quad (23)$$

$$E_z = 0 \quad (24)$$

$$H_r = \frac{k_3}{k} J'_l(k_1 r) \cos l \theta \cos k_3 z \quad (25)$$

$$H_\theta = -l \frac{k_3}{k} \frac{J_l(k_1 r)}{k_1 r} \sin l \theta \cos k_3 z \quad (26)$$

$$H_z = \frac{k_1}{k} J_l(k_1 r) \cos l \theta \sin k_3 z \quad (27)$$

For the TM-modes ($m > 0$):

$$E_r = -\frac{k_3}{k_1} J'_l(k_1 r) \cos l \theta \sin k_3 z \quad (28)$$

$$E_\theta = l \frac{k_3}{k} \frac{J_l(k_1 r)}{k_1 r} \sin l \theta \sin k_3 z \quad (29)$$

$$E_z = \frac{k_1}{k} J_l(k_1 r) \cos l \theta \cos k_3 z \quad (30)$$

$$H_r = -\ell \frac{J_\ell(k_1 r)}{k_1 r} \sin \ell \theta \cos k_3 z \quad (31)$$

$$H_\theta = -J'_\ell(k_1 r) \cos \ell \theta \cos k_3 z \quad (32)$$

$$H_z = 0 \quad (33)$$

where ℓ , m , and n are the previously described integers, and the k 's are wave numbers given by

$$k^2 = k_1^2 + k_3^2 \quad (34)$$

Here, k , the wave number in the dielectric when unbounded in extent, is given by

$$k = \frac{\omega}{v} = \frac{2\pi}{\lambda} \quad (15a)$$

the transverse wave number, k_1 , by

$$k_1 = \frac{\chi_{\ell m}}{a} \quad (35)$$

and the longitudinal wave number, k_3 , by

$$k_3 = \frac{n\pi}{L} \quad (36)$$

The $\chi_{\ell m}$ are the m^{th} roots of the Bessel function $J_\ell(\chi)$ for the TM-mode, and of its derivative $J'_\ell(\chi)$ for the TE-mode, respectively.

Eq. (34) can also be expressed in the form

$$k^2 = k_c^2 + k_g^2 \quad (34a)$$

using the critical wave number and guide wave number, respectively.

In the general case of wave propagation along a circular waveguide, the wave number k is given by

$$k^2 = \frac{\omega^2}{v^2} = k_1^2 - \gamma^2 \quad (37)$$

where k_1 is the transverse wave number, and γ is the propagation constant in the direction of travel, z , assuming an $e^{-\gamma z}$ spatial dependence, e.g., $E = E_0 e^{j\omega t - \gamma z}$. Also, γ is complex and given by

$$\gamma = \alpha + j\beta \quad (38)$$

where α and β denote the attenuation and phase constant along the wave. When there is little or no attenuation we can set

$$\gamma = j\beta \quad (39)$$

and therefore, from Eqs. (34) and (37), for a lossless dielectric

$$k_3 = \sqrt{-\gamma^2} = \beta \quad (40)$$

Now, from Eqs. (37) and (15) we have

$$\omega^2 (\epsilon^* \mu^*) = k_1^2 - \gamma^2 \quad (41)$$

which, for a lossless wave along the cavity becomes

$$\omega^2 (\epsilon_g' \mu_g') = k_1^2 + \beta_g^2 \quad (42)$$

where the subscript g refers to the dielectric in the waveguide (cavity).

For a vacuum dielectric ($\epsilon = \epsilon_0$); Eq. (42) becomes:

$$\beta_o^2 = k_1^2 + \beta_{g, \text{vac}}^2 \quad (43)$$

where β_0 is the phase constant in free-space, and β_{gv} designates the phase constant of an evacuated waveguide (cavity).

5. THE TE_{01n} RESONATOR

In the case of the TE_{01n} mode, $E_r = E_z = H_\theta = 0$, and we are left with Eqs. (23), (25) and (27). The resonant frequencies are given by Eqs. (18) and (19), and the cut-off frequency for the empty (vacuum) cavity is

$$f_{c,v} = 3.83171 \frac{c}{\pi D} \cong 0.610 \frac{c}{a} \quad (44)$$

since the first root of $-J_0(x_1) = J_1(x_1) = 0$ is 3.83171.

When air or some other medium fills the cavity, the cut-off frequency is given by

$$f_c = 3.83171 \frac{v}{\pi D} \cong \frac{0.610}{a} (\epsilon^* \mu^*)^{-1/2} \quad (45)$$

where ϵ^* and μ^* are the permittivity and permeability of the medium.

It should be noted that the TM_{11n} mode also has the same resonant frequency as the TE_{01n} mode. Hence, the TE_{01n} and TM_{11n} modes are degenerate. Excitation of the TM_{11n} mode in the cavity dielectrometer is largely suppressed by suitable geometrical location of the coupling orifices.

The wavelength in a dielectric-filled cavity (waveguide) is modified by the relative permittivity and permeability of the dielectric. At a given frequency, $\frac{\lambda_0}{c} = \frac{\lambda}{v}$ and, therefore, $\lambda_0 = \lambda (\epsilon^* \mu^*)^{1/2}$, where λ_0 is the wavelength in free space. Then, by rearranging Eq. (21) one obtains for the cavity wavelength

$$\lambda_g = 2\pi \left[(\epsilon^* \mu^*) \left(\frac{2\pi}{\lambda_0} \right)^2 - \left(\frac{x_{lm}}{a} \right)^2 \right]^{-1/2} \quad (46)$$

or, alternatively expressed:

$$\frac{1}{\lambda_g^2} = \left[\frac{\epsilon^* \mu^*}{\lambda_o^2} - \frac{1}{\lambda_o^2} \right] \quad (47)$$

where $\lambda_c \left(= \frac{v}{f_c} \right)$ is the cutoff wavelength, which is independent of the dielectric. For the TE_{01n} resonator, $\lambda_c = 1.64 a$.

Along the length of the cavity, resonance occurs when

$$\sin k_3 z = 0 \quad (48)$$

or when the resonant length L is

$$L = \frac{n\pi}{k_3} = \frac{n\pi}{\beta_g} \quad (49)$$

where n is any positive integer.

Obviously, from Eq. (42), β_g vanishes when $\omega^2 \epsilon' \mu' = k_1^2$, that is, for a cut-off angular frequency

$$\omega_c = k_1 (\epsilon^* \mu^*)^{-1/2} \quad (50)$$

which leads to Eq. (20)

$$f_c = \left(\frac{\omega_c}{2\pi} \right) = \frac{\chi_{lm}}{\pi D} (\epsilon^* \mu^*)^{-1/2} \quad [20]$$

6. THE TE_{01n} RESONATOR WITH LOW-LOSS TEST SPECIMEN

The following discussion is based on the procedures developed by Professor W. Jackson and students ⁽²⁾ and by Hughes Aircraft Company. ⁽³⁾

A. The Relative Permittivity of the Specimen

Consider a low-loss dielectric disc^{*}, of thickness b , at one end of the cavity, as shown in Figure A-6. Using subscripts g and s for guide (cavity) and specimen, respectively, the field equations at resonance become:

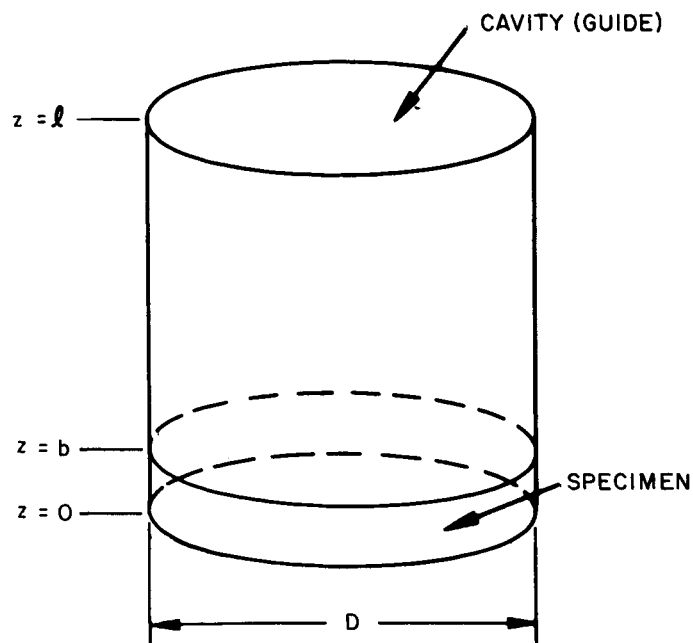


Figure A-6. Geometry of cavity with specimen inserted.

* The low-loss restriction is overcome in the analysis given by Paris⁽¹⁶⁾.

For the unfilled section ($b \leq z \leq l$):

$$E_{\theta} = J_0' (k_1 r) \sin \beta_g (z - l) \quad (51)$$

$$H_r = \frac{-j \beta_g}{\omega \mu^*} J_0' (k_1 r) \cos \beta_g (z - l) \quad (52)$$

$$H_z = \frac{j k_1}{\omega \mu^*} J_0 (k_1 r) \sin \beta_g (z - l) \quad (53)$$

and for the dielectric specimen portion ($0 \leq z \leq b$):

$$E_{\theta} = B J_0' (k_1 r) \sin (k_3)_s z \quad (54)$$

$$H_r = \frac{-j (k_3)_s}{\omega \mu^*} B J_0' (k_1 r) \cos (k_3)_s z \quad (55)$$

$$H_z = \frac{j k_1}{\omega \mu^*} B J_0 (k_1 r) \sin (k_3)_s z \quad (56)$$

where, as before, $k_1 = 3.83171/a$, $\beta_g^2 = \omega^2 \epsilon_g' \mu_g' - k_1^2$, and the specimen wave number $(k_3)_g$, is determined by

$$(k_3)_s^2 = \omega^2 (\epsilon_s^* \mu_s^*) - k_1^2 \quad (57)$$

where ϵ_s^* and μ_s^* are, respectively, the specimen permittivity and permeability.

Assuming no attenuation* in the dielectric specimen (valid for $\tan \delta < 0.1$) one can set

$$(k_3)_s \cong \beta_s \quad (58)$$

*See also Ref. (16).

and then we obtain

$$\beta_s^2 = \omega^2 (\epsilon'_s \mu'_s) - k_1^2 \quad (59)$$

where the asterisks have been replaced by the real components

Finally, by matching E_θ and H_r (and their derivatives) at the boundary $z = b$, we obtain

$$B \sin \beta_s b = - \sin \beta_g (\ell - b) \quad (60)$$

$$B \beta_s \cos \beta_s b = \beta_g \cos \beta_g (\ell - b) \quad (61)$$

Hence,
$$B = - \frac{\sin \beta_g (\ell - b)}{\sin \beta_s b} \quad (62)$$

and the resonance condition is characterized by

$$\frac{\tan \beta_s b}{\beta_s} = - \frac{\tan \beta_g (\ell - b)}{\beta_g} \quad (63)$$

The total length of the cavity with the specimens inserted is not directly measurable. What one measures is the shift $x = \ell_m - L_m = \ell - L$, where ℓ_m is the micrometer reading at the TE_{015} mode with specimen in cavity, and L_m is the micrometer reading at the TE_{014} mode of the empty cavity. Then, since $\beta_g L = 4$, $\tan \beta_g (\ell - b) = \tan \beta_g (x + L - b) = \tan \beta_g (x - b)$, and the right side of Eq. (63) is known. With the aid of tables, or by computer search, one then finds $\beta_s b$, and hence β_s . The solution is not single-valued, but the proper choice is resolved if the approximate value of the dielectric constant is known, or by repeating the measurement with a slightly different specimen thickness. It is desirable to make the specimen

thickness, b , an integral value, n , of $\frac{\lambda_s}{4} = \frac{2\pi}{\beta_s}$ where λ_s is the wavelength in the specimen. When n is even, the quantity n is unaffected by small changes in b since the air-dielectric interface is in a region of weak electric field⁽¹⁷⁾.

It is now necessary to calculate the relative dielectric constant $\bar{\epsilon}'_s$ from β_s . The following approximation is made (non-magnetic specimen):

$$\mu'_s \cong \mu'_g \quad (64)$$

Then, from Eq. (59)

$$\beta_s^2 + k_1^2 = \omega^2 (\epsilon'_s \mu'_g) \quad (65)$$

$$= (\omega^2 \epsilon'_g \mu'_g) \left(\frac{\epsilon'_s}{\epsilon'_g} \right) \quad (66)$$

$$= (\beta_g^2 + k_1^2) \left(\frac{\epsilon'_s}{\epsilon'_g} \right) \quad (67)$$

Hence, approximately,

$$\frac{\epsilon'_s}{\epsilon'_g} \cong \frac{\beta_s^2 + k_1^2}{\beta_g^2 + k_1^2} \quad (68)$$

If the cavity is evacuated, $\epsilon'_g = \epsilon_0$ and β_g becomes $\beta_{g,vac}$. Then, through Eq. (43), Eq. (68) yields the relative dielectric constant of a (non-magnetic) specimen with respect to vacuum in the form

$$\bar{\epsilon}'_s \cong \frac{\beta_s^2 + k_1^2}{\beta_0^2} \quad (69)$$

A better approximation than Eqs. (68) and (69) is obtained by consideration of Eq. (37), which, for a specimen, may be written as

$$\gamma_s^2 = k_1^2 - \epsilon_s^* \mu_s^* \omega^2 \quad (70)$$

and for a nonmagnetic sample ($\mu_s^* \approx \mu_0$) as

$$\gamma_s^2 = k_1^2 - \bar{\epsilon}_s' (1 - j \tan \delta) \beta_0^2 \quad (71)$$

where ($\gamma_s = \alpha_s + j \beta_s$) is the complex propagation constant in the dielectric specimen. When real and imaginary parts are separated, two equations may be obtained relating α_s and β_s with $\bar{\epsilon}_s'$ and $\tan \delta$. After eliminating α_s and expanding in powers of $\tan \delta$ one obtains

$$\bar{\epsilon}_s' = \frac{\beta_s^2 + k_1^2}{\beta_0^2} \left(1 - \frac{\beta_s^2 + k_1^2}{\beta_s^2} \cdot \frac{\tan^2 \delta}{4} + \dots \right) \quad (72)$$

where the remaining terms are of the order of $\tan^4 \delta$ or higher. For $\tan \delta \ll 1$, Eq. (72) reduces to Eq. (69).

Similarly, Eq. (68) is an approximation to the more exact general equation

$$\boxed{\frac{\epsilon_s'}{\epsilon_g} = \frac{\beta_s^2 + k_1^2}{\beta_g^2 + k_1^2} \left(1 - \frac{\beta_s^2 + k_1^2}{\beta_s^2} \frac{\tan^2 \delta}{4} + \dots \right)} \quad (73)$$

B. The Loss Tangent of the Specimen

Let Q be the quality value for the empty resonator:

$$Q = 2\pi f \cdot \frac{\text{Energy stored in resonator dielectric}}{\text{Power dissipated in resonator}} \quad (74)$$

where the power losses include the loss in the metal walls of the cavity.

By a somewhat lengthy procedure it can be shown⁽³⁾ that

$$\tan \delta = \left(\frac{1}{Q_T} - \frac{1}{Q'} \right) \left(\frac{\bar{\epsilon}_s' B^2 b' + l}{\bar{\epsilon}_s' B^2 b'} \right) \quad (75)$$

where Q_T is the Q of a cavity containing a specimen (whose losses are considered); Q' is an idealized Q of the cavity containing a lossless specimen of the same relative permittivity as the actual specimen; l is the cavity resonant length; b' is a modified specimen thickness, related to the actual thickness b by:

$$b' = b \left(1 - \frac{\sin 2\beta_s b}{2\beta_s b} \right) \quad (76)$$

and B is given by Eq. (62), that is,

$$B = - \frac{\sin \beta_g (l - b)}{\sin \beta_s} \quad (77)$$

Through an involved calculation it can also be shown that the quantity Q_T is related to the half-width Δl of the resonance peak (frequency ω_0 held constant and the length l of the cavity variable), and that the loss tangent is given by

$$\tan \delta = \frac{\beta_g^2}{\beta_0^2} \cdot \frac{1}{\bar{\epsilon}_s' B^2 b'} (\Delta l - C) \quad (78)$$

where ϵ'_g is obtained by Eqs. (69) or (68) depending on whether the cavity is evacuated or not. C is a correction term, generally small with respect to $\Delta\ell$, and given by

$$C = \frac{d}{a} \left[a \left(1 + B^2 \frac{\beta_s^2}{\beta_g^2} \right) + \frac{k_1^2}{\beta_g^2} (B^2 b' + \ell') \right] \quad (79)$$

where ℓ' is a modified cavity length given by:

$$\ell' = (\ell - b) \left(1 - \frac{\sin 2\beta_g (\ell - b)}{2\beta_g (\ell - b)} \right) \quad (80)$$

and d is the skin depth of the cavity material. The quantity d/a must be inferred from measurements on the empty cavity, through the expression

$$\frac{d}{a} = \frac{\beta_g^2}{k_1^2 + 2\beta_g^2 (a/L)} \cdot \frac{\Delta L}{L} \quad (81)$$

where ΔL is the half-width of the resonance peak of the empty cavity, and L is the resonant length.

7. SUMMARY

With the TE_{01n} resonant cavity dielectrometer, the specimen relative dielectric constant is obtained by Eq. (73) and the loss tangent through Eq. (78).

Since the calculations are laborious, it is advisable to program them for a high speed electronic computer.

8. REFERENCES

- (1) C. A. Escoffery, "A High Vacuum Dielectrometer for Microwave Measurements in Simulated Space Environments," Hughes Aircraft Company, TIC 2748.20/471 (19 May 1964).
- (2) F. Horner et al, "Resonance Methods of Dielectric Measurement at Centimeter Wavelengths," Proc. Inst. Elec. Engrs., 93 (III), 53 (1946).
- (3) D. N. Langenberg and B. A. Lengyel, "Resonant Cavity Dielectrometers," in Hughes Aircraft Company document TM-577 (June 1958).
- (4) S. A. Schelkunoff, "Electromagnetic Waves," Van Nostrand, New York (1943).
- (5) J. A. Stratton, "Electromagnetic Theory," McGraw-Hill, New York (1941).
- (6) C. G. Montgomery, "Electromagnetic Waves," in "Principles of Microwave Circuits" (Vol. 8 of Radiation Laboratory Series), McGraw-Hill, New York (1948).
- (7) H. Marcuvitz, "Waveguide Handbook" (Vol. 10 of Radiation Laboratory Series), McGraw-Hill, New York (1951).
- (8) H. R. L. Lamont, "Wave Guides," Methuen Monograph, London (1950).
- (9) W. L. Barrow, "Transmission of Electromagnetic Waves in Hollow Tubes of Metal," Proc. IRE 24, 1298 (1936).
- (10) G. C. Southworth, "Hyper-Frequency Wave Guides - General Considerations and Experimental Results," Bell Systems Technical Journal 15, 284 (1936).
- (11) J. R. Carson, S. P. Mead and S. A. Schelkunoff, "Hyper-Frequency Wave Guides," Bell Systems Technical Journal 15, 310 (1936).
- (12) W. Hansen, "A Type of Electrical Resonator," Journal of Applied Physics 9, 654 (1938).
- (13) F. Borgnis, "Electromagnetische Eigenschwingungen dielektrische Räume," Ann. Phys. 35, 359 (1939).
- (14) W. L. Barrow and W. W. Mieher, "Natural Oscillations of Electrical Cavity Resonators," Proc. IRE 28, 184 (1940).

- (15) C.G. Montgomery, "Techniques of Microwave Measurements," p. 297 (Vol. 11 of Radiation Laboratory Series), McGraw-Hill, New York (1947).
- (16) D.T. Paris, "An Extension of the TE_{01n} Resonator Method of Making Measurements on Solid Dielectrics," Trans. IEEE on MTT, 12, 251 (1964).
- (17) R.P. Penrose, "Some Measurements of the Permittivity and Power Factor of Low Loss Solids at 25,000 Mc/sec Frequency," Trans. Farad. Soc. 42A, 190 (1946).

APPENDIX B

INTERDEPARTMENTAL CORRESPONDENCE

TO: C. A. Escoffery
ORG.

DATE: 17 August 1965
REF. 2782.3/130

SUBJECT: An Integrating Sphere for Measuring
the Reflectance of Irradiated
Materials¹

FROM: T. P. Handy
ORG. 27-82-00

BLDG. 5 MAIL STA. B-146
EXT. 4741

The preliminary investigations of the integrating sphere are now completed. The suggested arrangement of sphere and monochromator to be used is shown in Figure 1.

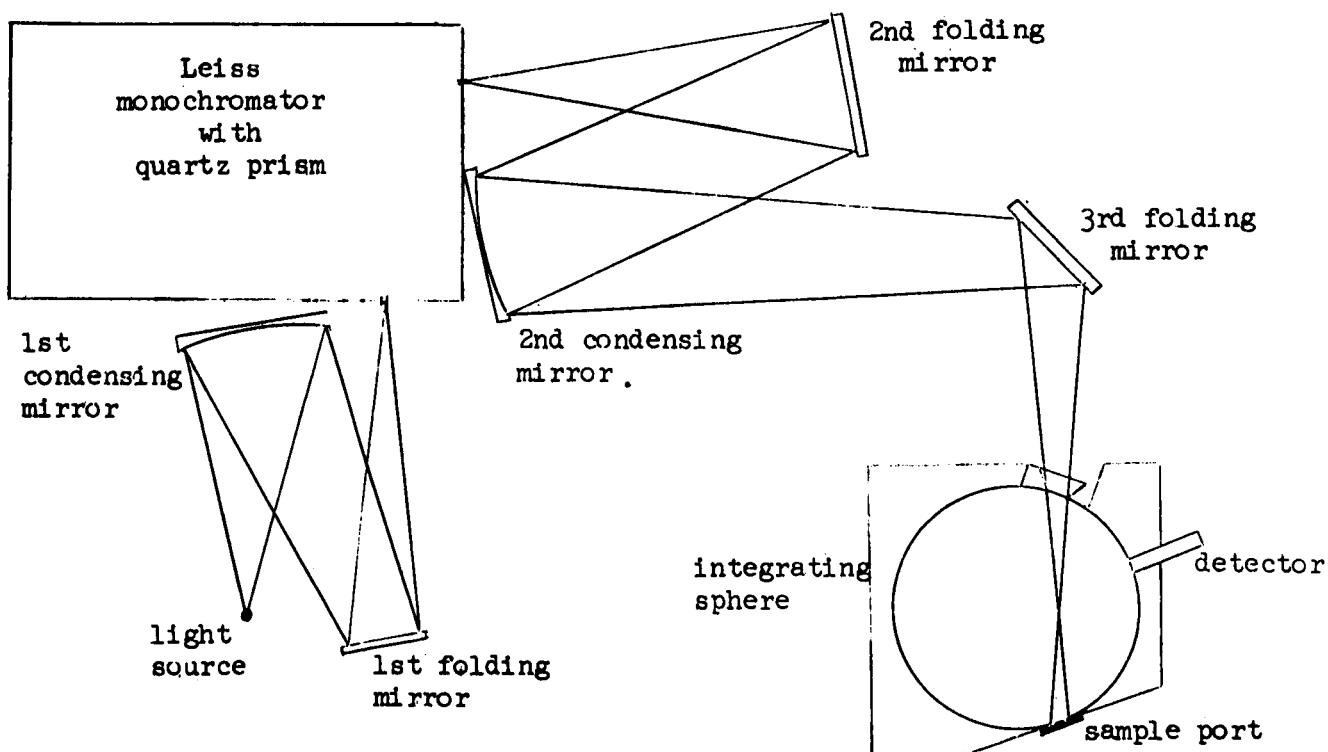


Figure I-1. Optical schematic of integrating sphere and its optics

¹Ref. HAC Technical Proposal TP-632 (65H-2961/A7419), April 1965, "Combined Effects of Space Environmental Parameters on Space Vehicle Materials"

To keep the measurement errors small, the illuminated area at the sample port must be as small as possible. If the sample port is too small, the incident light beam will be so much larger than the sample that an excessive amount of energy will be lost. Also, if the monochromator slit is focused directly on the sample, the sample will have to be long and very narrow. This presents a serious construction problem due to the length of the slit that must be formed in the curved sphere surface. However, it was found that by defocusing, as shown in Figure 1, and by masking the entrance slit of the monochromator, a square area could be illuminated. By properly adjusting the optics, this area will be well defined and sufficiently small. This arrangement will reduce the loss of effective internal area of the sphere and will minimize the image area, which significantly reduces the system error.

An analysis was made to determine the errors introduced by various values of sample area, C, and of internal sphere area, S, versus true sample reflectance, R_S . The error analysis was based on the work of Fussell, et al:²

$$\frac{B_S}{B_{ST}} = \frac{R_S}{R_{ST}} \left[1 - \frac{(R_{ST} - R_S)C}{S - RD - R_S C} \right] \quad (1)$$

where

B_S = total light flux passing into the detector port when the test sample is over the sample port

B_{ST} = total light flux passing into the detector port when the reflectance standard is over the sample port

R_S = true reflectance of test sample

R_{ST} = true reflectance of the reflectance standard

R = reflectance of the interior of the sphere

D = S - (A + B + C)

S = total internal area of the sphere

A = area of the entrance port

²W. B. Fussell, J. J. Triolo, and F. A. Jerozal, NASA Technical Note D-1714, "Portable Integrating Sphere for Monitoring Reflectance of Spacecraft Coatings"

B = area of the detector port

C = area of the sample port

By letting the expression $\left[\frac{(R_{ST} - R_S)C}{S - RD - R_S C} \right]$ equal "K", Eq. (1) reduces to

$$\frac{B_S}{R_{ST}} R_{ST} = R_S - K R_S. \quad (2)$$

The term $(-K R_S)$ represents the magnitude and direction of the error. That is, if $(-K R_S)$ equals -0.02, then the measured value corrected for the reflectance of the standard $\left(\frac{B_S}{B_{ST}} R_{ST} \right)$ will be two percent lower than the true value of R_S . Note that (B_S/B_{ST}) is the measured reflectance of the sample as compared to that of the reflectance standard. It was noted that the error function $(-K R_S)$ is not very dependent upon the value of A, the area of the entrance port. Since $(-K R_S)$ is quite dependent upon the total internal area of the sphere and the area of the sample port, its value was calculated for several values of these two variables. Figure 2 shows $(-K R_S)$ as a function of R_S , the true sample reflectance for several values of C, the sample port area, and two values of R_{ST} . Figure 3 shows $(-K R_S)$ as a function of R_S for several values of S, the internal area of the sphere, and two values of R_{ST} .

From Figures 2 and 3, it is seen that if the area of the sample port is less than 0.05 square inch, and the internal area of the sphere is approximately 20 square inches, the maximum error $(-K R_S)$ will be less than one percent.

On this basis, it is proposed that the entrance port dimension should be 0.25 x 0.50 inch (0.125 in²), the internal area of the sphere should be approximately 20 in², and the sample dimensions should be 0.20 x 0.20 inch (0.040 in²).

As an aid in aligning the entrance and sample ports, it is suggested that the portion of the sphere immediately surrounding the entrance port be made in the form of a cylindrical plug (see Figure 4). This will also make the unit more versatile, as it will be easy to change the configuration of the ports.

T. P. Handy
T. P. Handy

Approved: R. H. Frels by L. F. Rogers
R. H. Frels, Head, Optics Section

TPH:dr

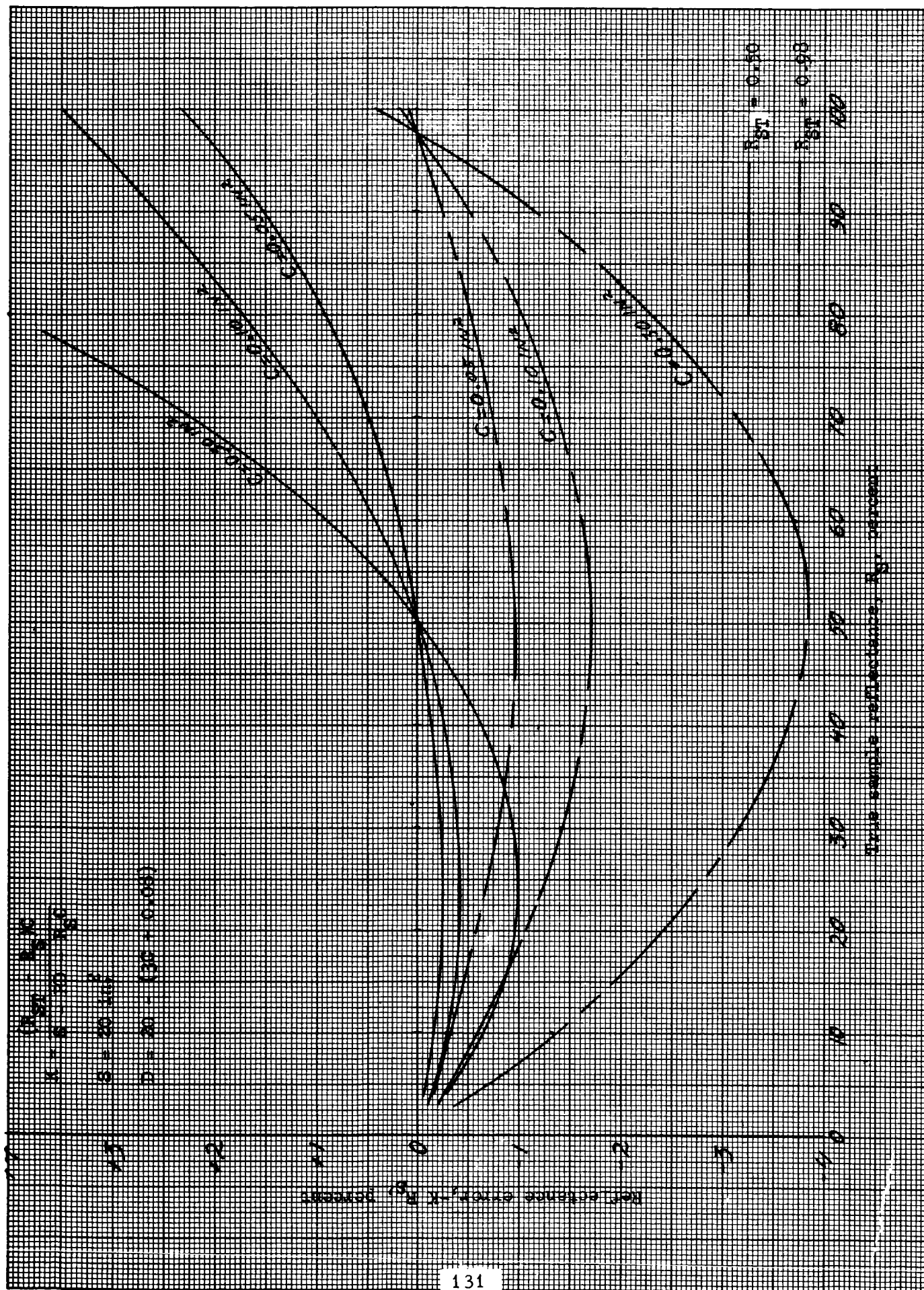


Figure I-2. Reflectance errors for various sample ports

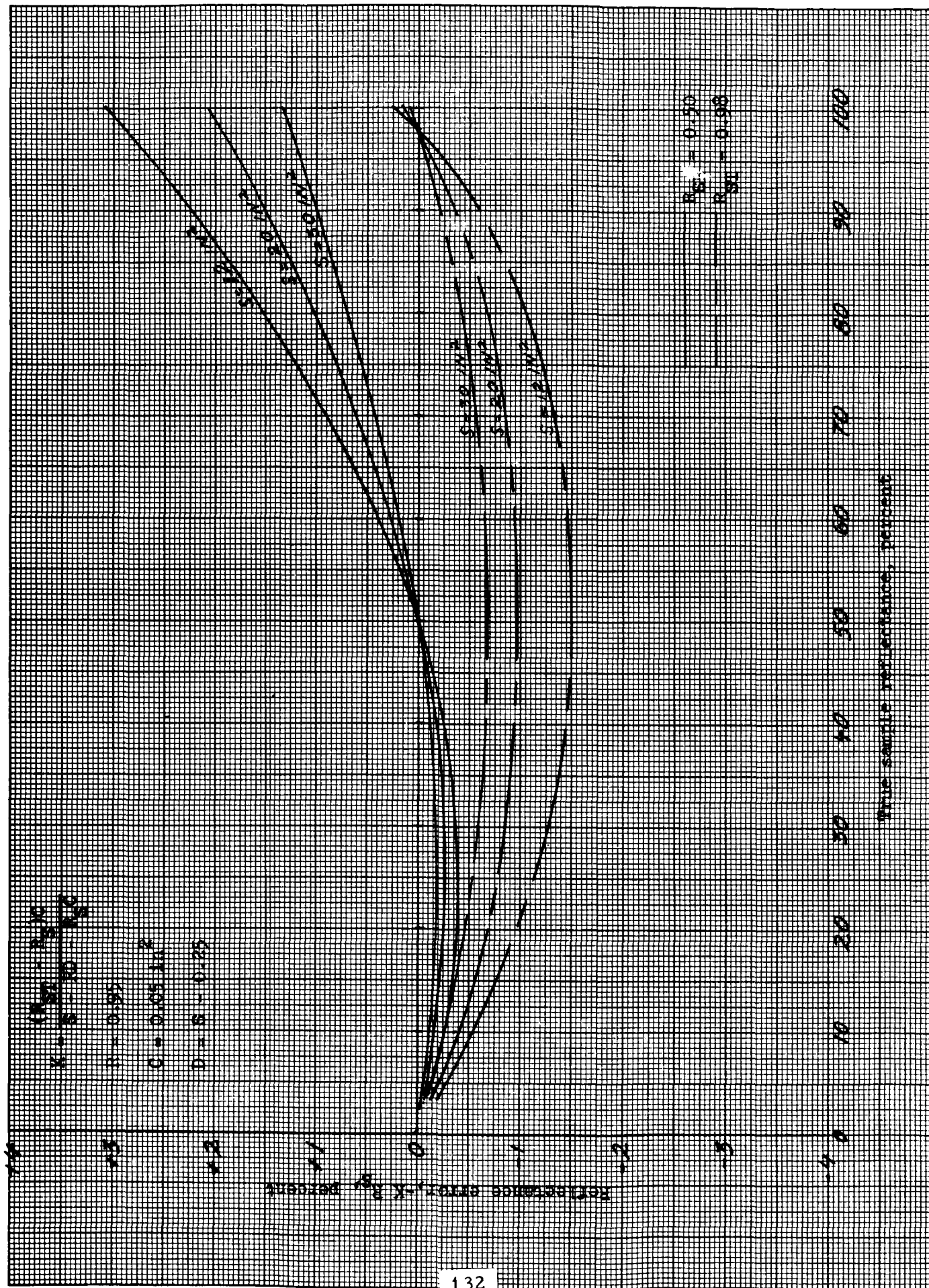


Figure I-3. Reflectance errors for various internal sphere areas

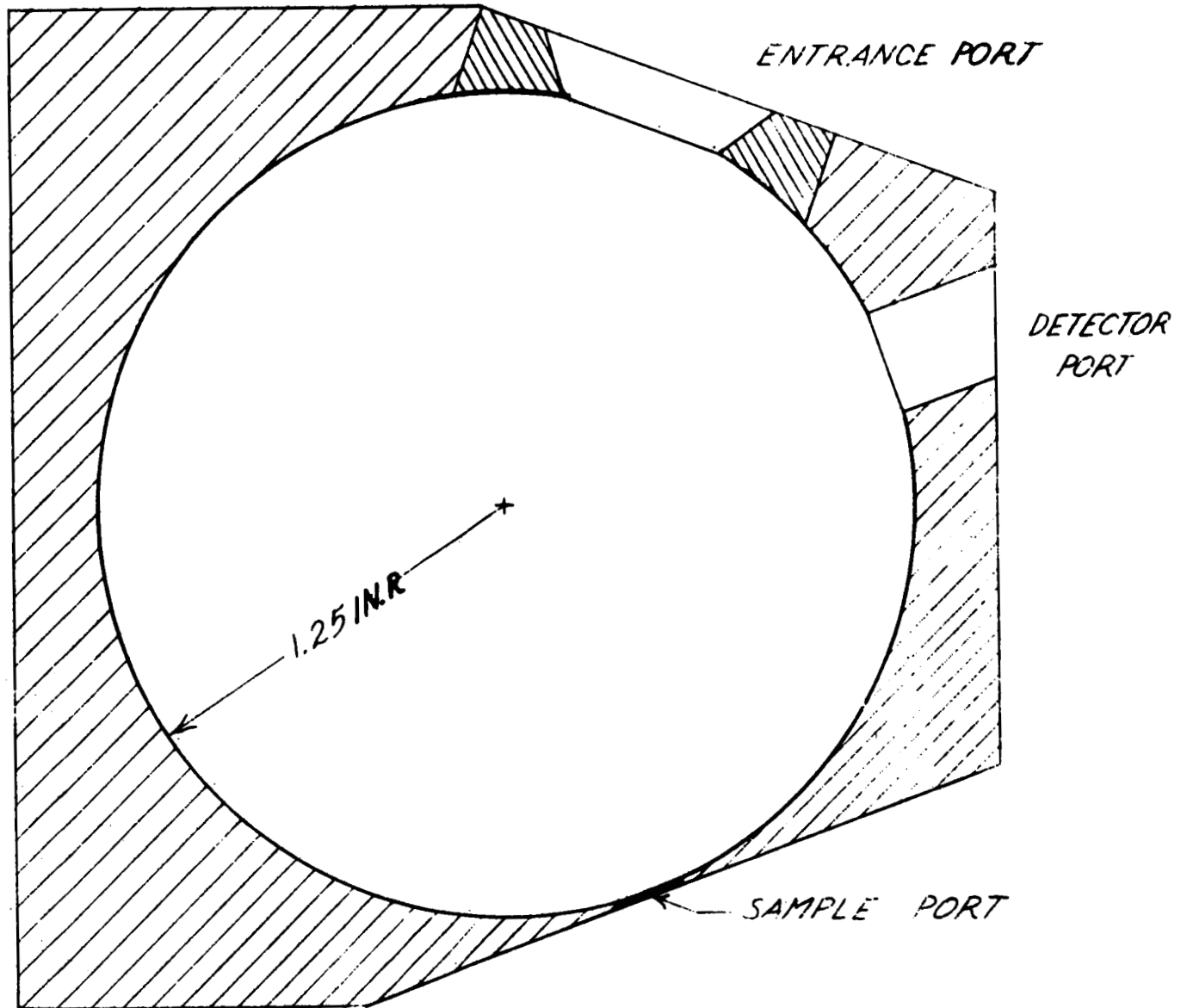


Figure I-4. Integrating sphere.

REFERENCES

1. W. J. Lewis, G. E. Faulkner, and P. J. Rieppel, "Brazing and Soldering of Titanium," Titanium Metallurgical Laboratory Report No. 45, Battelle Memorial Institute, 7 June 1956.
2. A. J. Parker, R. J. Jenkins, C. P. Butler, and G. L. Abott, "Flash Method of Determining Thermal Diffusivity, Heat Capacity, and Thermal Conductivity," Journal of Applied Physics **32**, 1679 (1961).
3. Hughes Aircraft Company, Culver City, California, Report TP-632, Technical Proposal for Combined Effects of Space Environmental Parameters on Space Vehicle Materials, April 1965.
4. "Electrical Resistance of Insulating Materials," ASTM Designation D257-61.
5. J. V. Hughes and H. L. Armstrong, "The Dielectric Constant of Dry Air," Journal of Applied Physics, **23**, 501 (1952).
6. B. G. Kimmel and C. A. Escoffery, "Development of Dielectric Windows for Spacecraft Antennas," Final Report on NAS 8-11026, Hughes Aircraft Company, April 1966.
7. C. A. Escoffery, "Vacuum Resonant-Cavity Dielectrometer for in situ Measurements of Complex Permittivity in a Simulated Space Environment," IEEE Transactions Nuclear Science, NS-13, No. ____ (1966); to be published; also issued as Hughes Aircraft Company Document Technical Memorandum TM-864, July 1966.
8. C. A. Escoffery, "Investigation of the Combined Effects of Space Environmental Parameters on Space Vehicle Materials," Quarterly Progress Report No. 3, Hughes Aircraft Company Report P66-106, April 1966.
9. F. Horner, T. A. Taylor, R. Dunsmuir, R. Lamb, and W. Jackson, "Resonance Methods of Dielectric Measurement at Centimeter Wavelengths," Journal of the Institution of Electrical Engineers, **93**, Part III, 53 (1946).
10. D. N. Langenberg and B. A. Lenyel, "Resonant Cavity Dielectrometers," Appendix B in: "Microwave Dielectric Measurements at High Temperatures," by H. R. Hope and W. W. Bayless, June 1958; Astia Document AD-207804.

11. H. Levinstein, "Infrared Detectors," Chapter 8 in Applied Optics and Optical Engineering Vol. II (R. Kingslake Ed.), Academic Press, New York, 1956.
12. P.M. Blair, Jr., Private Communication.
13. R. Stair and W.E. Schneider, "The NBS Instrumentation for Use in the Measurement of Spectral Irradiance of Solar Simulators," Proc. Int'l. Symposium on Solar Simulation, Inst. Environmental Sciences and ASTM, Los Angeles, California, p. 75, January 1965.
14. A. Hirshman, W.L. Derksen, and T.I. Monahan, "A Proposed Method for Measuring Thermal Diffusivity at Elevated Temperatures," Armed Forces Special Weapons Project Report, AFSWP 1145, Material Laboratory, New York Naval Shipyard, April 1959.
15. H.W. Deem and W.D. Wood, "Flash Thermal-Diffusivity Measurements Using a Laser," Review of Scientific Instruments 33, 1107 (1962).
16. F.G. Penneman, "A Long-Pulse Method of Determining Thermal Diffusivity," Solar Energy 9, 113 (1965).
17. R. J. Jenkins, "Experimental Aspects of the Flash Method of Determining Thermal Conductivity," 3rd Conference on Thermal Conductivity, U.S. Naval Radiological Defense Lab., San Francisco, California, 1963.
18. G.R. Cunningham, F. J. Smith, and W. Bradshaw, "Thermal Diffusivity of Graphites and Chars Using a Pulsed Laser," AIAA Thermophysics Specialist Conference, Monterey, California, September 1965.
19. R. Taylor, "An Investigation of the Heat Pulse Method for Measuring Thermal Diffusivity," Brit. J. Appl. Phys. 16, 509 (1965).
20. R.S. Mallouk (E. I. duPont de Nemours & Co.), "Polyimide Films," Machine Design 37, 232 (1964).
21. E.I. duPont de Nemours & Co. , Publication A-120703.
22. E.I. duPont de Nemours & Co. , Technical Bulletin T-4B.
23. E.S. Hotson, "Correction Term For Dielectric Measurements With Cavity Resonators," J. Sci. Instr. 38, 139 (1961).

24. Ye. B. Zal'tsman and V. Ye. Poyarkova, "On One Systematic Error of Measurement of Dielectric Constant by the Resonance Method with the Application of a H_{01n} Resonator," July 1961; Document N65-11113, part of English translation by the AF Systems Command, FTD-MT-64-06.
25. J. Lamb, "Dielectric Measurements at Wavelengths Around 1cm by Means of an H_{01} Cylindrical-Cavity Resonator," J. IEEE (London) 93 (Pt. III A), 92 (1946).
26. J.A. Knowlton, G.R. Mahn, and J.W. Ranftl, "The Resonant Transformer: A Source of High-Energy Electrons," Nucleonics 11 (11), 64 (November 1953).
27. R.J. Witt, J.J. Chapman, and B.L. Raskin, "Measuring of Surface and Volume Resistances," Modern Plastics 24, 151 (April 1947).